Electronic Structure Investigations of Group III-Nitrides Surface and Interfaces

vorgelegt von
Master of Science (M. S.)
Chia-Hao Chen,
aus Hsinchu, Taiwan

Von der Fakultät II - Mathematik und Naturwissenschaften
der Technischen Universität Berlin
zur Erlangung des akademischen Grades
Doktor der Naturwissenschaften
Dr.rer.nat.

genehmigte Dissertation

Promotionsausschuss:
Vorsitzender: Prof. Dr. Peter Zimmermann
Berichter/Gutachter: Prof. Dr. Mario Dähne
Berichter/Gutachter: Prof. Karsten Horn, Ph.D.

Tag der wissenschaftlichen Aussprache: 08. September 2003

Berlin 2003
D 83

Abstract

Group III–nitride semiconductors and their alloys have attracted a lot of attentions in the past decade because of their applications as short–wavelength emitters and optoelectronic devices. All of the developments were encouraged by the realization of the p–type doping of the nitride semiconductors and the successful growth of high quality thin films.

In spite of the rapid growth of nitride–related commercial products, there are still many fundamental aspects of these semiconductors that need to be addressed. This thesis reports investigations of the electronic properties of group III–nitride semiconductors by means of angle–resolved photoemission spectroscopy (ARPES) with synchrotron radiation and low energy electron diffraction (LEED).

In this thesis, the cleaning procedure for cubic InN has been studied and a good crystalline–ordered surface has been restored. The growth of hexagonal GaN thin films on 6H–SiC(0001) surface by molecular beam epitaxy with ammonia or nitrogen plasma as nitrogen atom sources has been carried out. Using ammonia gas better GaN thin films can be grown than with nitrogen plasma, judging from LEED and photoemission data.

The occupied valence band of cubic InN, wurtzite GaN, and wurtzite AlN were studied by ARPES and the dispersive features in the valence region were converted to bulk valence band structures with the assumption of a free electron final state. A surface state was observed from the ammonia grown GaN(0001)–(1×1) surface, and the mapping of this state along $\overline{\Gamma}-\overline{M}$ line has been carried out.

GaN/SiC heterointerfaces were studied by photoemission spectroscopy. The core level line shape analysis revealed that only nitrogen formed chemical bonds with silicon in the interface region, which is due to the surface nitridation process on the SiC(0001) surface prior to the GaN overlayer growth,

in order to increase the surface energy and improve the wetting of Ga on the SiC surface. The GaN/SiC heterojunction is of the staggered type (type II) alignment, and the measured valence band offset is 1.02 eV and 1.10 eV for ammonia growth and plasma growth GaN thin films, respectively.

Schottky barrier formation of Ag on GaN and Ag on AlN surfaces has been investigated by mean of photoemission spectroscopy. The surface photovoltage effect was observed after the semiconductors were cooled down to liquid nitrogen temperature. This effect has to be corrected in the determination of Schottky barrier height by the photoemission technique. The barrier height is 1.01 eV for Ag/GaN and 2.87 eV for Ag/AlN. The results show that the Schottky barrier heights of nonreactive metals on GaN and AlN surfaces cannot be described by the Schottky–Mott rule.

Contents

Abstract **iii**

1 Introduction **1**

2 Experimental Setup **7**
2.1 Photoelectron Spectroscopy 7
2.2 Synchrotron Radiation 9
2.3 Low Energy Electron Diffraction 11
2.4 Molecular Beam Epitaxy 13
2.5 Plasma Source 15
2.6 The vacuum system 17

3 Basics **19**
3.1 Electronic Bands 19
3.2 Photoemission Spectroscopy 22
3.2.1 Angle–Resolved Photoelectron Spectroscopy 23

4 Electronic Structure of Group III-Nitrides **33**
4.1 Cubic Indium Nitride 33
4.1.1 The Growth of c–InN 34
4.1.2 The Cleaning Process 37
4.1.3 ARPES Studies 39
4.2 Wurtzite Gallium Nitride 45
4.2.1 The Growth of w–GaN 46
4.2.2 The electronic structure of w–GaN 55
4.3 Wurtzite Aluminum Nitride 63
4.3.1 The Growth of w–AlN 64
4.3.2 The electronic structure of w–AlN 65
4.4 Conclusions 68

5 The SiC/GaN Heterointerface **69**

5.1 Heterojunctions 70

5.2 Investigation of Semiconductor Heterojunctions Using Photoemission 72

5.3 Core Levels 76

6 Metal–Nitride Interfaces **85**

6.1 Metal–Semiconductor Interfaces 86

6.2 Sample Preparation 89

6.3 Schottky Barrier Heights 89

7 Summary **99**

Bibliography **105**

Acknowledgements **119**

Zusammenfassung **121**

Chapter 1

Introduction

Traditionally, the essential part of a television set (TV) or monitor is a cathode–ray tube (CRT), which basically is a vacuum tube consisting of an electron gun at one end and a phosphor screen at the other, in between a coil to apply a magnetic field to control the trajectory of the electrons, or the so–called cathode–ray. Electrons need space to fly in a controllable manner, and the coil is heavy, this makes the CRT type TV bulky. Furthermore, the size of the vacuum vessel is limited, and an outdoor display, which needs a big screen, is therefore difficult to achieve by this type of monitor. Hence researchers are looking for substitutions to replace the CRT monitor. Liquid crystal displays (LCD) are one option, light emitting diodes (LED) another.

LCD has advantages and disadvantages. It is light and thin, but its manufacturing difficulty increases with size, and the price is relatively high. This is the reason that it only existed for the laptop computer in the beginning, and has become available for large size display in reasonable price only very recently and becoming popular for desk top computer and family TV set. But its size is also limited as the CRT monitor, and it cannot be used outdoor because of its small screen size and low brightness.

LEDs is another choice other than the LCD. However, up to the early 1990s, LEDs only operated in the red–to–yellow portion of the spectrum.[Craford, 1992] It was not until 1994, that the commercial introduction of extremely bright LEDs, based on gallium nitride compound semiconductors that can operate in the green–to–ultraviolet range, with efficiencies comparable to red and yellow LEDs. Moreover, these gallium nitride–based semiconductors have also been used in diode lasers operating at room temperature and emitting light in the blue–violet range, first under pulsed condition[Nakamura et al., 1996] in late 1995 and later under

continuous operation.[Nakamura, 1996]

With these technological advances, two particularly important areas of application have opened up. One is the ability to produce all three primary colours in LEDs, which implies applications in traffic lights, outdoor signs and also makes the realization of full colour large panel displays possible. The other is the availability of shorter–wavelength diode lasers. The first major commercial impact of these blue diode lasers will likely occur in high–density optical storage media, specifically in digital versatile disks (DVDs).[Johnson et al., Oct. 2000] Although promising optoelectronic applications of the nitride semiconductors is the most important driving force for the rapid development of these materials in the past ten years, it is not the only stage on which III–V nitride and related materials can play. For example, due to their high durability and inertness to chemical etching, nitride semiconductors are conducive to high power devices and circuits, especially with applications in high temperature and unfriendly environments[Strite and Morkoç, 1992] Some electronic devices like high temperature transistors and high power high frequency transistors have been demonstrated already.[Monemar and Pozina, 2000]

There are two main advantages of nitride semiconductors for a blue light source. Foremost is the large band gap associated with the Al–Ga–In–N system, which encompasses the entire visible spectrum. The $\mathrm{Ga_xIn_{1-x}N}$ ternary alloys have band gaps ranging from 1.9 eV (red) for InN to 3.4 eV (ultraviolet) for GaN.[Ambacher, 1998] The other main advantage of the nitrides over other wide band gap semiconductors is the strong chemical bond which makes the materials very stable and resist to degradation under conditions of high electric currents and intense light illumination (as encountered in the active regions of the device). The strong chemical bonds account also for the difficulty in introducing dislocations once the material is grown, thus removing one of the main mechanisms of degradation observed in other III–V compounds.

Amongst the disadvantages of the nitride materials, the most obvious one is the absence of suitable substrate materials for film growth (see Fig. 1.1); the high growth temperatures made necessary by the strong chemical bonding in these materials limit the choice of substrates to those that are stable at such elevated temperatures.The two most commonly used are sapphire ($\alpha - \mathrm{Al_2O_3}$) and silicon carbide ($\mathrm{6H - SiC}$). The large differences in lattice parameter and in linear thermal expansion coefficient relative to the substrates mean that poor–quality epitaxial films were expected. The first

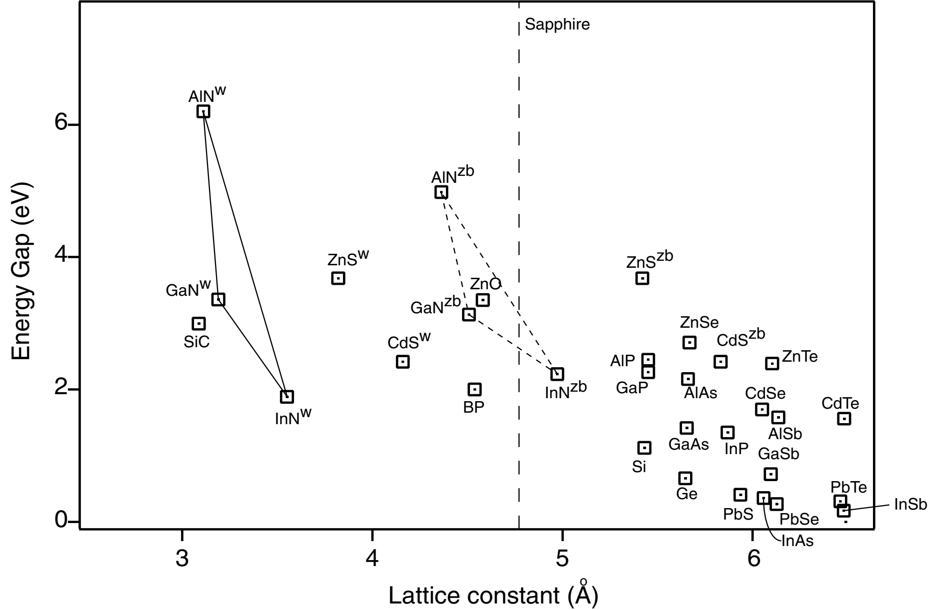

Figure 1.1: *The band gaps of common semiconductors versus lattice constants at room temperature. The superscript w means wurtzite phase and zb zinc blende phase. Vertical dashed line is the lattice constant of sapphire, the most common substrate material for GaN epitaxy growth.*

improvement of the GaN growth technique was the use of low temperature AlN buffer layers for GaN growth.[Yoshida et al., 1983; Amano et al., 1986] By using these nucleation layers, it became possible to obtain high-quality GaN films with a mirrorlike flat surface. However, even with this improvement, the defect density of the nitride thin films is still high. For example, in the commercial LEDs and laser diodes (LDs) based on nitride materials, the InGaN active layer in these devices includes a large number of threading dislocations, from 1×10^{8} to 1×10^{12} cm^{-1},[Nakamura, 1998] that originate from the interface between GaN and the sapphire substrate due to a large lattice mismatch of 15%. Most surprisingly, in spite of this large number of dislocations, the efficiency of the InGaN-based LEDs and LDs is much greater than that of the conventional III–V compound semiconductor (AlGaAs and AlInGaP)–based LEDs and LDs. In many conventional optoelectronic devices, the device performance has been limited by the control of both point defects and structural defects in these materials. However, these recent reports now suggest that III–V nitride based devices are less sensitive to dislocations than conventional III–V semiconductors.[Nakamura, 1998]

Another difficulty that hindered the development of nitride semiconductors was the preparation of p–type materials. Magnesium was expected to be a good acceptor; but although it was possible to incorporate significant concentrations of Mg in GaN, it did not effectively introduce hole charge carriers; the films were highly resistive. In 1989, Amano et al. demonstrated that low energy electron beam irradiation (LEEBI) activated Mg–doped GaN films,[Kito et al., 1989] converting them from a highly resistive state to one having a high concentration of holes (10^{16} cm^{-3}). This was sufficient to produce the first p-n junction blue LED.[Kito et al., 1989] However, the mechanism of LEEBI treatment was not clear by that time. In 1992, Nakamura et al.[Nakamura et al., 1992] obtained p-type GaN films by thermal annealing of GaN films in a nitrogen–ambient instead of the LEEBI treatment. Before thermal annealing, the resistivity of Mg–doped GaN films was 1×10^6 ohm · cm. After thermal annealing at temperatures above 700°C, the resistivity dropped to 2 ohm · cm. On the other hand, low–resistivity p–type GaN films, which were obtained by nitrogen–ambient thermal annealing, showed a resistivity as high as 1×10^6 ohm · cm after ammonia–ambient thermal annealing at temperatures above 600°C. Nakamura et al. therefore proposed that atomic hydrogen produced by ammonia dissociation at temperatures above 400°C was related to the acceptor compensation mechanism. A hydrogenation process whereby acceptor–H neutral complexes were formed in p–type GaN films was proposed. The formation of acceptor–H neutral complexes causes acceptor compensation. Theoretical calculations of this hydrogen passivation were made by Neugebauer et al.[Neugebauer and de Walle, 1994] in 1994 that clarify the hydrogenation process as the acceptor compensation mechanism.

Although commercialized blue LEDs and LDs have existed in the market for years, some fundamental problems are still unsolved. This thesis describe angle–resolved photoemission work that tries to investigate some of the fundamental issues related to group III–nitride semiconductors.

This thesis includes the following results:

- The preparation of a clean cubic indium nitride surface. The observed valence band dispersion was explained in terms of a pseudopotential band calculation.

- Growth of wurtzite GaN on 6H–SiC(0001) surface by means of MBE method with different nitrogen atom sources, e.g. ammonia or nitrogen

plasma. The *in situ* grown GaN thin films have been studied by LEED and ARPES and the film quality of different gas source is compared.

- The observation and mapping of the surface state that exist on the w–GaN(0001)–(1×1) surface grown by ammonia–assisted MBE.

- A study of w–AlN bulk band structure, and the comparison with theoretical band structure calculations.

- Investigations of the interface formation of SiC/GaN heterointerface. The resulting heterojunction is type II alignment. The valence band offset is consistent with the charge neutrality level model.

- A study of Ag/GaN and Ag/AlN Schottky barrier heights. The trend of the barrier height can be explained by virtual induced gap states model if it is nonreactive metal.

Chapter 2

Experimental Setup

The electronic properties of group–III nitrides are the main theme of these series of studies. I employed angle–resolved photoemission spectroscopy as the main tool to explore these properties. Low energy electron diffraction (LEED) was also used to investigate the structural order of these systems.

Molecular beam epitaxy is the only ultra–high vacuum compatible method that can grow group–III nitrides, with ammonia or nitrogen plasma as reactive nitrogen atom sources. We prepared GaN sample and studied the properties of these semiconductors *in situ*.

Here I described the details of the experimental setup in this chapter.

2.1 Photoelectron Spectroscopy

Electrons and photons are the most easily available probes with which to investigate matter. Hence, many spectroscopic techniques involve the use of these two types of particles. In a typical spectroscopic experiment, an electron or a photon in a well–defined state (energy, direction of propagation, polarization, etc.) impinges on a sample. As a result of the impact, electrons and/or photons escape from the sample. In any given spectroscopic technique, the state of one type of escaping particles is at least partially analyzed with a spectrometer.

Photoelectron spectroscopy (PES) is one of the spectroscopic techniques that utilizes these two particles to probe the properties of materials and is the most important experimental technique for studying the band structure

of occupied electronic states. In the PES experiment, photons (visible, ultraviolet (UV), X–rays, ...)are the incoming particles, and electrons are the outgoing particles to be analyzed. It is based on the photoelectric effect, which was first observed by Hertz[Hertz, 1887] in 1887 and explained later by Einstein[Einstein, 1905] in 1905 through the quantum nature of light.

The essential parts of the experimental set–up are a monochromatic light source, the sample contained in an ultra high vacuum (UHV) vessel to maintain clean surface conditions, and an electron energy analyzer, as illustrated in Fig. 2.1.

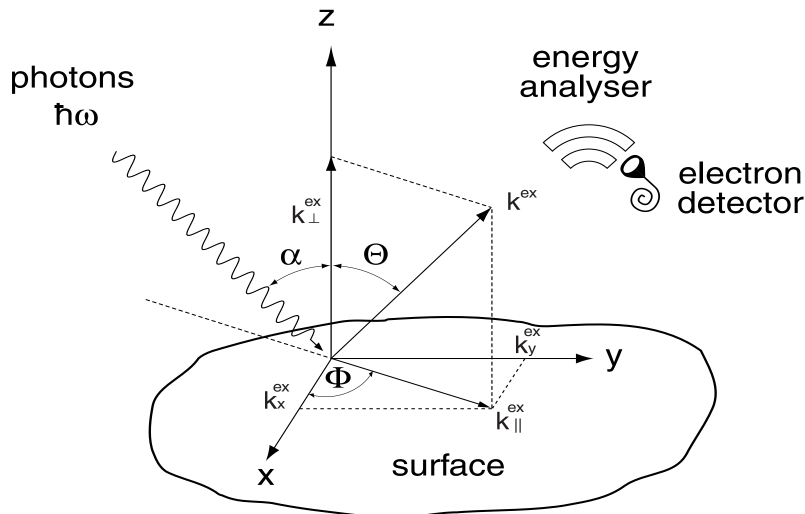

Figure 2.1: *Schematic representation of the photoemission experiment. Also show is the definition of the angles and wave vectors of the incident photon ($\hbar\omega$) and emitted electron.*

The emitted electrons are analyzed with respect to their kinetic energy. When photons in the ultraviolet (UV) spectral range are used, commonly using a gas discharge lamp with the following spectral lines: He (21.2 eV and 48.0 eV) or Ne (16.8 eV and 26.9 eV), the technique is called UPS (UV Photoemission Spectroscopy). Higher photon energies can be obtain with x–ray tubes (Al $K\alpha$:1486 eV and Mg $K\alpha$:1253 eV), in which case the method is called XPS (X–ray Photoemission Spectroscopy) or ESCA (Electron Spectroscopy for Chemical Analysis). To a large extent, however, these photon

sources are now being replaced by synchrotron radiation sources, which allows a continuous variation of the photon energy that cover the whole spectral range from the near–UV to the far x–ray regime.

All photoemission spectra in this work were recorded with a commercial hemispherical sector electron analyzer, ADES 400 from Vacuum Generators, with a nominal radius of 50 mm and an angular acceptance of 1.5°. The total energy resolution was determined from the width of the Fermi edge and varied between 90 and 150 meV. The light incidence was 45° to the sample normal, and the analyzer angle was varied with a two-axis goniometer.

2.2 Synchrotron Radiation

The data in this work were recorded at the Berliner Elektronenspeicherring-Gesellschaft für Synchrotron Strahlung mbH (BESSY I) and National Synchrotron Radiation Research Center (NSRRC), Taiwan. The monochromators used in BESSY I were the toroidal grating monochromator TGM 6 on an undulator beamline, providing photons of energies from 20 eV to 120 eV, and TGM 3 on a bending magnet, providing a similar photon energy range. The monochromator used in NSRRC was a low energy spherical grating monochromator (LSGM) on a bending magnet. This beamline covers the spectra range from 15 eV to 200 eV.

In such a facility, photons are produced as a result of the fact that a charged particle under acceleration emits radiation. A synchrotron radiation (SR) source consists of a storage ring in which bunches of electrons are circulating at relativistic speed in an ultra–high vacuum environment after being injected from an external accelerator. The electrons are kept in a closed orbit by means of strong bending and focussing magnets. In the bending sections they emit collimated radiation tangentially from the beam orbit. The total radiated power depends on the bending radius R, the electron energy E and the beam current I (at BESSY I 800 MeV and 200-800 mA; NSRRC are 1.5 GeV and 240 mA respectively) as:[Koch et al., 1983]

$$P \propto \frac{E^4 I}{R} \tag{2.1}$$

Radio frequency power is used to replenish the energy lost by radiation. The synchrotron radiation has a continuous frequency distribution, extending from the IR into the near x-ray regime, and is strongly in-plane polarized

in the orbital plane. The calculated flux vs. photon energy is shown in Fig 2.2.

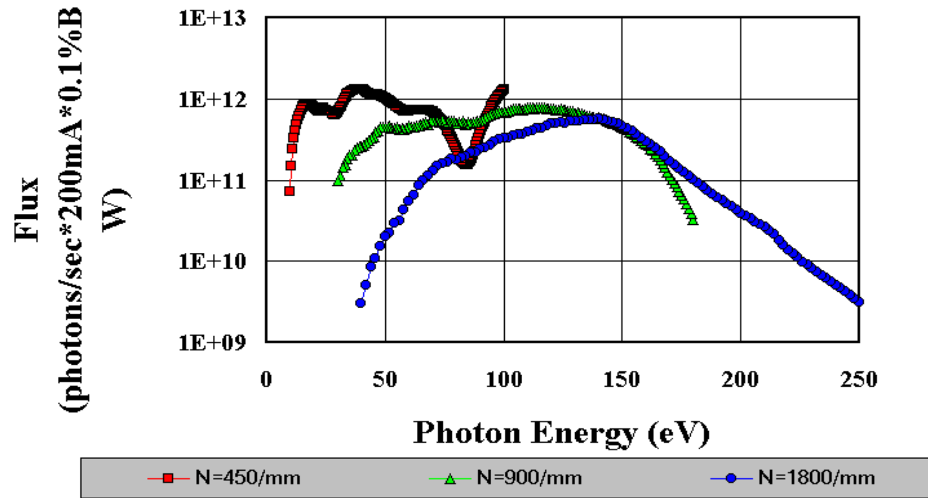

Figure 2.2: *The calculated photon flux versus photon energy of the LSGM beamline in NSRRC, Taiwan. (from NSRRC homepage.)*

Several experimental stations can be provided with radiation emitted from bending sections, undulators or wigglers of the storage ring. The bending magnet essentially is a magnetic dipole, that bends the electron beam through a short arc and produces a broad–band smooth spectrum. Wigglers and undulators are called insertion devices, that are inserted in the straight section of the storage ring. They are sequences of magnets with alternating polarities, as indicated in Fig. 2.3. A wiggler causes electron deflections that are large compared with the natural emission angle of SR, resulting in broad band emission of a fan–shaped beam of photons. Wiggler SR is similar to that produced by an individual bending magnet, but 2N times as intense due to repetitive electron bending over the length of a 2N–pole wiggler.[Ciocci et al., 2000] An undulator, on the other hand, causes small electron deflections, comparable in magnitude to the natural emission angle of the SR. The radiation emitted by an individual electron at the various poles in the magnet array interferes coherently, resulting in emission of a pencil–shaped beam of photons peaked in narrow energy bands at the harmonics of the fundamental energy. Due to the constructive interference, the radiation beam's opening

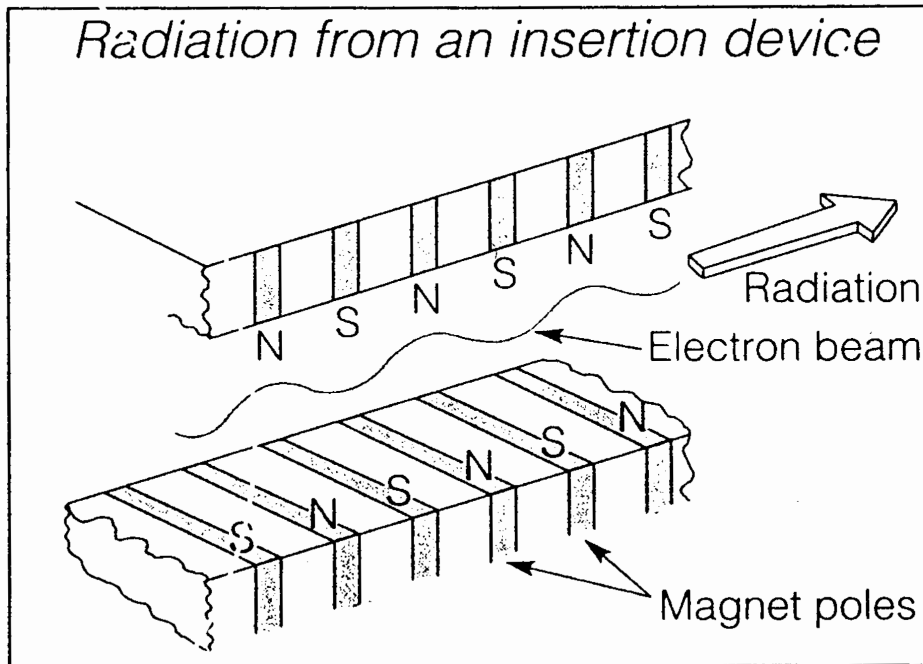

Figure 2.3: *Electrons wiggle or undulate in the midplane along the spatially periodic sinusoidal field in an insertion divice. After ref. [Winick, 1994]*

angle at any given wavelength is decreased by $\sqrt{\mathrm{N}}$ and thus radiation intensity per solid angle goes as N^2.[Winick, 1994] Figure 2.4 shows the typical on–axis photon spectrum from a bending magnet, a wiggler, and an undulator.[Winick, 1994]

All the beamlines connecting the ring with experimental stations are kept under UHV and equipped with a set of optical elements that constitute a monochromator. The high intensity of the broad spectrum emitted, together with the high degree of collimation and well defined polarization makes the synchrotron radiation source unique as a provider of high quality radiation for experimental use.

2.3 Low Energy Electron Diffraction

The analysis of diffraction patterns of low energy electrons scattered by surfaces of solids is a well established technique for the investigation of their surface periodicity. Electrons of kinetic energies in the range of 10 eV to

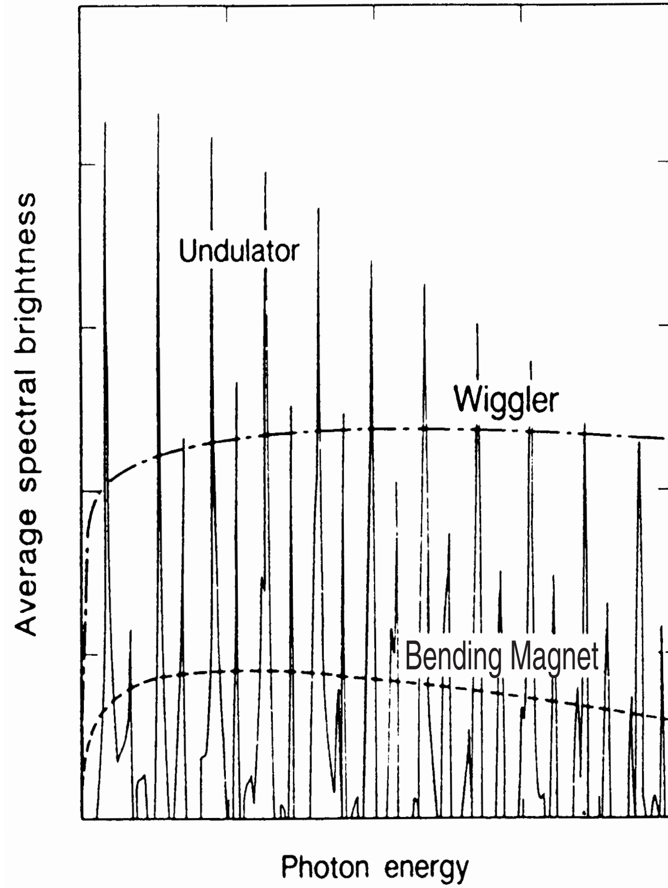

Figure 2.4: *Typical radiation spectra from a bending magnet, a wiggler, and an undulator. After ref. [Winick, 1994]*

300 eV have de Broglie wavelengths h/p comparable to interatomic distances [Davisson and Germer, 1927]. Illuminating a surface with a (quasi-)monoenergetic beam of such electrons will give rise to a well defined diffraction pattern of the elastically scattered electrons. As a result of the short mean free path of electrons in this energy region, this scattering only probes the surface layers of atoms. If only the uppermost atomic layer is involved in the scattering process, it can be shown that the diffraction spots appear when the parallel components of the wave vectors of incoming and outcoming electron waves fulfil the condition[Ertl and Küppers, 1985]

$$\mathbf{k}_{\parallel}^{out} - \mathbf{k}_{\parallel}^{in} = \mathbf{G}_{2D} \tag{2.2}$$

where $\mathbf{G}_{2D}$ is a reciprocal surface-lattice vector. That is, periodic structures on the sample lead to constructive interference of the backscattered electrons and the diffraction pattern is therefore a representation of the reciprocal lattice vectors of the surface.[Ertl and Küppers, 1985] Experimentally, a filament emits electrons which are accelerated by a variable voltage and focused on the sample surface with deflection electrodes. The diffracted electrons are retarded between a set of grids in front of a fluorescent screen, in order to discriminate inelastically scattered electrons. Finally, the electrons passing the grids are accelerated onto the fluorescent screen, where they are converted into visible intensity variations.[Ertl and Küppers, 1985]

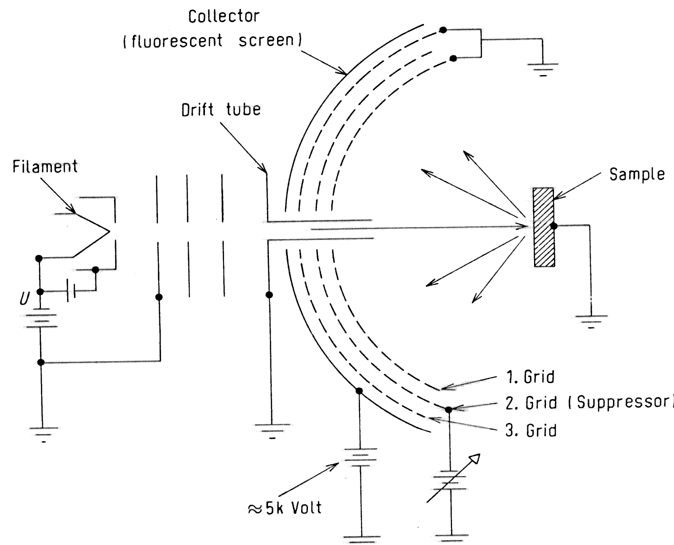

Figure 2.5: *Scheme of a LEED optics.*

The principle of construction of a typical LEED electron experiment is depicted in Fig.2.5. The diffraction patterns in this work were recorded with LEED optic from Omicron and Varian.

2.4 Molecular Beam Epitaxy

Evaporation and condensation of thin films under ultra–high vacuum (UHV) condition is a classical method to prepare a fresh clean surface. Depending on the substrate surface and on the evaporation conditions, subli-

mated films can be either polycrystalline or monocrystalline. If the film has a crystalline structure that is ordered with respect to that of the underlying substrate, we describe it as "epitaxial" and the preparation method is then called Molecular Beam Epitaxy (MBE). When the epitaxial films grows on a substrate of the same material, the film is "homoepitaxial"; alternatively, if grows on a substrate of a different material, it is called "heteroepitaxial".

The method of MBE is a specialized form of vacuum deposition. The MBE growth of semiconductor films takes place by the reaction of molecular beams of the constituent elements with a crystalline substrate surface held at a suitable substrate temperature under UHV conditions. The molecular beams are generated from sources contained in effusion cells, which are aimed at the heated substrate where the molecular beam flux intensity is accurately adjusted by the temperature within the effusion cell.[Cho and Arthur, 1975] Under UHV conditions, the thermal molecular beams emanating from effusion cells travel in nearly collision–free paths to the heated semiconductor substrate, the temperature provides sufficient thermal energy to the arriving atoms for them to migrate over the surface to lattice sites where they incorporate and start growing.[Cho and Arthur, 1975] MBE growth is carried out under conditions far from thermodynamic equilibrium, and is governed mainly by the kinetics of the surface processes occurring when the impinging beams react with the outermost atomic layer of the substrate crystal. This is in contrast to other epitaxial growth techniques, such as liquid phase epitaxy (LPE) or metalorganic chemical vapour deposition (MOCVD), which processes occur in the crystallizing phase surrounding the substrate.[Ambacher, 1998]

Gallium nitride films have been grown by variety of deposition methods, such as chemical vapour deposition (CVD) of gallium chloride with ammonia, MOCVD of trimethyl gallium with ammonia, or MBE. Among them, MBE is the only UHV compatible method such that we can *in–situ* study the film properties.

Unlike in solid–phase MBE, the metal atoms coming from conventional Knudsen effusion cells have to combine with a source of nitrogen atoms for nitride growth. Commonly, N_2 is employed as nitrogen source. Nitrogen at room temperature is almost an inert gas because of the triple bond between the two nitrogen atoms. The dissociation of one nitrogen molecule into reactive nitrogen atoms requires a relative high amount of energy:[Pauling, 1970]

$$9.81 \text{ eV} + N_2 \rightarrow 2N \tag{2.3}$$

Under the influence of a plasma at reduced pressure, a significant dissociation of the nitrogen molecules takes place. Atomic nitrogen is chemically very active even at room temperature and bonds with many metals creating various nitrides. Therefore, group III–nitrides can be grown by plasma–assisted molecular beam epitaxy, where the plasma–induced fragmentation of nitrogen molecules is combined with effusion cell–evaporated group III metal atoms on the substrate surface. Eddy et al. had demonstrated the growth of high quality GaN thin films by electron cyclotron resonance microwave–plasma–assisted MBE (ECR–MBE)[Eddy Jr. et al., 1993], and this method was studied extensively afterwards.[Ambacher, 1998] However, this rather sophisticated source can also cause some problems, for example, low growth rates, ion damage, contamination by sputtering effects, reproducibility problems, etc.[Mayer et al., 1997] Alternatively, NH_3 is a candidate as the nitrogen precursor for MBE to grow nitrides. The comparably low binding energy of NH_3 (3.85 eV) allows thermal dissociation at moderate temperature ($T \geq 500°C$). Injected NH_3 is cracked directly on the heated substrate surface,[Kamp et al., 1997] and the release of nitrogen atoms incorporated with metal atoms on the surface to form metal nitride.

The MBE cells attached in our chamber, developed by H. Haak at the FHI, consists of a boron nitride crucible, a heating circuit of ceramic-insulated tantalum wire and a water-cooled shielding and collimator. The temperature at the crucible is monitored with a thermocouple in order to stabilize evaporation rates. The temperature was regulated at $\pm 2°C$ while the sample was grown, for most elements this is equivalent to a flux regulation of $\pm 7\%$ or better.[Cho and Arthur, 1975] With a simple chamber arrangement (see figure 2.6), high quality GaN thin films were grown by both nitrogen sources. The film quality was studied by LEED optics and its electronic structure by angle–resolve photoemission spectroscopy.

2.5 Plasma Source

Other than solid, liquid and gas, plasma is called "the fourth phase of matter". It consists of a collection of free–moving electrons and ions. In a plasma, electrons acquire energy from the electric field and collide with gas molecules; electron collisions cause excitation and ionization of the gas molecules.

Figure 2.7(**a**) illustrates the principle of a radio frequency (rf) discharge.

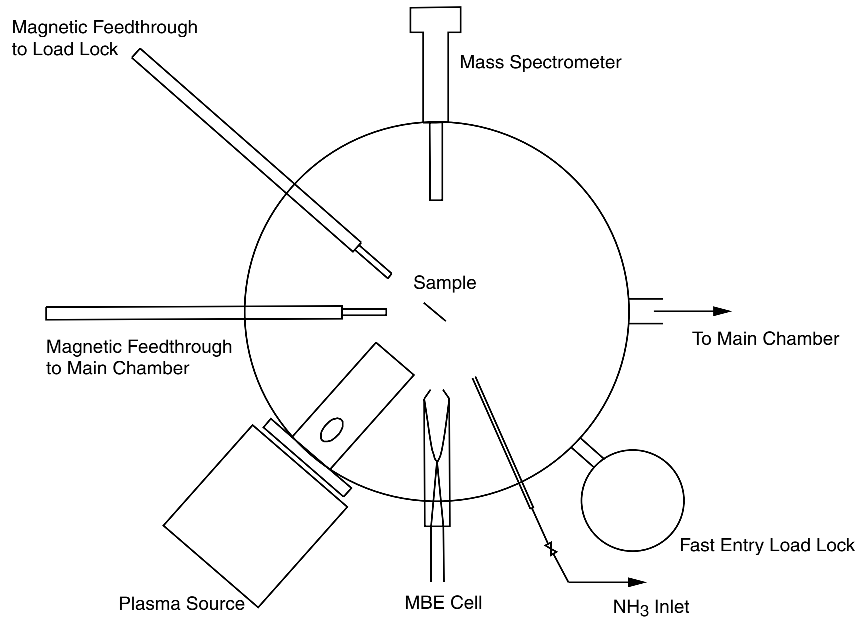

Figure 2.6: *The arrangement of the preparation chamber for sample preparation and growth. This chamber also equipped with turbomolecular and ion–getter pumps. The base pressure was always at* 10^{-10} *mbar range after bake out.*

The rf power, usually at a frequency of 13.56 MHz, is applied through a matching network and a coupling capacitor, which prevents conduction currents from flowing in the circuit.

A commercial rf plasma cell from Oxford Applied Research, UK., was employed in our system to generate an active nitrogen flux, Fig 2.7(**b**). The plasma source was operated at nitrogen flow rates which provided a downstream pressure in the chamber of 5×10^{-6} to 10^{-4} mbar range (base pressure of the chamber in order of 10^{-10} mbar). The design of the source promotes efficient electron–nitrogen collisions and results in a high–density plasma with gas ionization efficiencies as high as 10%.

The growth is carried out in the molecular flow regime, where the transport of atoms or molecules in both thermal beams from the effusion cell as well as the beam of activated nitrogen from the plasma source occurs in a collisionless manner.[Ambacher, 1998] In general, the nitrogen atoms created by the plasma source are not confined and reach the substrate because of the

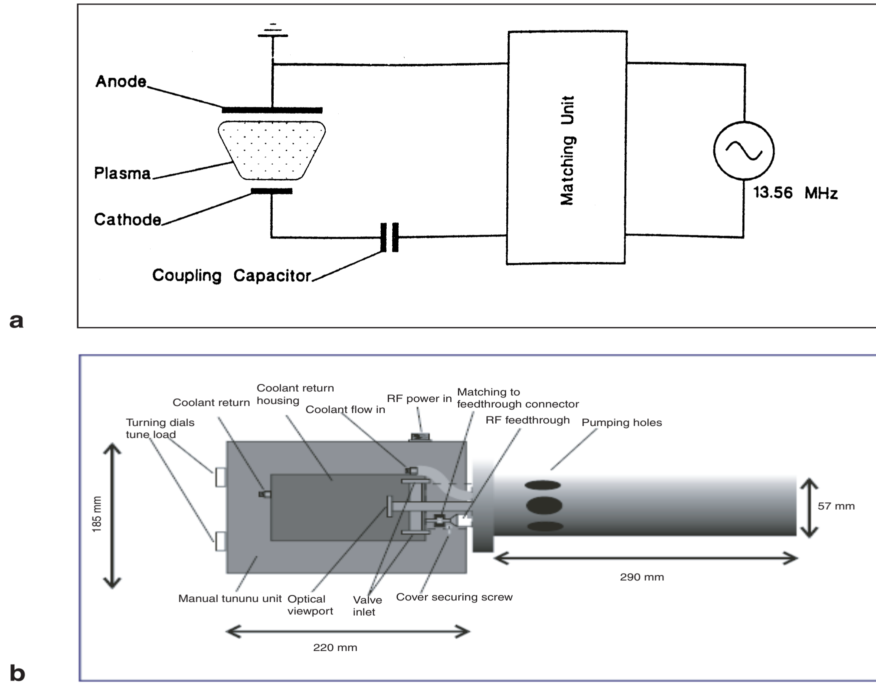

Figure 2.7: *(**a**)Illustration of a capacitively coupled radio–frequency discharge plasma formed between two plane electrodes. (**b**)The dimension and specification of the plasma source employed in our system.*

pressure difference between the plasma cell and the MBE chamber.[Molnar et al., 1995]

The damage threshold of GaN was estimated to be 24 eV[Wright, 1997], for an ECR source. The energy of the nitrogen ions can be high and the damage of the sample maybe severe, therefore an ECR source needs an extra magnetic field to divert the highly energetic ions from the substrate surface. On the other hand, nitrogen radicals leaving the rf plasma source have energies in the region of 2 eV so radiation damage can be neglected.

2.6 The vacuum system

The growth of well defined epitaxial films and their investigation with UV radiation can only be performed in ultra high vacuum. The stainless steel

or mu-metal vacuum chambers are equipped with turbomolecular, ion-getter and titanium sublimation pumps, as well as liquid nitrogen filled cold traps. A base pressure of 2×10^{-10} mbar is generally reached after careful bake out of the system at 120°-140°C and outgassing of all filaments and sample holders in the chamber. Pressure in the chamber was monitored at all moments with an ion gauge, and rest gas analysis was performed when necessary with a quadrupole mass spectrometer.

Since ammonia is a sticky gas and can spoil the vacuum easily, we attached a small preparation chamber with the main chamber for sample treatments. That small chamber was equipped with a plasma generator with nitrogen inlet, ammonia inlet, an MBE cell and quadrupole mass spectrometer to monitor the gas purity. With this chamber, a fresh sample can be prepared and introduced to the main chamber to conduct experiments without losing precious time to wait for the vacuum to recover.

A fast entry load–lock system with a three–stage magazine to load extra samples and two magnetic linear and rotary feedthroughs were connected with the preparation chamber, which allowed the fast introduction of new samples into the UHV system and transfer between the two chambers.

Positioning of samples in vacuum were conducted with manipulators in both chambers. The one in the main chamber had a cold finger in direct contact with the copper sample holder magazine, which can be filled with liquid nitrogen for sample cooling if necessary. Sample holders were pressed tightly in the magazine to guarantee a good electrical and thermal contact. Both manipulators had a heating wire and a thermocouple contact for current conduction and temperature reading. Samples could be moved in x, y, z, directions and polar angle. Samples were mounted on stainless steel sample holders, the upper and lower parts of the holder were electrically isolated with ceramics, so sample heating by direct current was possible. When necessary, a reference Fermi edge was measured on the lower part of the copper magazine, which was in good electrical contact with the sample. Before the Fermi edge measurement, the oxidized copper was scratched away with a wobble–stick.

Chapter 3

Basics

3.1 Electronic Bands

Isolated atoms have discrete allowed energy levels similar to those that exist for a particle in a one–dimensional well, a linear harmonic oscillator, or the hydrogen atom. When atoms come together to form a crystal,the distance between the atoms becomes comparable to or less than the spatial extension of the electronic wave functions associated with a particular atom; the consequence is that the electrons are no longer identifiable with specific atoms, but in a real sense belong to the crystal as a whole. The electron is a Fermion and obeys the Pauli exclusion principle; no two electrons can have the same identical set of quantum numbers, so in the larger environment of the crystal, no two electrons can have the same identical energy state, except for spin degeneracy.

The energy state of a $3s$ valence electron in sodium, for example, is the same in one isolated sodium atom as in another; in a sodium crystal, however, all the electrons that would have been identified as $3s$ valence electrons in the isolated atoms must now have different energies, for they all belong to the single system of the sodium crystal.[Slater, 1934] Thus when many atoms are brought together to form a solid, the number of electron states is conserved,[Harrison, 1989] there are 2.7×10^{22} atoms of Na in 1cm^3, there must be 2.7×10^{22} different energy levels, i.e., there must exist a bands of energy levels with small differences between individual levels.

What is true of the $3s$ electrons in sodium is true also of the $1s$, $2s$ and $2p$ electrons; they also belong to the whole crystal and require the formation of energy bands as a result of the interaction of sodium atoms forming a crystal.

The difference is that these are more tightly bound electrons, and therefore give rise to much narrower bands than that associated with the valence electrons. They interact less with each other since their wave functions do not overlap as much.

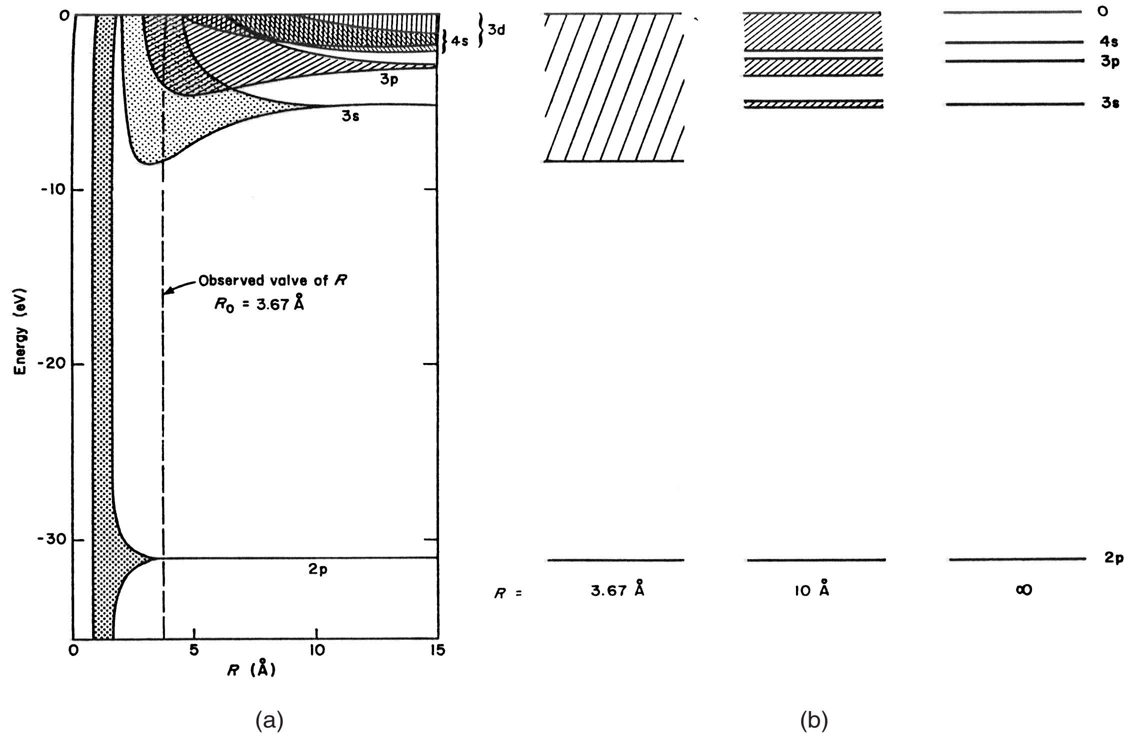

Figure 3.1: *Energy bands developing in metallic sodium as a function if the interatomic distance R. From Ref. [Slater, 1934]. (a) Bands broadening as the interatomic distance decreases. (b) Specific energy band formation for three values of R.*

The variation of the energy bands in sodium as a function of the spacing between sodium atoms is shown in Fig. 3.1. At large spacing, the energy levels are essentially the same as in the isolated sodium atom. As the spacing between atoms becomes smaller, these discrete atomic levels broaden into energy bands. Because the bands overlap, we can no longer properly refer to them as s or p bands, but must recognize that there is a mixing of s– and p–like wave functions. The energy curves bend upward again when the spacing is smaller than the observed equilibrium distance because of the growing repulsive energy between closely spaced atoms.[Slater, 1934]

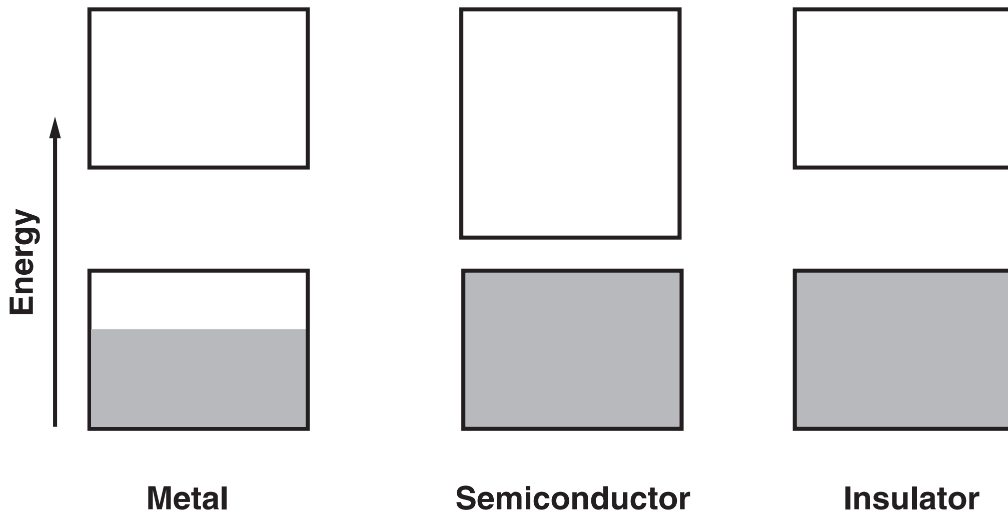

Figure 3.2: *Schematic electron occupancy of allowed energy bands for an insulator, semiconductor, and metal. The boxes indicate the allowed energy regions; the shaded areas are the regions filled with electrons. The main difference of semiconductor and insulator is size of the forbidden gap.*

Energy band formation strongly affects the electronic properties of materials. For example, electrons in a completely filled band can carry no current, this is the basis for the distinction between insulators (semiconductors) and metals: In the ground state of an insulator (or a semiconductor) all bands are either completely filled or completely empty; for metal at least one band is partially filled, as indicated in Fig. 3.2. The effective mass of electron as well as the electron velocity, and many other properties also depend on the band structure.[Ashcroft and Mermin, 1976; Kittel, 1986] Electronic bands are therefore the most fundamental aspects of matter that one should study in order to understand the properties of the material.

Angle–resolved photoemission spectroscopy is a most important technique to determine the electronic structure of materials.[Horn and Scheffler, 2000] This method probes the occupied states in momentum space, which can be mapped to the electronic band structure directly. In our studies, we mainly took the spectra in the normal emission direction; namely, we probed the electronic structure perpendicular to the sample surface, which is along the Γ–X direction in a face–centered cubic (fcc) crystal with (100) surface and the Γ–A direction in hexagonal close–packed (hcp) crystal with (0001) surface, as indicated in Fig. 3.3 (a) and (b).

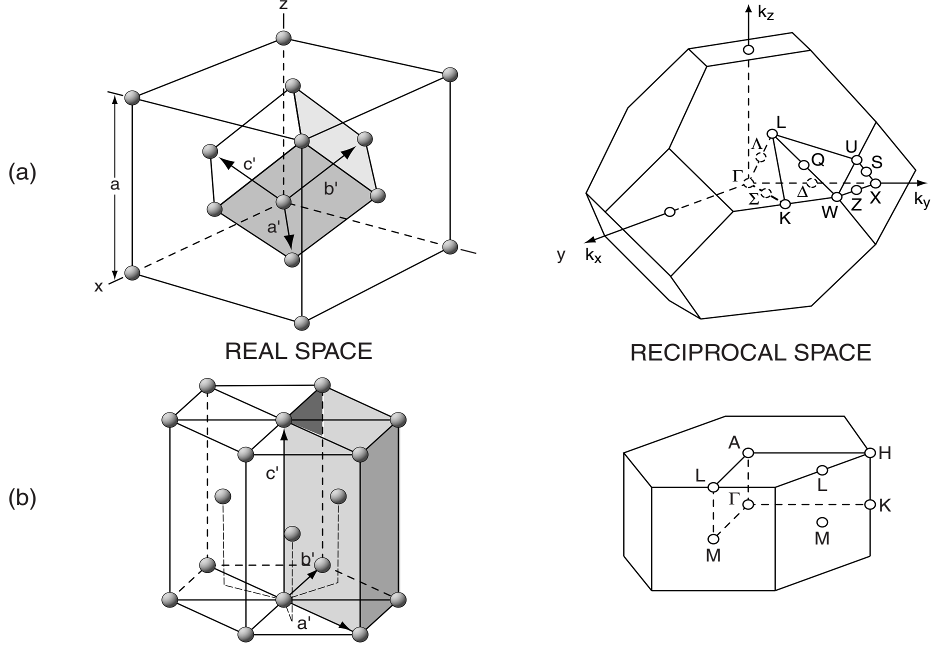

Figure 3.3: *Real and reciprocal lattices for (a) fcc and (b) hcp crystal structures. The normal emission for fcc (100) surface is along* Γ–X *direction and hcp (0001) surface is* Γ–A *direction.*

3.2 Photoemission Spectroscopy

In photoemission experiments, the solid surface is irradiated by mono–energetic photons with a relatively high energy ($\hbar\omega$). This causes electrons to be excited from occupied states (bands) into empty states of the quasi–continuum above the vacuum level. Provided these electrons have sufficient excess kinetic energy E_{kin} they can overcome the work function Φ and escape from the crystal. On account of the relation

$$\hbar\omega = \Phi + E_{kin} + E_b \tag{3.1}$$

a measurement of the spectrum $N(E_{kin})$ of the photoexcited electrons corresponds directly to a distribution of occupied electronic states (with binding energy E_b) in the solid, which is shown in Fig. 3.1.

Depending on the acceptance of the electron energy analyzer, PES can be separated into angle–integrated PES or angle–resolved PES (ARPES). If

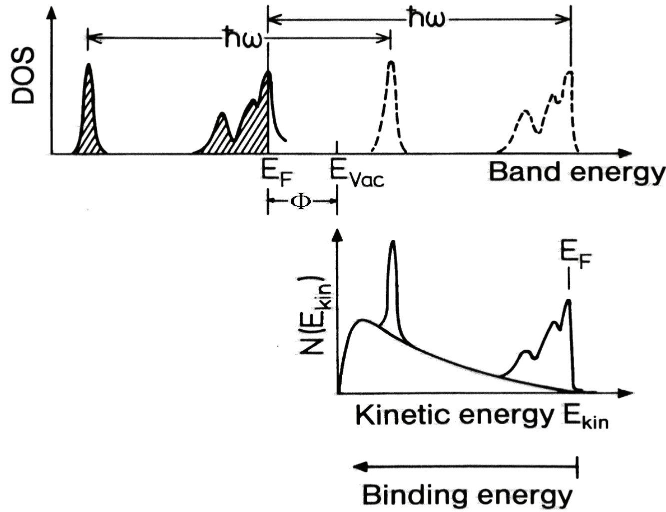

Figure 3.4: *Schematic illustration of the measurement of photoemission for a metal. The occupied states are shaded and the Fermi level E_F also show in the diagram. The electrons that are excited into the quasi–continuous empty states can escape from the crystal and are detected in the vacuum with their excess kinetic energy E_{kin}. The lower part shows the measured spectrum, the real signals are sat on the secondary electron background.*

in the photoemission experiment one uses an electron energy analyzer that accepts (in the ideal case) electrons within the whole half–space above the sample surface, then essentially one obtains the densities of occupied electronic states.[Woodruff and Delchar, 1994] In order to investigate the dispersion of electronic bands for bulk and surface states, a determination of the electron wave vector is necessary. Besides the kinetic energy one thus also needs to know the emission direction.[Lüth, 1997] This can be achieved by using an electron energy analyzer with a small angular aperture. This will of course strongly affect the counting efficiency. Since we mainly worked in ARPES mode, we will emphasize that category.

3.2.1 Angle–Resolved Photoelectron Spectroscopy

Since the exciting UV photon adds negligible momentum to the electron momentum, the photoexcitation process can then be specified as a transition from a particular state on the initial state energy surface (band) $\mathrm{E_i(k_\parallel, k_\perp)}$,

to a final state surface $E_f(k_{\parallel}, k_{\perp})$ where these locations differ in energy by the incident photon energy but are of the same value of k in the reduced zone scheme. With reasonable assumptions or the theoretical calculations of the final state band, one therefore should be able to determine the initial state inside the crystal. This is the reason why angle–resolved photoelectron spectroscopy is the most powerful experimental tool for investigation of the electronic structure of solids and surfaces.

The geometrical parameters in ARPES experiments are shown in Fig. 2.1, along with the definitions of the angles and wave vectors of the incident photons ($\hbar\omega$) and emitted electrons (e^-). The angle of incidence α of the photons with energy $\hbar\omega$, their polarization and the plane of incidence, determine the electronic field direction and the vector potential **A** of the photoexciting electromagnetic wave with respect to the crystal lattice. The wave vector $\mathbf{k^{ex}}$ of the emitted electrons is determined by its magnitude

$$k^{ex} = \sqrt{(\frac{2mE_{kin}}{\hbar^2})} \tag{3.2}$$

where E_{kin} is the kinetic energy of the detected electrons, and by the emission direction described by the angles ϕ and θ.

A rigorous theoretical approach to the photoemission process requires a full quantum–mechanical treatment of the complete coherent process in which an electron is removed from an occupied state within the solid and arrives at the detector. Theoretical approaches of this kind treat the photoeffect as a one–step process. The less accurate but simpler and more instructive approach is the so–called three–step model[Fan, 1945; Berglund and Spicer, 1964] in which the photoemission process is artificially separated into three independent parts, see Fig. 3.5[Hüfner, 1995]:

1. Optical excitation of an electron from an initial into a final electronic state within the crystal.

2. Propagation of the excited electrons to the surface with concomitant production of secondary background.

3. Electron penetrate the surface (barrier) escape into the vacuum and collected by the detector.

This separation of stages is somewhat artificial and the whole process of photoexcitation should be treated as one step. However, the division of the process into distinct steps can be justified reasonably well and a one–step

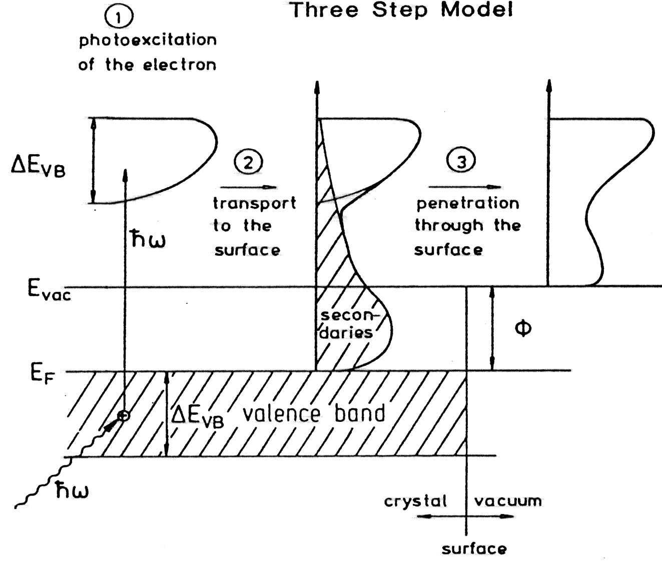

Figure 3.5: *The three–step model: (1) photoexcitation of electrons; (2) travel to the surface with concomitant production of secondaries (shaded); (3) penetration through the surface (barrier) and escape into the vacuum. From reference[Hüfner, 1995].*

theory actually gives results that are not very different from the conceptually much simpler three–step model.[Hüfner, 1995]

Step 1. Optical excitation of an electron within the crystal

Neglecting the momentum of the photon, which is always true in the photon energy range we are interested, the optical excitation is a direct transition (momentum conserving or vertical transition) in the reduced zone scheme, Fig. 3.6.

The internal energy distribution of photoexcited electrons $\mathrm{I^{int}(E, \hbar\omega)}$ can be described by Fermi golden–rule transition probability for optical excitation,[Lüth, 1997]

$$\mathrm{I^{int}(E,\hbar\omega) \propto \sum_{f,i} |<f,\mathbf{k_f}|\mathscr{H}|i,\mathbf{k_i}>|^2 \delta(E_f(\mathbf{k_f}) - E_i(\mathbf{k_i}) - \hbar\omega)\delta(E - [E_f(\mathbf{k_f}) - \Phi])} \tag{3.3}$$

where E is the final kinetic energy of the electrons and $\hbar\omega$ the photon energy, $\mathrm{E_f(\mathbf{k_f})}$ and $\mathrm{E_i(\mathbf{k_i})}$ denote the energies of the final bands $|\mathrm{f}, \mathbf{k_f}>$ and the

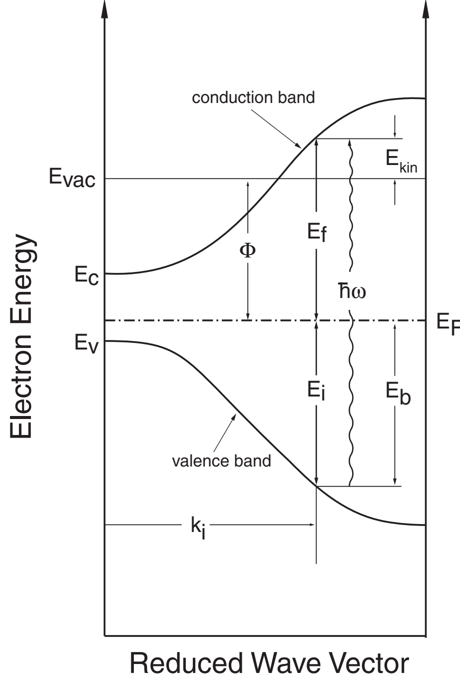

Figure 3.6: *Representation of the photoexcitation process in the electronic band scheme. Only the direct transition are taken into account. The energies of the initial state* $\mathrm{E_i}$ *and final state* $\mathrm{E_f}$ *are referred to the Fermi level* $\mathrm{E_F}$.

initial bands $|\mathrm{i}, \mathbf{k_i}>$, respectively. $|<\mathrm{f}, \mathbf{k_f}|\mathscr{H}|\mathrm{i}, \mathbf{k_i}>|^2$ is the square of the transition matrix element of the perturbation operator:

$$\mathscr{H} = \frac{1}{2mc}(\mathbf{A} \cdot \hat{p} + \hat{p} \cdot \mathbf{A}) \tag{3.4}$$

$\mathbf{A}$ is the vector potential of the exciting electromagnetic field, and $\hat{p} = -i\hbar\nabla$, is the momentum operator of the electron. The first delta function in Eq. 3.3 imposes energy conservation during the first step, and the second delta function ensures that the kinetic energy measured outside the sample equals the final state energy inside minus the work function.

Step 2. Propagation of the electron to the surface

In this step, the photoexcited electrons propagate to the surface. In the process a large number of electrons undergo inelastic scattering; they lose part of their energy $\mathrm{E_f}$(or E) by electron–plasmon or electron– phonon scattering. Such electrons contribute to the continuous background in the PE spectrum which is called "the true secondary background"; they have lost the information about their initial electronic level $\mathrm{E_i}$.

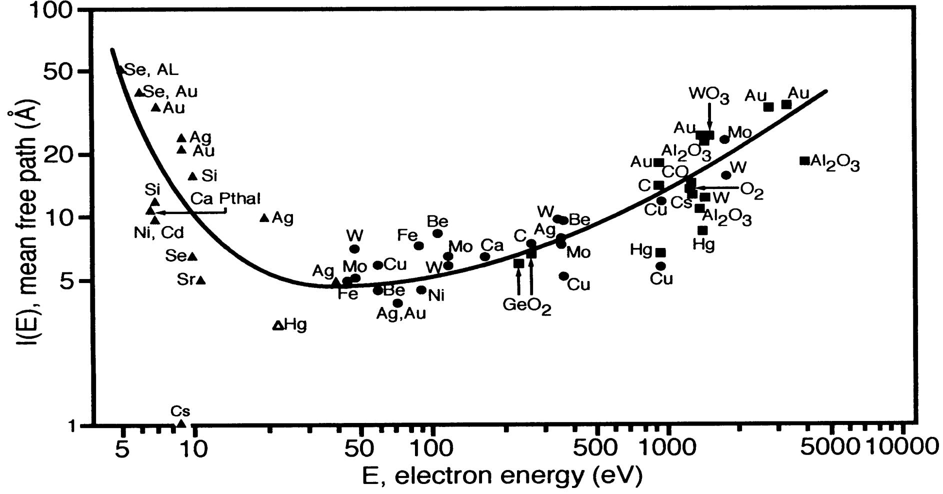

Figure 3.7: *Escape depth versus kinetic energy of the electron and measured for different materials.*

The probability that an electron will reach the surface without inelastic scattering is given phenomenologically by the mean–free path λ. λ is strongly dependent on kinetic energy of the electron but normally rather insensitive to the choice of the host material, see Fig. 3.7. The value of λ is typically between 5 to 20 Å, thus limiting the information depth to this spatial region and makes PE a surface sensitive technique.

Step 3. Escape of the electron into vacuum

The escaping electrons are those for which the component of the kinetic energy normal to the surface is sufficient to overcome the surface potential barrier; the other electrons are totally reflected back into the bulk. Inside the crystal, the electron travels in a potential of depth $\mathrm{E_v - E_0}$, Fig. 3.8, $\mathrm{E_v}$ is the vacuum level and $\mathrm{E_0}(< 0)$ is the energy of the bottom of the valence band. For escaping into the vacuum, the electrons must satisfy the following condition:

$$(\frac{\hbar^2}{2\mathrm{m}})(\mathrm{k}_\perp^{\mathrm{ex}})^2 \geq \mathrm{E_v - E_0} \tag{3.5}$$

$\mathbf{k}_\perp^{\mathbf{ex}}$ is the component normal to the crystal surface of the wave vector $\mathbf{k}^{\mathbf{ex}}$ of the excited electron. Because of the two dimension translational symmetry, the transmission of the electron through the surface into the vacuum requires

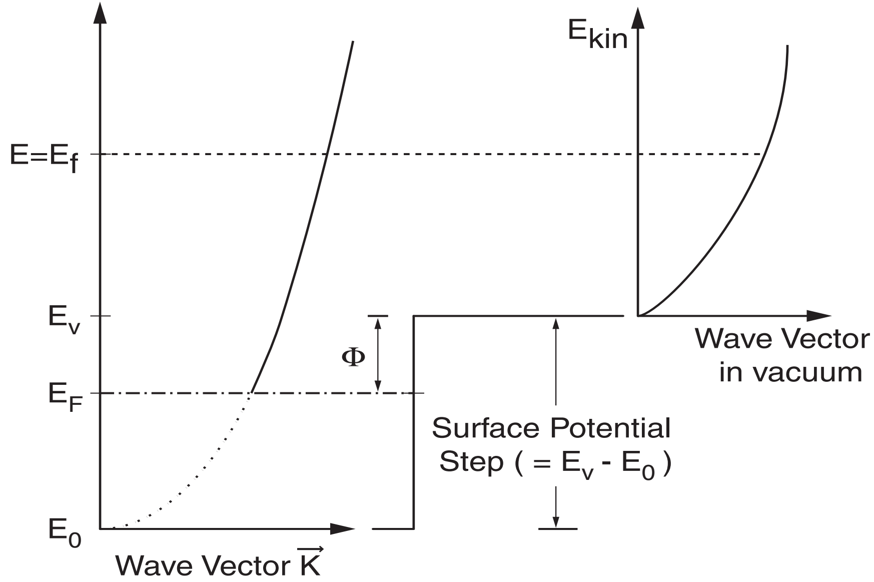

Figure 3.8: *Schematic representation of the surface potential barrier. The electrons must overcome this barrier to escape into vacuum.* $\mathrm{E_o}$ *is the bottom of the valence band,* $\mathrm{E_F}$ *the Fermi level,* $\mathrm{E_v}$ *the vacuum level,* Φ *the work function of the material.*

conservation of its wave vector component parallel to the surface, Fig. 3.9:

$$\mathbf{k}_{\|}^{\mathrm{ex}} = \mathbf{k}_{\|} + \mathbf{G}_{\|} \tag{3.6}$$

where $\mathbf{k}$ is the wave vector of the electron inside the crystal, $\mathbf{G}$ is the reciprocal lattice vector.

The normal component of the wave vector $\mathrm{k}_{\perp}$ is not conserved during transmission through the surface. For the external electron on the vacuum side, the kinetic energy and wave vector has the following relation:

$$\mathrm{E_{kin}} = \frac{\hbar^2}{2\mathrm{m}}(\mathrm{k}^{\mathrm{ex}})^2 = \frac{\hbar^2}{2\mathrm{m}}[(\mathrm{k}_{\perp}^{\mathrm{ex}})^2 + (\mathrm{k}_{\|}^{\mathrm{ex}})^2] \tag{3.7}$$

With ARPES, the wave vector component parallel to the surface outside the crystal can be determined from known experimental parameters:

$$\mathrm{k}_{\|}^{\mathrm{ex}} = \sqrt{\frac{2\mathrm{m}}{\hbar^2}\mathrm{E_{kin}}}\ \sin\theta \tag{3.8}$$

therefore directly yields the internal parallel wave vector component $\mathrm{k}_{\|}$. On the other hand, due to the inner potential, the wave vector component normal

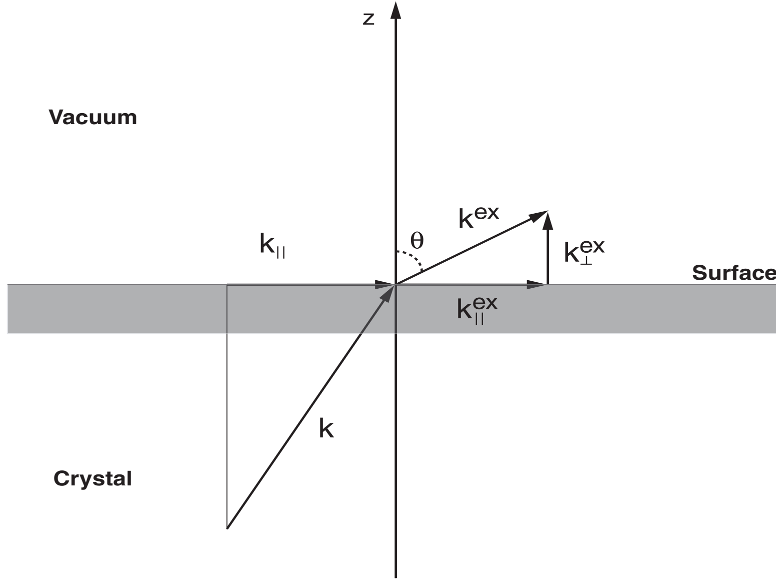

Figure 3.9: *Momentum relations at the solid–vacuum interface. Conservation of the wave vector component* $\mathbf{k}_{\|}$ *(parallel to the surface) upon transmission of the emitted electron through the surface.*

to the surface $k_{\perp}$ of the electron inside the crystal is changed upon transmission through the surface. One can determine the outside component by eq. 3.7 and Fig. 3.9 as:

$$k_{\perp}^{ex} = \sqrt{\frac{2m}{\hbar^2} E_{kin}} \cos\theta \tag{3.9}$$

However, without a detailed knowledge of the electronic band structure for energies above vacuum level and of the inner potential (usually not exactly known) information about the inner wave vector component $k_{\perp}$ can not be obtained.

To determine the complete momentum vector directly from the angle–resolved experiment, one therefore has to find the momentum transfer perpendicular to the surface. Let us assume that we know the final state band dispersion $E_f(k_{\perp}^f)$ to some degree, and we are interested in the initial state band dispersion $E_i(\mathbf{k_i})$. By measuring the electron energy E in vacuum, which is equal to E_f in the solid, we can invert the E_f to obtain the initial state band dispersion in the vertical transition case:(Fig. 3.10)

$$k_{\perp}^i = k_{\perp}^f = k_{\perp}^f(E_f) = k_{\perp}^f(E) \tag{3.10}$$

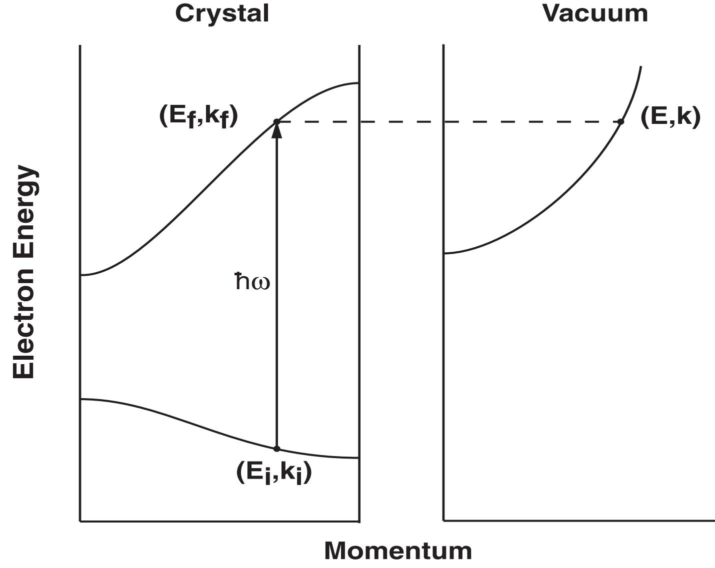

Figure 3.10: *Schematic representation of the vertical transition model, see text for detail.*

The final state is usually approximated by either the unoccupied states of the material (ground state conduction bands) or by free electron final states placed at a suitable relative energy. The latter one is the simplest approximation for the final state $(\mathrm{E_f}, \mathbf{k_f})$, which is a parabolic band in a constant inner potential $\mathrm{E_0}$

$$\mathrm{E_f}(\mathbf{k_f}) = \frac{\hbar^2 \mathrm{k_f^2}}{2\mathrm{m}} - \mathrm{E_0} \qquad (\mathrm{E_0} > 0) \tag{3.11}$$

This model was the first to be used for a direct determination of 3–D energy bands[Stöhr et al., 1978] and has been successfully used in many cases.[Chiang et al., 1980; Thiry et al., 1979] The bottom energy of this parabola, i. e. inner potential, is used as an adjustable parameter which is fitted to give the best agreement with the observed dispersion effects.[Horn et al., 1984]

By inverting Eq. 3.11 and referring to Fig. 3.9, one obtains

$$\mathrm{k_\perp^i} = |\mathbf{k_f}(\mathrm{E_f})| \cos\theta = \sqrt{\frac{2\mathrm{m}}{\hbar^2}(\mathrm{E}+\mathrm{E_0})} \cos\theta = 0.51\text{Å}^{-1}\sqrt{(\mathrm{E}+\mathrm{E_0})} \cos\theta \tag{3.12}$$

θ is the angle between surface normal and the outgoing electron. Eq. 3.12 essentially describes the refraction of the outgoing photoelectron when it

crosses the potential step E_0 at the surface.

With the free–electron–final band approximation as premise, and by combining Eq. 3.8 and Eq. 3.12, one can determine the electronic structure of materials by using ARPES.

Chapter 4

Electronic Structure of Group III-Nitrides

The electronic energy bands in a solid represent the basic electronic structure of the solid just as the atomic term values in the free atomic represent the basic electronic structure of the atom. It is thus the most fundamental property one has to clarify in order to really understand the properties of the material.

We have applied ARPES to study the electronic band structures of the group–III nitride semiconductors. Since photoemission is a surface sensitive technique, a well ordered surface is critical for the experiments. It is well known that good surface quality of nitride semiconductors is difficult to achieve, we will therefore describe the cleaning and growing processes for these semiconductors.

The band structures we have studied include cubic InN, wurtzite GaN, and wurtzite AlN. For GaN, we also compare the effect of different nitrogen sources we applied during the crystal growth.

4.1 Cubic Indium Nitride

The energy of the band gap of group III–nitride semiconductors can be varied by mixing the nitrides to their ternary combinations to form the nitride alloys. The key component for the band gap engineering in the visible range is indium nitride. Using AlGaN or GaN as the barrier or cladding layers and GaN or InGaN as active layers, quantum wells and superlattices can

be fabricated, these quantum wells and superlattices are the constructing blocks for the modern short wavelength optoelectronic devices.[Ponce and Bour, 1997]

InGaN quantum wells are indispensable for nitride–based light emitting devices since the high–efficiency devices can be realized only by an InGaN active layer for the light–emitting diodes (LEDs) and laser diodes (LDs).[Nakamura, 1998] When the active layers of the LEDs is GaN or AlGaN, the efficiency of LEDs is considerably lower.[Mukai et al., 1998] The reason why InGaN–based LEDs are so efficient despite the large number of threading dislocations has not yet been clarified.[Nakamura, 1998; Lester et al., 1995]

It is well known that for group III–nitride semiconductors, the thermodynamically stable phase is the hexagonal wurtzite structure (α–phase). Beside it, a metastable β–phase with cubic zinc blende structure also exist.[Ambacher, 1998] It has been argued that c–InN inclusions in the w–InGaN quantum well layer should be the active media in the light emitting process.[Weinstein et al., 1998] Thus, the investigations on the properties of c–InN are important for the applications based on both zinc blende and wurtzite phases of group III–nitride semiconductors.

The growth of all nitride semiconductors suffers form the lack of suitable substrate materials, it is especially a serious problem for InN, since it also has the lowest thermal stability in the nitride family. Decomposition of the surface of the thin film sample in vacuum was found to begin at 1050°C for AlN, 850°C for GaN,[Ambacher et al., 1996] and 550°C for InN.[Guo et al., 1993] Due to this rather poor thermal stability, InN crystal cannot be grown at the high temperature required by CVD growth processes, which is the most popular nitride growth approach.[Strite and Morkoç, 1992] This is the main reason that only few experimental results have been published concerning the growth and characterization of cubic InN.[Strite et al., 1993]

4.1.1 The Growth of c–InN

The cubic InN samples we measured were grown and characterized by Prof. Lischka's group.[Lima et al., 1999] They were grown by the plasma–assisted MBE method on GaAs(001) substrates with an InAs buffer layer. The GaAs(001) substrates were first deposited 500 nm GaAs buffer layer at 600°C under (2×4) reconstruction, then 300 nm of InAs was grown at 480°C

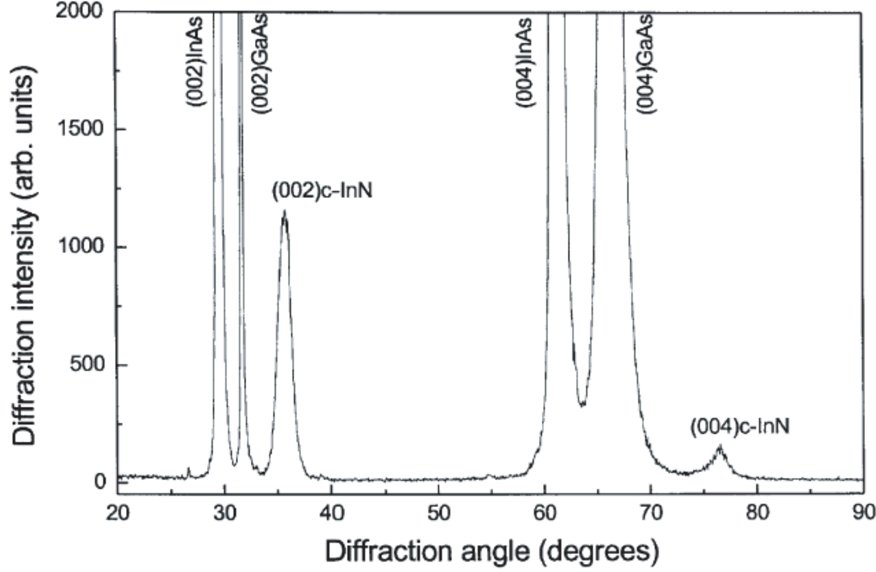

Figure 4.1: *XRD pattern of the c–InN films on InAs/GaAs(001) substrates. The cubic phase of the InN layer in this spectrum is identified by the presence of diffraction peaks at 2θ =* 76.4° *and* 36.1° *originating from the zinc blende type InN (004) and (002) planes, respectively. From ref. [Lima et al., 1999].*

with (2×4) reconstruction to ensure As–stabilized condition. Prior to InN growth, the InAs(001) surfaces have to be exposed under nitrogen flux in order to produce a N–As anion exchange, and to form the c–InN nucleation layers. The c–InN overlayers were grown after the nitridation process and at 450°C substrate temperature. The growth rate was 80 nm/h.

At first sight this InN/InAs system seems unrealistic, since the lattice constants for c-InN and InAs are 4.98 Å[Lima et al., 1999; Strite et al., 1993] and 6.06 Å[Sze, 1981], respectively. The lattice mismatch is then as large as 17.8%. Yet epitaxial growth at this extreme mismatch is shown to result from a coincidence lattice between InAs and InN. This is similar to cubic GaN grown on GaAs(001) surface, which system has 20% lattice mismatch.[Trampert et al., 1997] The mismatch between InN and InAs (the same as GaN and GaAs) is seen to be relieved by Lomer dislocations formed at every six (five) overlayer interatomic distances, this regular spacing is along [110] directions.[Ding et al., 1997] This coincidence leads to a residual misfit $f = (na_{overlayer} - ma_{substrate})/(ma_{substrate})$ of only -1.34% for c–

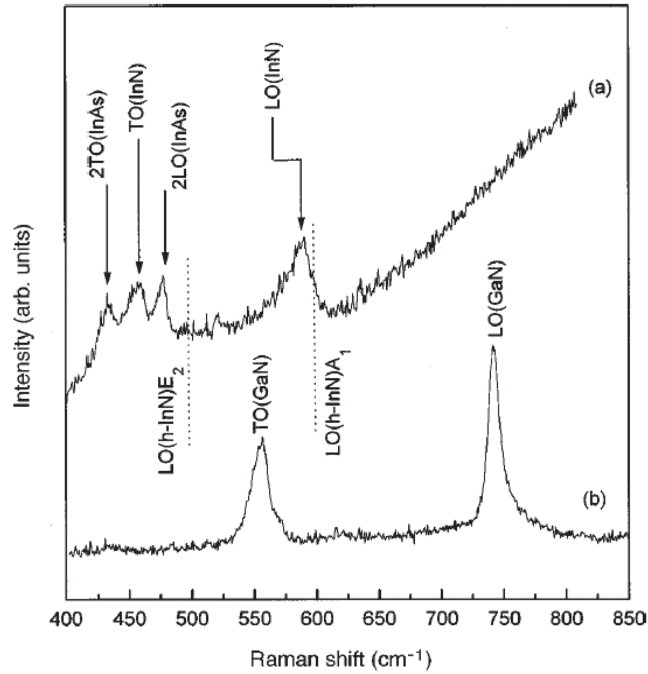

Figure 4.2: *Room temperature micro–Raman spectra of c–InN sample (a) and of c–GaN sample (b) from ref. [Tabata et al., 1996] for comparison. The dashed lines are the two most intense phonon peak positions for wurtzite InN[Kwon et al., 1996]. From ref. [Tabata et al., 1999].*

InN/InAs system; (n,m) = (6,5), and -0.02% for c–GaN/GaAs system; (n,m) = (5,4)[Trampert et al., 1997]. For the InA/InAs system this means every 5 InAs can accommodate 6 InN interatomic distances and relieve the interface strain. The occurrence of a coincidence mismatch between cubic InN and InAs provides a basis for epitaxial growth for a material combination with such a large lattice mismatch where epitaxy of covalently bonded materials is usually no longer achieved.[Trampert et al., 1997]

The films grown by Prof. Lischka's group were characterized by X–ray diffraction (XRD) measurements; (see Fig. 4.1), that shows a zincblende type InN, and from this the lattice constant of c–InN is (4.98±0.01) Å,[Lima et al., 1999] in good agreement with the data in the literature.[Strite et al., 1993]

Figure 4.2 shows a room temperature micro–Raman spectra of the c–InN/InAs/GaAs film and the c–GaN sample for comparison.[Tabata et al., 1999] The dashed lines indicate the peak positions for wurtzite InN,[Kwon

et al., 1996] where no peak exist. This is also evidence that shows the cubic phase of the InN thin films.

4.1.2 The Cleaning Process

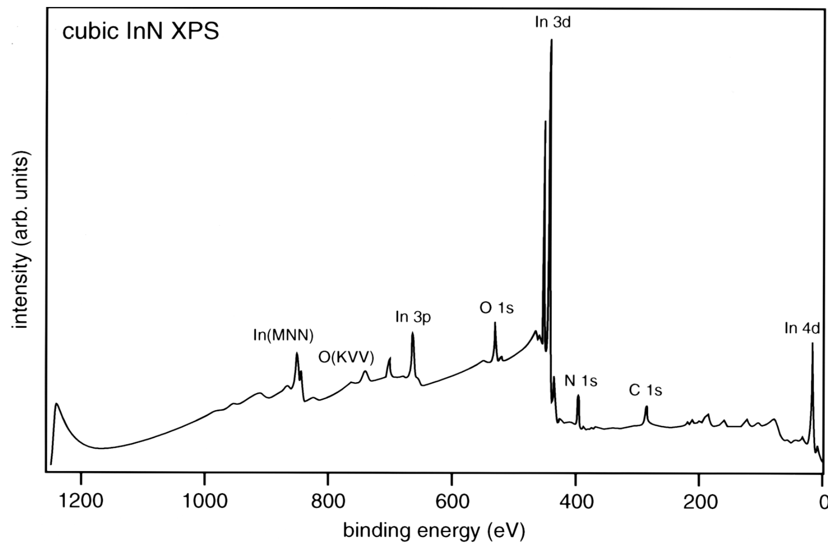

Figure 4.3: *X–ray photoelectron spectrum from as–inserted cubic indium nitride using Mg kα radiation ($\hbar\omega$ = 1253.6 eV).*

The as–inserted cubic InN XPS spectrum, recorded with Mg $K\alpha$ radiation ($\hbar\omega = 1253.6$ eV) is shown in Fig. 4.3. The indium (In *4d*, In *3d*, and In *3p*), nitrogen (N *1s*), and oxygen (O *1s*) as well as In(MNN), O(KVV) Auger emissions are indicated in the figure. The XPS spectra were taken from a laboratory based conventional ESCA spectrometer. This spectrum is identical to the XPS spectrum from oxygen and carbon contaminated wurtzite InN.[Guo et al., 1998]

The c–InN sample was loaded into the vacuum chamber after a brief etch in 25% HCl for 10 seconds with a subsequent rinse in distilled water. We then tried many different methods to clean the c–InN surfaces to remove the surface contamination and restore the crystalline order. Mild vacuum

annealing was the first attempt. After the annealing the valence band region was still featureless and an As *3d* peak started showing up. This treatment did not restore the crystalline order, instead it made the substrate arsenic diffuse to the surface. Further annealing only made things worse. We then tried neon ion bombardment (0.5 kV, 11μA sample current for 5 min.) with post annealing at 500°C for 5 minutes. After this treatment, the As peak was lower but still existed, a metallic Fermi edge occurred, as shown in the lower spectrum in Fig. 4.4. This indicated that the nitrogen atoms on the InN surface were preferably sputtered by the noble gas ion bombardment, the remained indium then formed metallic clusters on the surface, those clusters were the origin of the Fermi edge in the spectrum.

Nitrogen ion sputtering was reported to remove the oxide layer on the GaN surface without significant modification of the nitrogen to gallium atomic ratio[Hunt et al., 1993], and can suppress the formation of nitrogen vacancies[Ishikawa et al., 1997] on the GaN surface. We therefore applied this method on the indium covered InN surface, hoping to remove the surface indium island as well as the diffused arsenic, and the energetic nitrogen ions can restore the surface nitrogen atom losses.

This method did not bring the expected result either. We bombarded the sample with 0.5 kV, 5μA and 7μA of nitrogen ions for 5 minutes each. The situation did not improve at all, a Fermi edge was always present in the spectra. The binding energy of In–N and Ga–N bonds are 1.93 eV and 2.2 eV, respectively,[Edgar, 1994] hence the In–N bond is much weaker than Ga–N bond. The ion bombardment is fine for GaN but maybe is too strong for InN; the high energy ions may break up the In–N bond more efficiently, or at least as efficiently as removing the surface contaminations, the In clusters therefore always existed and so did the metallic Fermi edge.

After all the treatments failed, our next attempt was annealing the sample under an ammonia atmosphere for 10 minutes. The sample was kept at 450°C, and NH_3 pressure was 1.5×10^{-6} mbar. The ammonia molecules cracked on the hot sample surface and released nitrogen atoms, the free nitrogen atoms then reacted with surface indium and formed InN again. This is indicated in the upper spectrum in Fig. 4.4. The Fermi edge was removed by this treatment, and restored the semiconductor–like valence band maximum with some gap emission between the leading peak of the valence band and the Fermi level. Those states we assigned to defect states; they are frequently observed in the nitride semiconductor photoemission experiments. The LEED showed only a blurred (1×1) pattern with diffuse background;

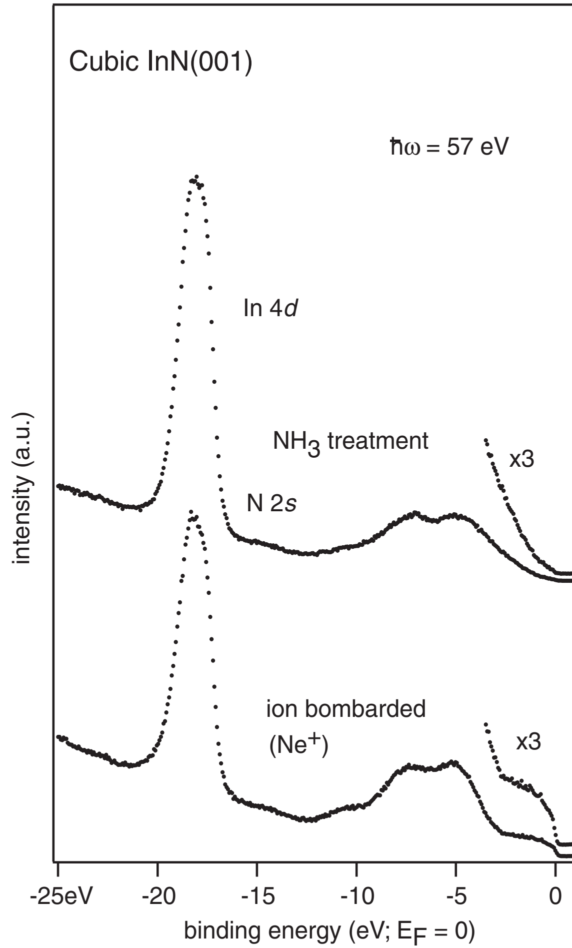

Figure 4.4: *Comparison of different sample preparation methods for c–InN(001). Spectra recorded at normal emission condition at photon energy of 57 eV. Note the metallic Fermi edge was removed after the ammonia treatment. See the text for details.*

Fig. 4.5, which also indicates a less–than–perfect surface quality.

4.1.3 ARPES Studies

For zincblende (001), normal emission ARPES probes states with momenta along the $\Gamma - \Delta - X$ symmetry line in the bulk Brillouin zone, see Fig. 3.3. Fig. 4.6 shows a set of normal emission valence band spectra recorded with different photon energy from 27 to 53 eV. A mixed polar-

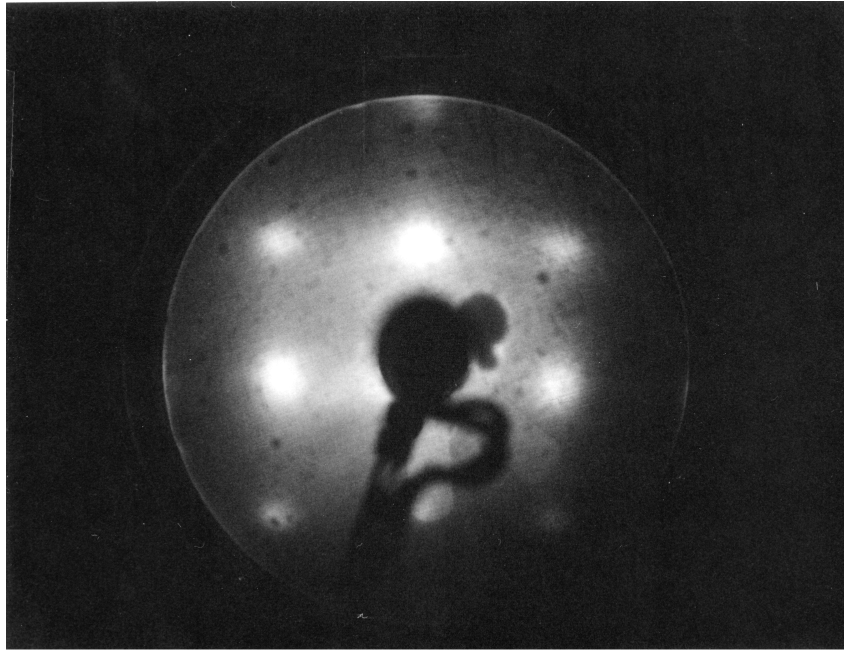

Figure 4.5: *The* (1×1) *LEED pattern took from the ammonia treated cubic InN surface, the electron beam energy was 70.4 eV. It shows blur spots with high background, which means the surface quality was not perfect, but we can still see the cubical structure.*

ization was always used such that all valence states were excited regardless of symmetry. At the photon energy range applied in these experiments, the photoemission spectral peaks can be roughly classified into two categories: primary cone emission peaks and secondary cone–surface umklapp emission peaks.[Chiang et al., 1980; Mahan, 1970] The primary cone emission peaks exhibit a shift with respect to the Fermi level upon change of photon energy, and the transitions giving rise to these peaks are **k**–conserving. The final states for these excitations usually can be well described by a free–electron dispersion which is shifted by the inner potential, as described in the previous chapter.

The non–dispersive feature at a binding energy 6.74 eV, relative to Fermi level, is probably the so–called secondary cone–surface umklapp emission peak. Normally stationary peaks in normal emission valence band spectra are either from surface states or from this secondary cone–surface umklapp emission process.[Sorba et al., 1987] But from the blurred LEED spots, it is not likely that they originate from surface states. They are therefore most likely

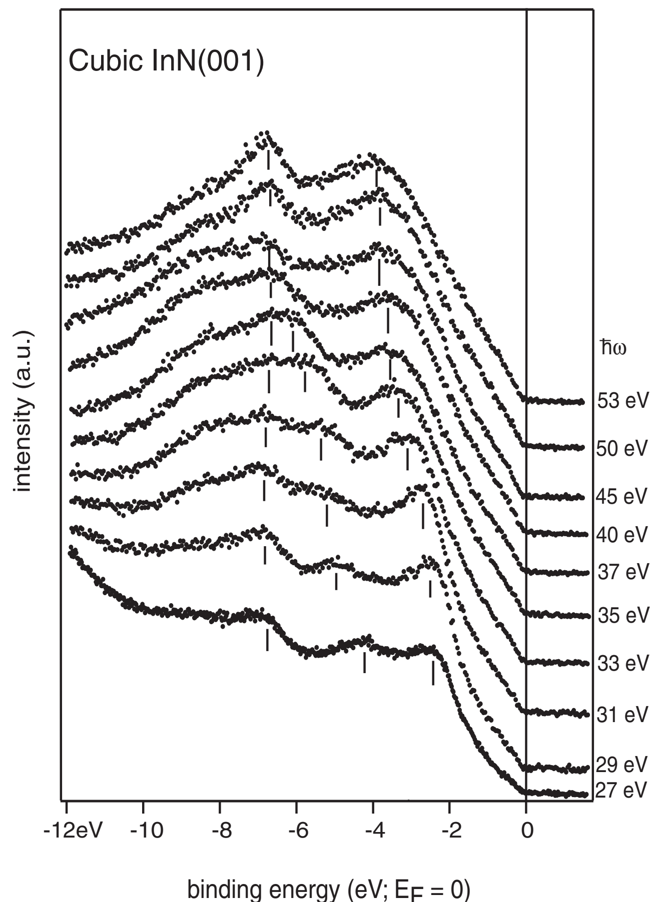

Figure 4.6: *Set of valence band spectra from c–InN(001), recorded in normal emission for photon energy from 27 eV to 53 eV. Peak positions used in band determinations are indicated by markers underneath each spectrum.*

due to emission from a point of high density of states in the occupied bands which occurs with a loss of electron momentum conservation, for example, through scattering from phonons.[Sorba et al., 1987] Such features are commonly observed in valence band spectra from III–V semiconductors.[Chiang et al., 1980; Dhesi et al., 1997; Sorba et al., 1987; Ding et al., 1996] The energy position of the non–dispersive peaks is in general determined by the one–dimensional valence band critical points[Chiang et al., 1980; Chiang and Eastman, 1980]; we therefore obtained the critical point binding energy at the X_3 point as 6.74 eV.[Ding et al., 1996]

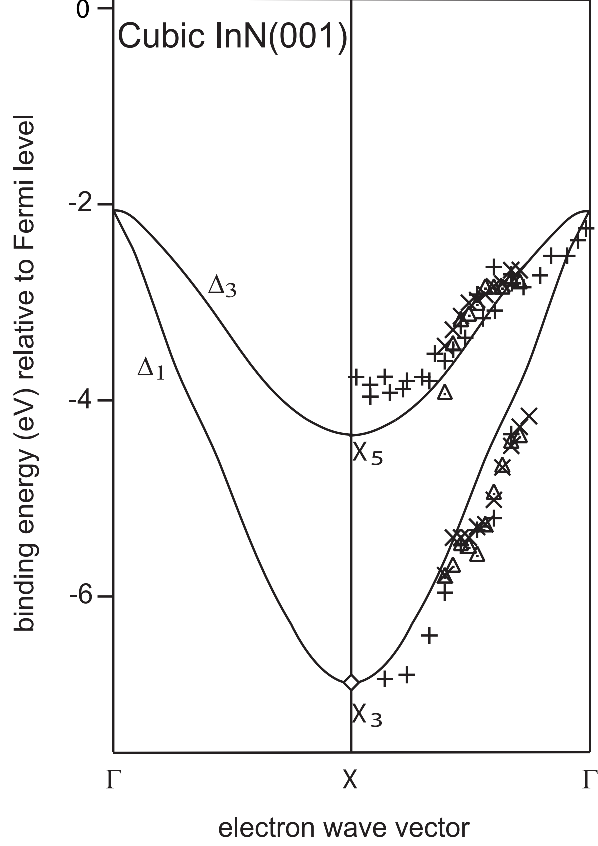

Figure 4.7: *Experimental band structure of c–InN along the* $\Gamma - \mathrm{X}$ *direction in the Brillioun zone. Single symmetry labels are used throughout. Solid lines are the calculated band structure. Data points are from this work.*

With the assumption of a free electron final band and based on the lattice constant of cubic InN of 4.97 Å[Lima et al., 1999], the Γ point is reached at $k_{\perp}$ value of 2.53 Å^{-1} and 5.06 Å^{-1}, while the X point is reached at 3.79 Å^{-1}. With an inner potential of 7 eV, the experimental band structure can now be evaluated from the energies of the dispersive peaks in the spectra in Fig. 4.6. This is shown in Fig. 4.7 for the Γ–X direction, compared with the calculated band structure by Fuchs et al[Fuchs et al.]. The calculated bands have been rigidly shifted to higher binding energy by 2.08 eV in order to coincide the experimental critical point at energy of 6.74 eV (diamond point in the figure) with the theoretical band at the X_3 point. Different symbols indicated

different data sets from separate measurements or folded from different parts of the Brillioun zone.

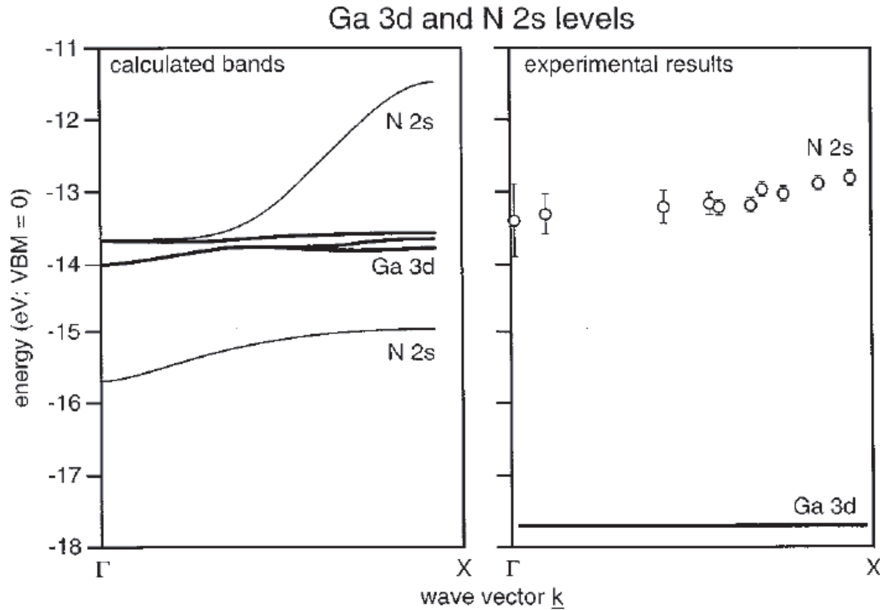

Figure 4.8: *Band structure along Γ–X line in the region of the Ga 3d/N 2s bands. Left panel is the calculation result from Fiorentini et al.[Fiorentini et al., 1993], right panel is the photoemission experimental results form Ding et al.[Ding et al., 1996].*

Because of the limitation of the monochromator, we could not reach the upper part of the Δ_1 band. Other than that, the general agreement is pretty well between different data sets and between the calculated bands. The deviation is somehow larger at the X_5 point (about E_B =0.49 eV energy difference) with a experimental value for the X_5 point of 4.03 eV. This inconsistency could be due to the lack of resolution of the top band within the leading peak near the VBM. But the overall width of the upper valence band range is similar to the calculations of Fuchs et al.[Fuchs et al.] and references [Stampfl and de Walle, 1999] and [Ramos et al., 2001].

The behaviour of the lower Ga *3d* and N *2s* states has received particular attention in cubic GaN, since the proximity of the N *2s* and Ga *3d* levels they were expected to strongly hybridize,[Fiorentini et al., 1993; Ding et al.,

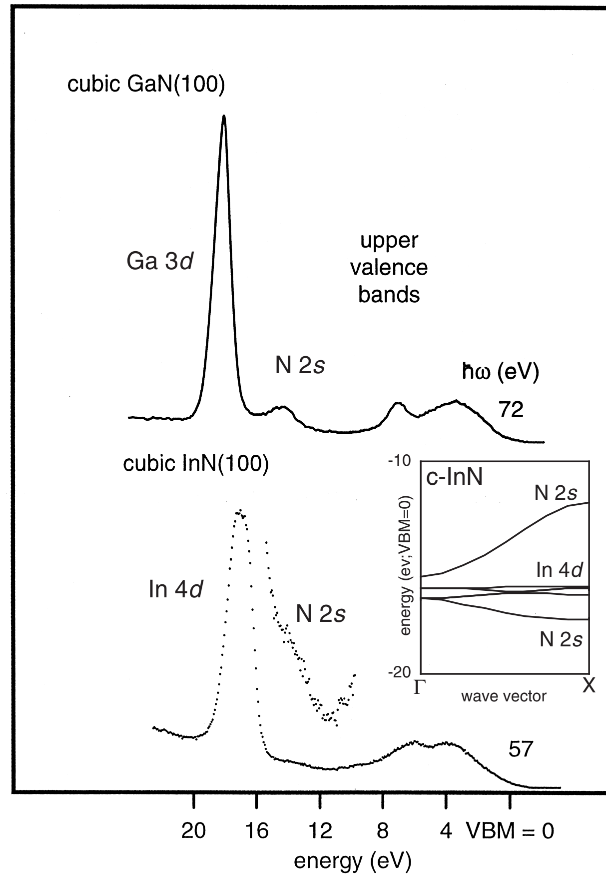

Figure 4.9: *The photoemission spectra of shallow core levels and valence band region from cubic GaN (upper spectrum) and cubic InN (lower spectrum). The N 2s level from c–InN is enlarged for better observation. The inset is the calculated[Fuchs et al.] c–InN bands for In 4*d*/N 2s along the* Γ*–X direction.*

1996] which has been studied intensively by Ding et al.[Ding et al., 1996] Fig. 4.8 shows the calculated hybridization of the Ga *3d* and N *2s* levels along the Γ–X direction (left panel)[Fiorentini et al., 1993] and the photoemission experimental results (right panel)[Ding et al., 1996]. The In *4d* level is shallower than that of Ga *3d* and deeper than that of N *2s*; since the In *4d* is even closer to N *2s*, one would expect to observe the similar hybridization behaviour as in cubic GaN.

The theoretical calculation[Fuchs et al.] for the In *4d*/N *2s* bands along the Γ–X direction is in the inset of Fig. 4.9. However, as shown in the same figure, the Ga *3d* and N *2s* levels for cubic GaN are well separated, for the cubic InN, the In *4d* peak is rather broad and featureless, the N *2s* is just buried under this broad In *4d* peak, enlarged in the lower spectrum. It is not possible to locate the energy positions precisely enough to obtain a meaningful experimental result under these circumstances. A better sample quality or a better sample preparation procedure for the optimization of the sample stoichiometry is needed in order to observe the dispersion of the In *4d*/N *2s* bands.

In summary, we used mild ion bombardment and subsequent annealing of the sample under an ammonia atmosphere to clean the cubic indium nitride sample. The ion bombardment removed the surface contaminations but also caused nitrogen depletion and formed metallic In clusters on the surface. Free nitrogen atoms from ammonia reacted with surface indium and restored the semiconductor–like surface. This surface showed a blurred (1 × 1) LEED pattern. We applied angle–resolved photoemission on this surface to determine the occupied band structure along the Γ–X symmetric line, which showed good agreement with a calculated band structure. However, we could neither locate the critical point energy at X_5 point precisely nor resolve the In *4d*/N *2s* dispersion. All of these shows that we need better sample preparation method to restore the optimized surface stoichiometry.

4.2 Wurtzite Gallium Nitride

The physical properties of gallium nitride (GaN) make it an attractive semiconductor for many electronic and optoelectronic devices. Its wide, direct energy band gap makes it suitable for short wavelength light emitters (LEDs, LDs) and detectors. The wide energy band gap and good thermal stability of GaN is also advantageous for high–temperature and high power electronics. A fundamental understanding of the electronic structure of this material is required if they are to fulfill their technological potential. To this end, understanding the electronic properties of this material under well controlled condition is of particular importance since it is the first step in understanding fundamental issues such as contact formation, chemical reactivity, growth processes, and structural stability. Despite numerous studies that monitor the epitaxial process and characterize the resulting morphology of the thin films, the growth front is not yet completely understood. Studies

concluded that the surface stoichiometry depends on details of the growth parameters such as the substrate temperature, buffer layers and gallium and nitrogen flux.[Hacke et al., 1996] Other studies revealed that the Ga to N ratio is an important parameter for different surface reconstructions.[Smith et al., 1997] It is well known that it is difficult to obtain atomically–clean, well–order and stoichiometric GaN surface by post sample treatment methods. It also has been shown that the surface cleaning processes for wurtzite GaN thin films will strongly affect the electronic properties of the films, such as the valence band shapes and Fermi level positions.[Bermudez et al., 1998] Therefore, it is reasonable to grow the GaN thin films under a well controlled environment, e.g. inside an ultra high vacuum (UHV) chamber, and to *in–situ* characterize and study the properties of the as–grown thin films.

The growth technique was based on the MBE method but with two different atomic nitrogen sources. One involved cracking the nitrogen molecules by a radio frequency plasma source to produce nitrogen atoms, another was to inject NH_3 gas and direct crack the molecules on the hot crystal surface to release free nitrogen atoms. We have grown single crystal GaN thin films on 6H–SiC(0001) surface successfully with these two nitrogen atom sources. The studies and comparison of the resulting GaN thin films will be the main topic of the following subsections.

4.2.1 The Growth of w–GaN

Sapphire (Al_2O_3), single crystal aluminum oxide, was the original substrate used in Maruska and Tietjen's pioneering study of GaN epitaxy by hydride vapour phase epitaxy (HVPE) in 1969.[Maruska and Tietjen, 1969] It still remains as the most common choice substrate for GaN–based devices. Most surprisingly, its properties are seemingly unsuitable based on the usual assumptions made in choosing a substrate for epitaxy; it has large lattice constant and thermal expansion coefficient mismatches with GaN.[Ortony and Foxonz, 1998] This causes the dislocation density of commercial available GaN–based LEDs to be as high as 2–10$\times10^{-10}$cm^{-2}, which is four order of magnitude higher than that of working LEDs made from any other III–V material systems.[Lester et al., 1995] The large thermal expansion coefficient difference will produce biaxial compressive stress in the layer as it cools from the deposition temperature. For thick films, the stress can cause both the film and the substrate to crack.[Etzkorn and Clarke, 2001] In addition, there is evidence that oxygen from the sapphire causes unintentional doping in the GaN layer, raising its background electron concentration.[Nostrand

Substrate	Space Group Symmetry	Lattice Constants (Å)	Thermal Expansion Coefficient ($10^{-6}K^{-1}$)
		$a_0 = 3.189$	5.59
αGaN	$P6_3mc$		
		$c_0 = 5.185$	3.17
βGaN	$F\overline{4}3m$	$a_0 = 4.52$	?
		$a_0 = 4.7589$	7.3
Al_2O_3	$R\overline{3}c$		
		$c_0 = 12.991$	8.5
		$a_0 = 3.0806$	4.46
6H–SiC	$P6_3mc$		
		$c_0 = 15.1173$	4.16
3C–SiC	$F\overline{4}3m$	$a_0 = 4.3596$	3.9
Si	$Fd\overline{3}m$	$a_0 = 5.430$	3.59
GaAs	$F\overline{4}3m$	$a_0 = 5.652$	6.0
MgO	$Fm\overline{3}m$	$a_0 = 4.216$	10.5
$MgAl_2O_4$	$Fd\overline{3}m$	$a_0 = 8.083$	7.45
		$a_0 = 5.431$	11.9
$NdGaO_3$	Orthorhombic	$b_0 = 5.499$	6.6
		$c_0 = 7.710$	5.8
		$a_0 = 5.169$	15
γ–$LiAlO_2$	$P4_12_12$		
		$c_0 = 6.268$	7.1
		$a_0 = 5.4063$	6
$LiGaO_2$	$Pna2_1$	$b_0 = 6.3786$	9
		$c_0 = 5.0129$	7
		$a_0 = 3.252$	2.9
ZnO	$P6_3mc$		
		$c_0 = 5.213$	4.75

Table 4.1: *Space group symmetry, lattice constants and thermal expansion coefficients for substrate materials which are used for the growth of epitaxial GaN films. After ref. [Ambacher, 1998].*

et al., 2000] Other than all of those reasons, sapphire is electrically insulating, which makes it difficult to heat up in our direct current heating system. All in all, we needed a substrate other than sapphire for the self–grown GaN films.

There are many other choices for GaN epitaxy substrate materials, as shown in table 4.1[Ambacher, 1998]. Apart from sapphire, silicon carbide (both the 4H– and 6H–polytype) is the most common choice as the substrate material for w–GaN epitaxial growth. It holds several advantages over sapphire, such as a smaller lattice constant mismatch (3.1%) for [0001] oriented films, a much higher thermal conductivity, smaller thermal expansion coefficient misfit, and, being a semiconductor, it is ideal for the direct current heating method and for photoemission experiments. However, SiC does have its disadvantages. One is due to the poor wetting of Ga on the silicon carbide surface, which is because of the lower surface energy of the 6H–SiC(0001) surface.[Lahrèche et al., 2000] As a consequence, 3D randomly oriented independent GaN islands tend to form upon the onset of nucleation, eventually leading to textured or polycrystalline growth. In addition, there are several possible bonding configurations at the GaN–SiC interface,[Ren and Dow, 1997] the growth conditions must hence promote the exclusion of formation of N–Si bonds at the interface. This can be achieved by nitridation of the 6H–SiC(0001) surface thoroughly prior to nitride growth.[Ploog et al., 1998] We therefore chose the 6H–SiC as the substrate material for our self–grown epitaxial GaN films.

From table 4.1, one can see that hexagonal polytypes of SiC belong to the same space group $P6_3mc$ as wurtzite GaN. The GaN deposit on hexagonal SiC substrate results in a simple epitaxial relationship, that is $[0001]_{\mathrm{GaN}} \parallel [0001]_{\mathrm{SiC}}$, $[11\bar{2}0]_{\mathrm{GaN}} \parallel [11\bar{2}0]_{\mathrm{SiC}}$.[Ploog et al., 1998] The most studied substrates for GaN epitaxy are the 3C–SiC/Si(100) and 6H–SiC, as these polytypes have been the most readily prepared or commercially available for the longest time. With 4H–SiC now commercially available, its use as substrate for GaN epitaxy will become more common.

The first step for a good epitaxy is the cleanliness and good order of the substrate surface. The substrates for the studies were n–type Si–surface 6H–SiC(0001) wafers from Cree Research Inc. with research grade quality.

The composition and the structure of SiC surface depends heavily on the preparation procedures employed on the surface in the UHV environment.[Starke et al., 1995] Cleaning the surface by ion bombardment and

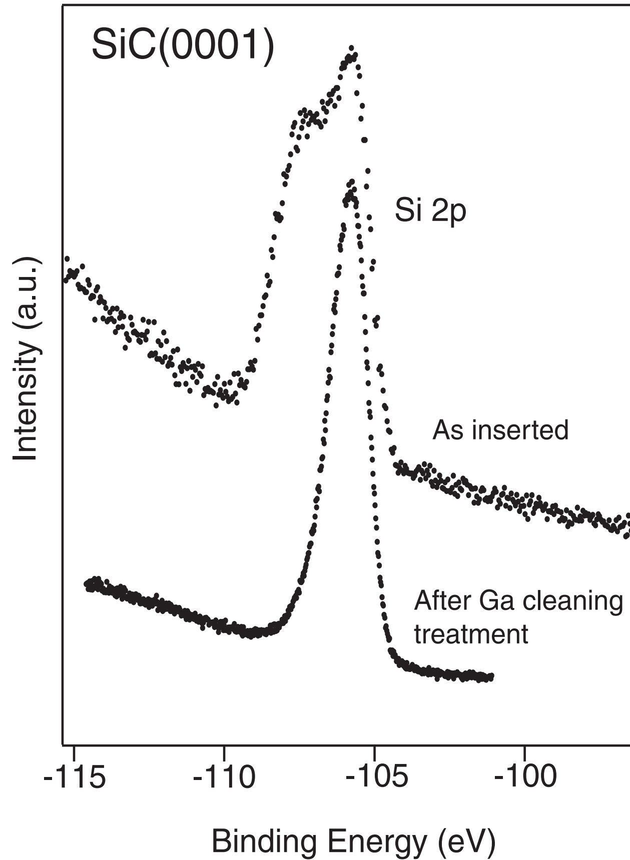

Figure 4.10: *The cleaning process for the SiC sample. The upper spectrum was from the as–inserted 6H–SiC(0001) surface, an oxidize component exist in higher binding energy side. After annealing the sample under Ga vapour for 15 min. at 1220 K, the oxidized component was removed; as shown in the lower spectrum.*

subsequent annealing results in severe surface damage.[Kaplan, 1984] Some studies have shown that high temperature annealing above 1100 K is necessary to remove oxygen contaminations.[Bommel et al., 1975; Dayan, 1986; Starke et al., 1995] However, from this temperature upward, one can also observe graphitic carbon on the surface.,[Starke et al., 1995] while annealing above 1300 K will reduce the Si/C ratio at the surface due to the loss of Si.[Bellina Jr. et al., 1986] UHV annealing, thus seem does not a good preparation method to obtain a clean and well ordered stoichiometric 6H–

SiC(0001) surface.

Two alternative preparation methods were used by Kaplan et al.[Kaplan and Parrill, 1986; Kaplan, 1989] They annealed silicon carbide samples under Si or Ga vapor; this will remove surface oxygen as volatilized SiO and Ga_2O. Annealing under Si flux requires lower sample temperature to achieve a clean surface, which is 1120 K only[Kaplan, 1989] and for the Ga flux method one will need 1250 K.[Kaplan and Parrill, 1986] But Ga vapour is more suitable for us since we have Ga MBE cell built into our UHV chamber for GaN growth already.

Figure 4.10 shows the effect of the sample preparation method. We annealed the as–inserted SiC sample at 1220 K under Ga vapour for 15 minutes. The upper spectrum is the Si 2*p* peak from the as–inserted SiC sample, an oxidized component is clearly visible in the higher binding energy side. After the treatment, this component was completely removed (lower spectrum).

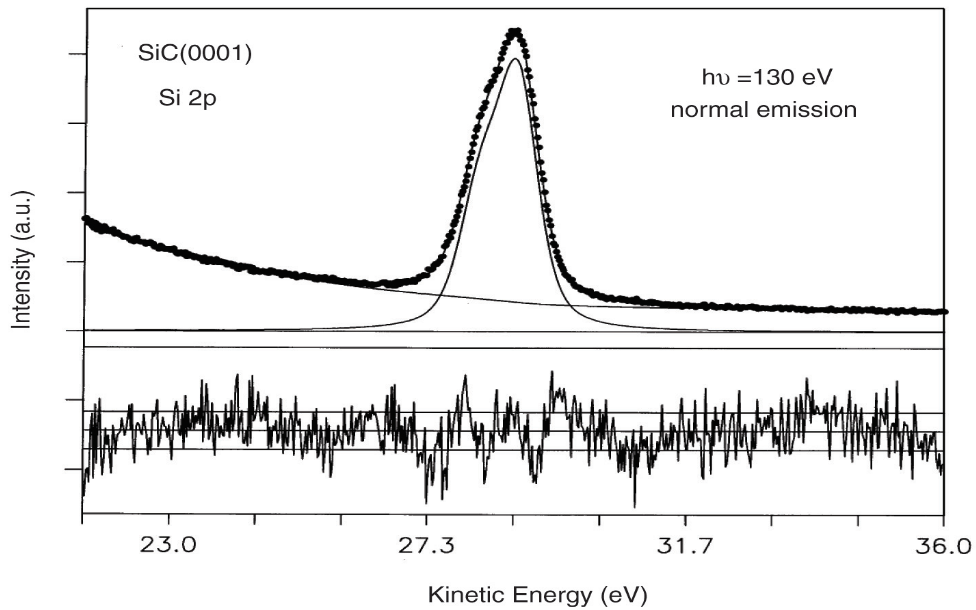

Figure 4.11: *Core level spectrum of the Si 2p peak from clean SiC(0001) along with line shape analysis. The spectrum was recorded in normal emission condition with 130 eV photon energy. Dots are the data points, solid lines are the fitting result and background. Below the spectrum is the residuum of the fit. See text for the detail description of the analysis.*

We have applied data deconvolution processes to these two spectra; the

deconvolution procedures will be described in detail in next chapter. The spin–orbit branching ratio and energy splitting for Si $2p$ level are 0.53±0.03 and 627±10 meV, respectively. The result of curve fitting for the Si $2p$ line from clean SiC is shown in Fig. 4.11 along with the residuum of the data fit. The energy separation of oxidized component and bulk component from dirty SiC is 1.68 eV, which is consistent with van Elsbergen et al..[van Elsbergen et al., 1996] They determined the energy shift of oxidized component relative to bulk SiC Si $2p$ emission to be 1.7 eV. Fig. 4.11 shows the result of the curve fitting of the lower spectrum in Fig. 4.10. The fitting result shows one component only, which is the bulk emission from the 6H–SiC substrate. The absence of oxidized and surface components indicate that the 6H–SiC(0001) sample is clean but lacks of surface order. Typically, the as–received commercial SiC wafers have scratches and subsurface crystal damages from the mechanical polishing procedures,[Xue et al., 1999] these defects can only be removed by a more sophisticated preparation method, i.e. *ex situ* H_2 etching at 1600°C subsequently *in situ* Ga or Si deposition and flash–off.[Ploog et al., 2000; Xue et al., 1999] However, this method is too complex for our purpose, we therefore tried to grow w–GaN on the clean 6H–SiC(0001) surface prepared as shown in the lower spectrum in Fig. 4.10.

As described in previous paragraphs, in order to achieve two–dimensional nucleation of single crystal GaN, one has to improve the wetting between the 6H–SiC(0001) surface and GaN. This can be done by nitridation of the SiC surface at a sufficiently high temperature, (of 850°C) prior to GaN growth and subsequent nucleation of GaN at a lower substrate temperature of 650°C.[Ploog et al., 1998]

Since we used two different gases as atomic nitrogen sources, we performed SiC surface nitridation in two ways. The exposure of the bare SiC surfaces under 350 W forward power of nitrogen plasma was one, the other was to anneal SiC under ammonia atmosphere; both substrates were kept at 850°C for 30 minutes. The nitrogen and ammonia pressure were both 1×10^{-4} mbar. After the nitridation process, we decreased the substrate temperature to 650°C but kept the other parameters constant, then switched on the gallium molecular beam, to start the GaN nucleation process.

In general, higher substrate temperatures are expected to improve structural perfection and increase the growth rate of the GaN films, but a lower substrate temperature is required to promote the wetting process, and at substrate temperature above 850°C no growth of GaN occurs, probably due to the strongly increased desorption rate of the Ga and N species at ele-

vated temperature from the foreign substrate.[Ploog et al., 1998] Furthermore, higher nucleation rates resulted inevitably in poor crystalline GaN nuclei. This is assumed to be associated with the reduced migration lengths of the reactive species, in particular Ga, at the relatively low substrate temperature,[Brandt et al., 1997; Yang et al., 1996] as longer times are needed for the species to arrive at their ideal lattice sites, a higher nucleation rate would induce disorder, defects, and possibly excess strain in the GaN films.

We have tried different substrate temperatures for GaN thin film growth, 650°C is the optimized substrate temperature under our growth condition, the overlayer quality was judged by LEED and valence band spectra. All the self–grown GaN thin films described in this thesis were grown under the same conditions. The gallium Knudsen cell was kept roughly at 700°C, that is corresponding to a vapour pressure of 1.5×10^{-6} mbar, a bit higher than 5.2×10^{-7} mbar, the Ga vapour pressure suggested by Mayer et al.[Mayer et al., 1997] for MBE–grown GaN.

Figure 4.12 shows a comparison of spectra from clean SiC and the as–grown GaN thin films. As indicated in the figure, the lower spectrum is from a clean 6H–SiC(0001) surface excited by 130 eV photons. The center one is from GaN thin film grown by ammonia using the surface cracking MBE method, also with a photon energy of 130 eV. The uppermost spectrum is from nitrogen assisted MBE method GaN ($\hbar\omega = 150$ eV). All of the spectra were recorded under normal emission. The growth of the GaN thin films was stopped when the Si $2p$ signal from the substrate had disappeared, the estimated GaN thin film thickness was more than 50Å. As expected, except the secondary background, the GaN spectra are similar to each other despite the different gas sources.

The LEED pattern of the as–grown GaN thin films shows a clear (1×1) structure, as illustrated in Fig. 4.13. This is somehow in contrast to Ploog et al., since their hexagonal GaN-on-SiC(0001) thin films only stabilized under (2×2) reconstruction, studied by reflection high–energy electron diffraction (RHEED) during thin film deposition.[Ploog et al., 1998]

From our studies, thin GaN films grown with different gas sources possess the same structure, but one can clearly see that ammonia gas induces better films because that LEED pattern is sharper than for the N_2 plasma sample.

According to scanning tunnelling microscope (STM) studies and first–principles total energy calculations,[Smith et al., 1997, 1998, 1999] depending

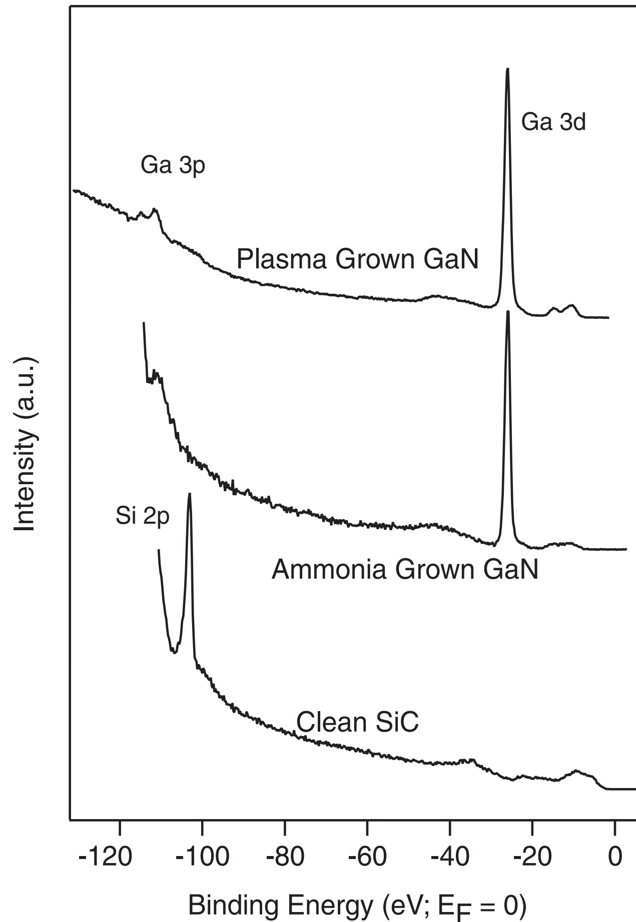

Figure 4.12: *The comparison of the clean SiC and the GaN overlayers grown by different atomic nitrogen sources. From upper to lower spectrum, GaN grown with nitrogen plasma, ammonia, and clean 6H–SiC(0001). The Si 2p signal from substrate was totally disappeared in the upper two spectra.*

on the Ga to N ratio, hexagonal GaN surfaces are full of reconstruction structures. Based on the first–principles calculations, the (2×2) reconstruction is the most stable structure in the Ga–rich limit for the GaN(0001) surface, i.e. the Ga face of the GaN surface.[Smith et al., 1998, 2114] The (1×1) structure, on the other hand, is the most energetically favoured structure for the GaN($000\bar{1}$), the N face, of the GaN surface.[Smith et al., 1997, 2114] The model for this surface structure is schematically illustrated in Fig. 4.14,[Smith et al., 1998] which consists of a full monolayer of Ga atoms bonded to a N–terminated GaN bilayer.[Smith et al., 1997] One may thus conclude that the

thin GaN films grown by ourselves expose the GaN(000$\bar{1}$) surface, different from Ploog's GaN(0001) surface, even though we have similar recipes for GaN growth.

Another point is worth to be mentioned here. According to Dhesi et al.,[Dhesi et al., 1997] the GaN surface is sensitive to residual gas contamination, for they had to sputter and anneal the sample every two hours to keep the surface clean. However, I did not observe this behaviour during the experimental period. After the GaN thin films were left inside UHV chamber

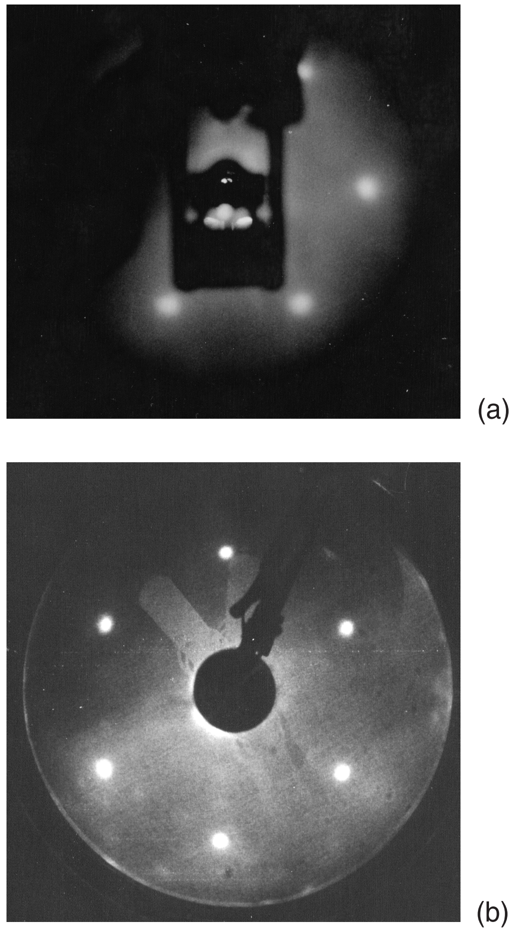

Figure 4.13: *The* (1×1) *LEED pattern taken from as–grown hexagonal GaN thin films. (a)from the thin film grown by* N_2 *plasma assisted MBE method (primary beam energy* (E_p) *75 eV). (b)from the ammonia MBE thin film,* $E_p = 78$ *eV. These two photos were taken from different LEED optics.*

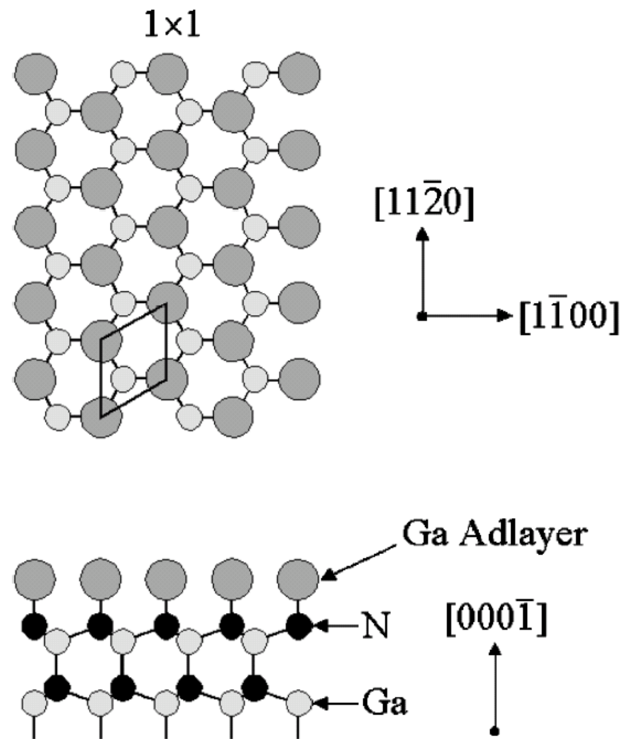

Figure 4.14: *Schematic view of (1 × 1) Ga adlayer structure of GaN surface. After Ref. [Smith et al., 1998].*

for one night, the valence band spectrum and the LEED pattern still showed the same features.

A possible explanation is that maybe the samples have different surface polarities, just as the aqueous solution of KOH or NaOH will selectively attack GaN surfaces of one polarity, whereas surfaces of the opposite polarity remain completely unaffected;[Seelmann-Eggebert et al., 1997] so one polarity may be sensitive to gas contamination while the other one is not. Yet no solid evidence to support this speculation exists at present.

4.2.2 The electronic structure of w–GaN

As for cubic indium nitride, ARPES experiments were applied to determine the electronic band structure of wurtzite GaN under normal emis-

sion geometry, the UV light was incident at 45° relative to surface normal. For (0001) surface of hexagonal structural crystal, normal emission ARPES probes states with momenta along $\Gamma - \Delta - A$ symmetric line in reciprocal space, see Fig. 3.3.

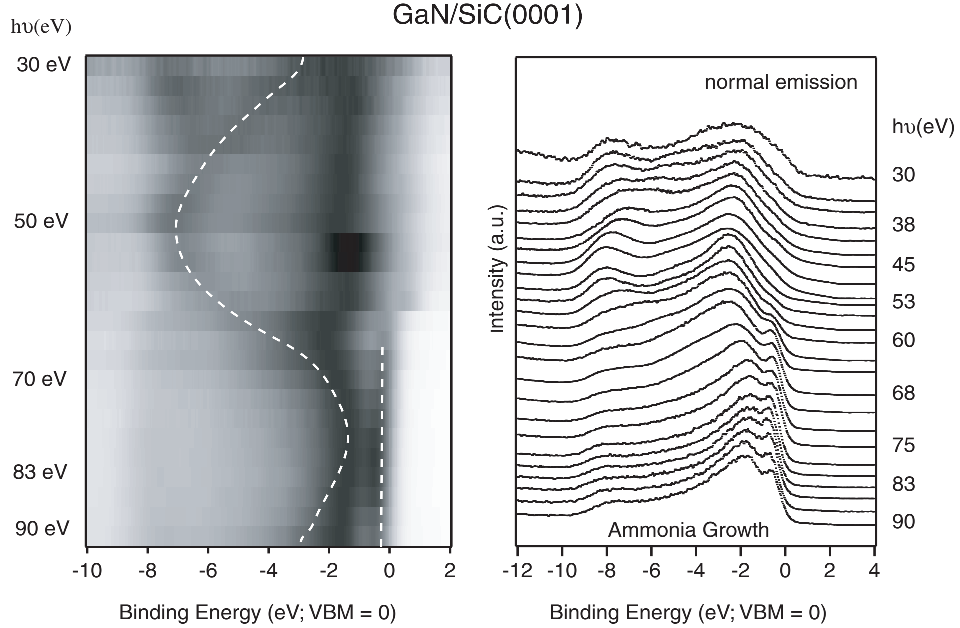

Figure 4.15: *Set of normal emission valence band spectra from w–GaN(0001) surface, photon energies were varied from 30 eV to 90 eV. Lines are only guides to the eye. The sample was prepared by the ammonia gas as nitrogen source. Left is the grey scale image of the right hand spectra. Compare with Fig. 4.16, the dispersion can be easily followed.*

The normal emission spectra of the w–GaN samples are shown in Fig. 4.15 and Fig. 4.16 for the ammonia and N_2 plasma samples, respectively. The photon energies were varied from 20 eV to 90 eV, as indicated beside each spectrum. These spectra were normalized to the same height and aligned at the VBM of each spectrum. The left hand side of the figures are the same spectra but converted into grey scale for better visual effect of the band dispersion. Darker means higher intensity.

From these two figures one can clearly see that for the ammonia growth sample, the valence band features are more pronounced and the dispersion of peaks in this region is clearer and easier to follow. The implies that the

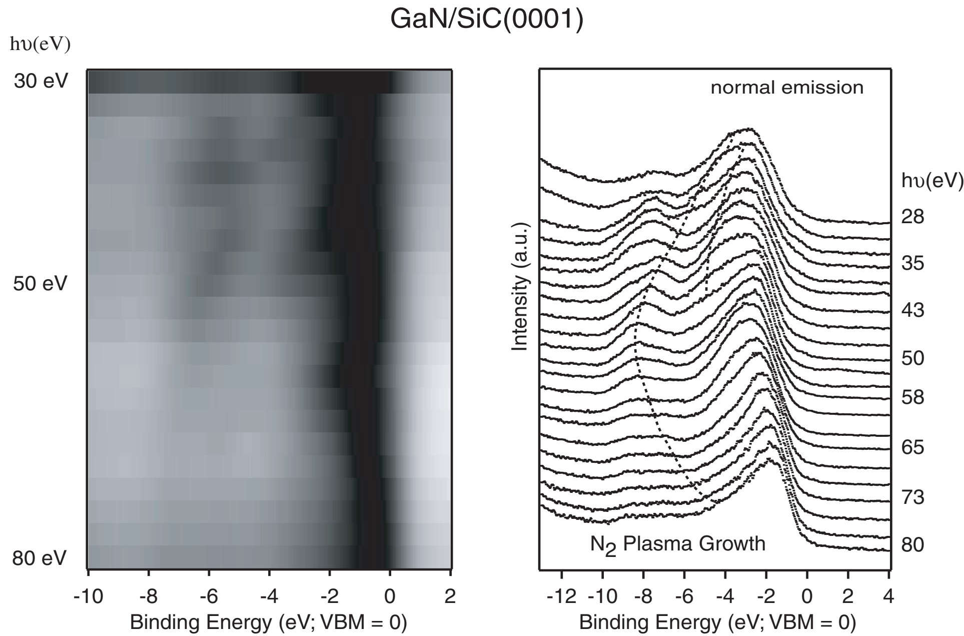

Figure 4.16: *Series of spectra similar to previous figure but N_2 plasma as the gas source. Photon energy changed from 28 eV to 80 eV. Lines are only as guides to the eye. The dispersion is not as obvious to follow.*

ammonia growth samples have a better crystalline quality than the nitrogen plasma growth ones, in agreement with the result of the LEED studies.

One of the reasons why ammonia gas can produce a better GaN thin film quality is due to the reactive hydrogen atoms released from the NH_3 molecules; these are effective in etching the surface contaminations away, [Mayer et al., 1997] and have a similar effect as the high temperature H_2 etching applied on 6H–SiC(0001) surface to remove surface scratches.[Ploog et al., 2000] Therefore the ammonia method can produces better substrate surface to grow GaN overlayer.

Let us now return to the normal emission valence band spectra. All features except the component near a binding energy of 8 eV below VBM and the sharp peak near VBM (see Fig. 4.15) exhibit dispersion with photon energy, this is a clear sign of band–like behaviour of the initial states.[Chiang et al., 1980] Another clear sign of the direct i.e., **k**–conserving transitions, is the expanding and narrowing of the entire spectrum, suggesting that transitions at critical points are reached in those widest and narrowest places.[Himpsel,

1980]

Based on the lattice constant of hexagonal GaN; $a_0 = 3.189$Å, $c_0 = 5.185$Å, [Jain et al., 2000] the Γ point will be reached at a $k_\perp$ value of 3.64Å^{-1} and the A point at 3.03Å^{-1} and 4.24Å^{-1}. In comparison of the binding energies of these features with band structure calculations,[van Schilfgaarde et al., 1997; Rubio et al., 1993; Christensen and Gorczyca, 1994; Min et al., 1992] the emission from the Γ point occurs at photon energy roughly equal to 51 eV, where the high binding energy component reaches its maximum as expected. Two dominant features of the $\hbar\omega = 51$ eV spectrum located at binding energies 2.0 eV and 8.0 eV are assigned to the emission from the Γ_5^ν and Γ_3^ν critical points, respectively. The symmetric notations are after Ref. [Rubio et al., 1993].

In order to derive an experimental band structure, one needs to determine peak positions that correspond to the initial–state energies. For clearly separated peaks of a reasonable shape, this is straightforward. But there are cases where only a shoulder can be distinguished, like the spectra of the plasma sample. In the absence of a suitable model function for the peak shape of valence transitions, I use clearly distinguishable peaks or shoulders and also take into account situations where peaks become broader with photon energy. With the free–electron–final–band assumption, these peaks are translated into points in an E(**k**) diagram as described in previous chapter and using an inner potential of 10 eV, this is consistent with the value reported previously.[Dhesi et al., 1997]

This band diagram, in the range from the Γ to the A point along the line Δ of the bulk Brillouin zone, is shown in Fig. 4.17. The circles and squares are from the ammonia and nitrogen plasma samples, as indicated in the diagram. Also shown is a calculated band structure for the valence bands, based on the local density approximation band structure calculation of Rubio et al..[Rubio et al., 1993] The calculated bands have been rigidly shifted to higher binding energy by 1.6 eV, to fit the calculated VBM with the experimental leading peaks. The bands expected from the general shape of the band structure are clearly seen in the experimental data, and they closely follow the dispersions predicted by the calculations. Since we have two independent sets of data from thin GaN films grown with different gas sources, they should exhibit the same bulk electronic properties, a fact that puts the determination of the inner potential, and the shape of the bands, on a solid foundation.

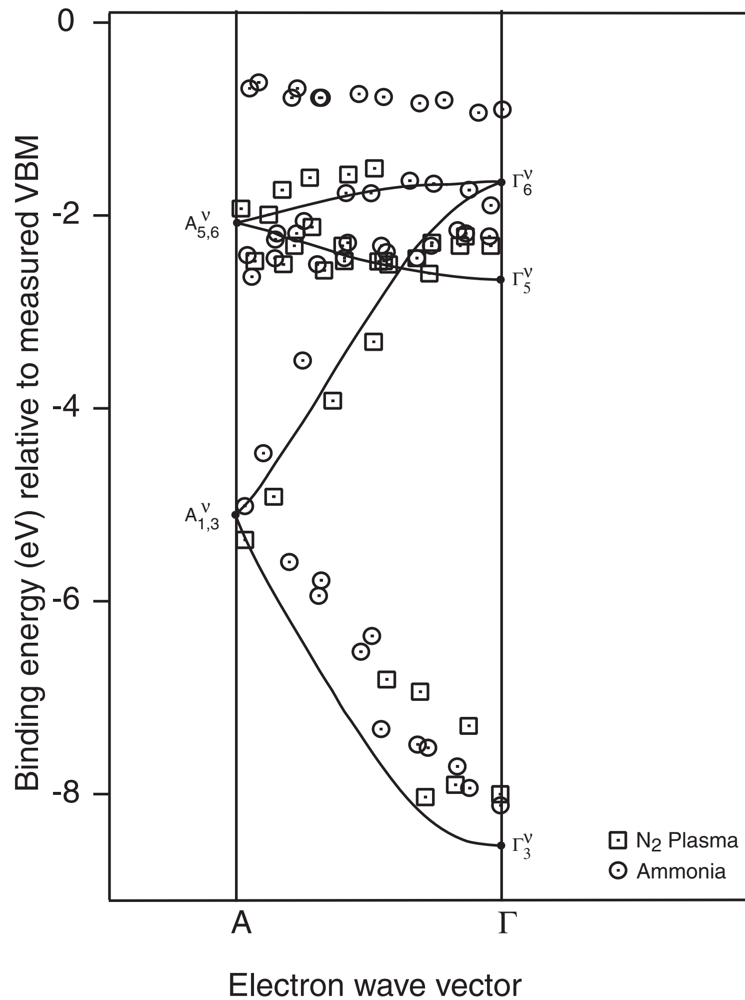

Figure 4.17: *Comparison of measured band structure for GaN thin films that were grown with two different nitrogen sources, and the theoretical calculation (solid lines, from Ref. [Rubio et al., 1993]) of the bulk GaN bands along the* $\Gamma - \Delta - A$ *direction.*

The energies of critical points and their comparison with calculations are the most important results of the experimental band structure determination. Just as the case of cubic indium nitride, the hybridization of Ga $3d$ and N $2s$ levels will occur, which is due to the close proximity of these two levels. They then have to be considered on an equal footing with the other valence electrons.[Fiorentini et al., 1993] One therefore has to distinguish between those calculations which treat the Ga $3d$ electrons as inert core electrons and

Table 4.2: *Critical points in the hexagonal GaN band structure from different calculations, compared with results from angle–resolved photoemission (this work), unit in eV.*

	Exp.	LDA^a	GW^a	LDA^b	$FP-LMTO^b$
Γ_3^ν	-8.10	-9	-9.6	-8.6	-8.7
Γ_5^ν	-2.30	-2.7	-2.8	-2.6	-2.6
Γ_6^ν	-1.60	-1.6	-1.6	-1.6	-1.6
$A_{5,6}^\nu$	-2.24	-2.1	-2.1	-2.1	-2.1
$A_{1,3}^\nu$	-5.10	-5.7	-6.2	-5.4	-5.4

LDA: Local density approximation.
FP–LMTO: Full potential linear–muffin–tin–orbital calculation.
[a]Ref. [Rubio et al., 1993]
[b]Ref. [van Schilfgaarde et al., 1997]

those which explicitly include them. We hence restrict the comparison with the calculations to those that include the Ga $3d$ levels as part of the valence electrons,[van Schilfgaarde et al., 1997; Rubio et al., 1993] and list the values in Table 4.2. All of the theoretical critical point energies are shifted by 1.6 eV to higher binding energy to fit the calculated and experimental VBM (the Γ_6^ν point). The general agreement between the different calculations and also between the calculations and experiment is adequate.

One of the most striking aspects of Fig. 4.17 is that a stationary feature exist in the energy gap region; it is also clearly visible in Fig. 4.15, and only exist in the ammonia grown sample. The existence of this state is not predicted by published bulk band structure calculations and was also observed by Dhesi et al..[Dhesi et al., 1997] Dhesi et al. assigned this component as a surface state because of the following reasons. First of all, this state only observed from clean, well–ordered surfaces. Secondly, it is highly sensitive to H_2 as well as O_2 adsorption and N_2^+ bombardment. And thirdly, it does not disperse with photon energies and thus has no component of momentum perpendicular to the surface. These prove conclusively that this state is indeed a surface state.[Dhesi et al., 1997] Since this state only exists in the ammonia grown GaN thin film, it is another evidence that the ammonia gas is superior to the nitrogen plasma source for the GaN thin films grown by MBE method.

The surface state dispersion was recorded by changing the polar angle

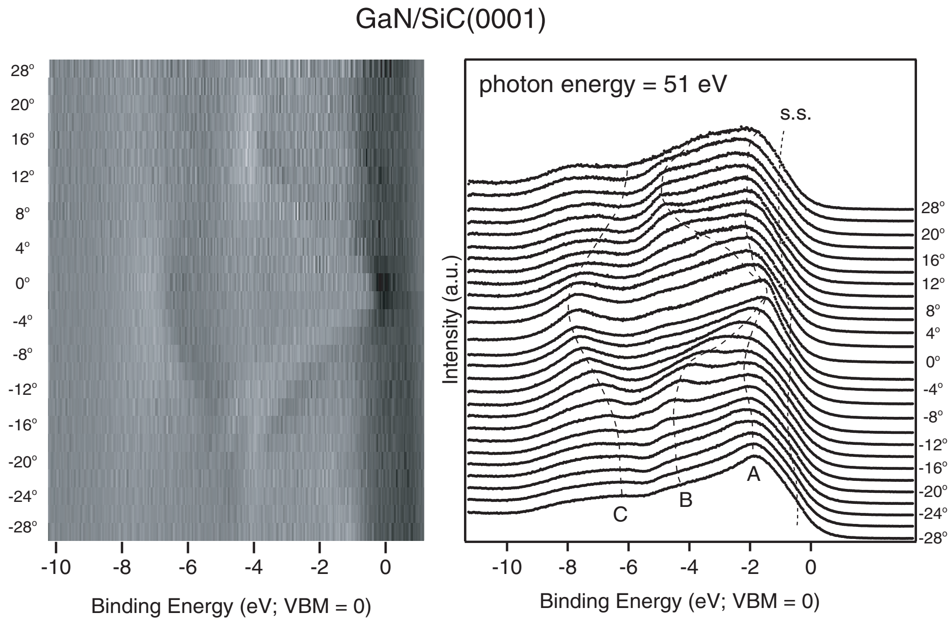

Figure 4.18: *Off–normal ARPES spectra recorded from the ammonia grown GaN(0001)1×1 surface with a photon energy of 51 eV. Showing emission from states along the* $\overline{\Gamma}$–$\overline{M}$ *direction. Left panel is the derivative of the spectra displays in grey scale. The photoelectron collecting angles are indicated beside the spectra. Lines are only as guides to the eye.*

along the surface Brillouin zone $\overline{\Gamma}$–$\overline{M}$ direction, the orientation being aligned according to the LEED pattern prior to the measurements. The photoelectrons were excited by 51 eV photons, incident in 45° to surface normal. The angle of the spectrometer was changed from 0° to 28° in both direction in every two degrees, as indicated in Fig. 4.18, the positive and negative degrees were chosen arbitrarily. The left panel of Fig. 4.18 is the derivative of the spectra show in the right panel, is displayed in grey scale for better visual effect to follow the dispersion of the bands.

Three highly dispersive bands are clearly visible in the spectra; labelled as A, B, and C in the figure, their dispersions are symmetric to the 0° azimuth angle, which is as expected, since this is the $\overline{\Gamma}$ point in the Brillouin zone, and these are three bulk bands. Another state near the VBM, labelled as S.S., does not disperse much with the changing of spectrometer angle, this state is the surface feature described previously, it also exhibits a symmetric behaviour relative to zone center. With a free electron final state assumption,

one can use the data of Fig. 4.18 to generate a surface band dispersion as shown in Fig. 4.19. Inverse photoemission experiments have shown that the free electron final state is a good approximation for photon energies above 25 eV.[Valla et al., 1999]

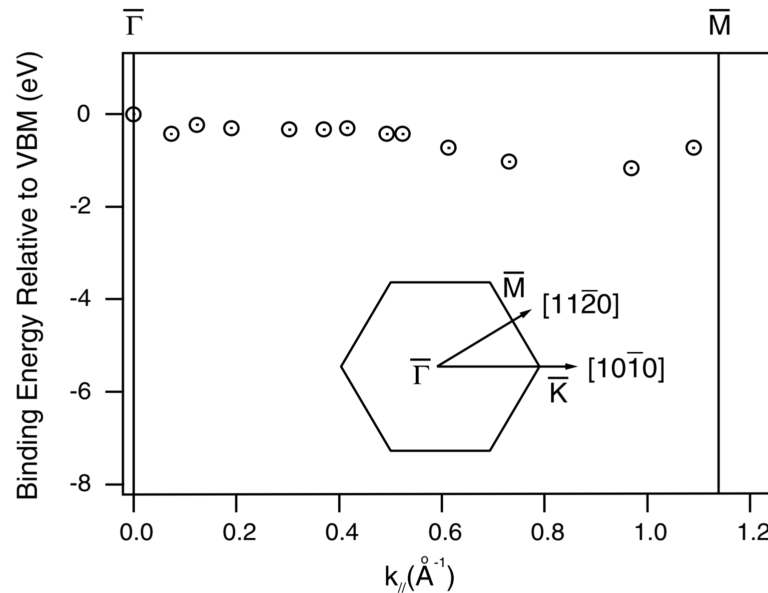

Figure 4.19: *Measured two–dimensional band structure for the clean ammonia grown GaN(0001)1×1 surface in the 1×1 surface Brillouin zone along the* $\overline{\Gamma}$–$\overline{M}$ *direction. The recording geometry is indicated in the inset.*

The exact origin of this surface state is difficult to determine due to uncertainties in the structure, termination, and stoichiometry of the surface. However, the characteristics of this surface band give some important clues. The most notable aspect of this state is the fact that it is highly sensitive to surface contamination,[Dhesi et al., 1997] it also shows very little dispersion in the $\overline{\Gamma}$ to $\overline{M}$ region. This indicates that this state is quite localized, probably corresponding to the dangling–bond surface state,[Chao et al., 1999] since similar behaviour for dangling–bond states is also observed in other systems, for example, the SiC(001) surface,[Duda et al., 1999] or the Si(001)2×3–In surface.[Yeom et al., 1997] The reactivity of this state[Dhesi et al., 1997] is consistent with this assignment. However, in order to totally reveal the origin of this state, one will need further studies and compare the results with

the theoretical calculations, which are not available for the moment.

4.3 Wurtzite Aluminum Nitride

Aluminum nitride, AlN, has the largest energy band gap (6.2 eV[Mohammad et al., 1995]) amongst the group III-nitride semiconductors. Just as other two family members, it usually crystallizes in the hexagonal wurtzite structure,[Ching and Harmon, 1986] although some reports[Paisley and Davis, 1993] suggested the occurrence of a metastable zincblende polytype, a phenomenon is common for the nitride materials.[Strite and Morkoç, 1992] AlN has some outstanding physical properties that have attracted much interest. It is an extremely hard ceramic material, with a melting point in excess of 2000° C[Slack and McNelly, 1976] and rather inert to chemical etching, thus it has emerged as an attractive material for III–V nitride heterostructure owing to its wide energy band gap, high thermal conductivity (2W/cm K[Strite and Morkoç, 1992]), long durability at high temperatures and in caustic environments.[Morkoç, 1997] Because of its attractive piezoelectric properties, it was considered for surface acoustic wave devices applications.[Kline and Lakin, 1983] Further, as a wide band gap alloying material for GaN and InN, it is attractive as a barrier material for electronic and optical devices applications in the UV wavelengths range.[Monemar and Pozina, 2000] AlN also has a good thermal expansion match to SiC, $4.2 \times 10^{-6}/K$ for AlN[Yim and Paff, 1974] and $4.46 \times 10^{-6}/K$ for 6H–SiC[Liu and Edgar, 2002] along the a–axis, and a lattice constant in between 6H–SiC and w–GaN, making it an ideal buffer layer material for GaN grow on SiC. Due to its large band gap, it is also electrically insulating– ideal for microwave device applications.[Monemar and Pozina, 2000] The interest in AlN has grown markedly in recent years due to some experimental observations suggested that AlN might be a negative electron affinity (NEA) material,[Benjamin et al., 1994, 1996] though some other observations indicate that merely the affinity is rather small.[Bermudez et al., 1996, 2001; Wu and Kahn, 1999] This issue thus still under heavy debate. Nevertheless, it can potentially pave the way for cold cathodes with applications to high power vacuum electronics and flat panel displays.

Although AlN has such advantageous physical properties and promises wide applications, the studies about its fundamental electronic properties are rather limited but an important issue, since this is the basic property

for all electronic device applications. We hence again, employed the ARPES technique to study the electronic band structure of the hexagonal AlN semiconductor.

4.3.1 The Growth of w–AlN

The history of the production of AlN covers more than a century. AlN powder was first made in 1862 from liquid Al and N_2 gas.[Ambacher, 1998] However, it is difficult to grow high quality AlN crystals because of the reactivity of Al with oxygen, high purity source material and oxygen free environment were hard to achieve. Only roughly a decade ago researchers were able to grow high quality AlN using MBE and CVD techniques.[Mohammad et al., 1995] To date, bulk AlN crystals are not available commercially, but intense research to improve its crystal growth suggests that AlN substrates will be available in a few years.[Liu and Edgar, 2002]

Wurtzite AlN belongs to the same space group as wurtzite GaN and 6H–SiC; space group $P6_3mc$, with lattice constant of $a_0 = 3.11\mathring{A}$, $c_0 = 4.98\mathring{A}$,[Ambacher, 1998] in between w–GaN and 6H–SiC in (0001) surface. The lattice misfit between AlN(0001) surface and 6H–SiC(0001) surface is rather small, 1% only; this makes 6H–SiC an ideal substrate material for AlN epitaxy growth.

The AlN thin films we have studied were kindly supplied by Dr. Rizzi and Dr. Lantier from the Institut für Schicht- und Ionentechnik (ISI), Jülich, Germany. The thin films were grown on the Si–terminated 6H–SiC(0001) surface, the substrates showed a sharp (1×1) LEED pattern before the thin AlN films were deposited onto it. The AlN films were grown by the rf plasma assisted MBE method. The growth temperature was $620 - 640°C$. After thin film deposition, the overlayer also showed a clear (1×1) LEED pattern, with the same orientation as on the substrate.[Rizzi et al., 1999] AlN overlayer thickness was 20 nm. One sample was capped with 7 nm GaN to prevent surface oxidization, one was not capped.

After the transportation through the air, the as–inserted AlN samples showed no LEED pattern and no feature could be resolved in the valence band region of the photoemission spectrum. It is reasonable that, because of the highly affinity of aluminum for oxygen and the very negative Gibbs free energy of formation of Al_2O_3 $(-1.58 \times 10^6 J/mol)$[Dean, 1992], the surface had likely formed an aluminum oxide layer. It has been reported[Slack and

McNelly, 1976] that on the AlN surface an oxide 50–100 Å thick occurs when exposed for one day to ambient. However, this oxide layer is protective, since no further decomposition of the AlN samples was observed.[Slack and McNelly, 1976]

We annealed the as–inserted AlN samples to $750 - 800°C$ for 10 minutes. This procedure restored the (1×1) LEED pattern with a high background, and three clear components in the valence band region were observed. With further annealing and even Ne^{+} ion bombardment neither the LEED nor the valence band quality was improved. The Al *2p* peak after this cleaning process was broad, this is frequently observed for AlN thin films grown on a foreign substrate.[Martin et al., 1994; Bermudez et al., 1996]The binding energy of Al *2p* of AlN thin films was extracted under this condition. Its energy relative to VBM is 70.8 eV, this value is close to 70.6 eV of Martin et al.[Martin et al., 1994] and 71.9 eV of Bermudez et al..[Bermudez et al., 1996]

4.3.2 The electronic structure of w–AlN

A series of normal emission valence band spectra form AlN(0001)–(1×1) surface were taken from 28 eV photon energy to 96 eV, which is probing the $\Gamma - A$ direction along the Δ line of the bulk Brillouin zone, as described in the previous section. The left panel of Fig. 4.20 shows the whole set of spectra converted into a grey scale, darker colours indicate higher intensity. The right panel is the lower photon energy part of the valence band spectra set; all spectra are aligned with the VBM.

Three components exhibit dispersion with changing photon energy, an indication of band–to–band transition. From the lattice constant of w–AlN, the Γ point will be reached at 5.05 $\AA^{-1}$ and the A point at 4.42 $\AA^{-1}$ in reciprocal space in the direction normal to the surface. By comparing the binding energies of the components in the valence band region with the theoretical band structure calculations[Ching and Harmon, 1986; Rubio et al., 1993; Xu and Ching, 1993; van Schilfgaarde et al., 1997] and by the free electron final band assumption, the inner potential is 10.85 eV and the Γ point is reached at $\hbar\omega = 55eV$.

The range of photon energies accessible here permits the detection of direction transitions from the A point to Γ point and extends to the A point of the next zone, which covers this branch of the bands twice, such that we can fold the data points into the same zone as two independent data sets.

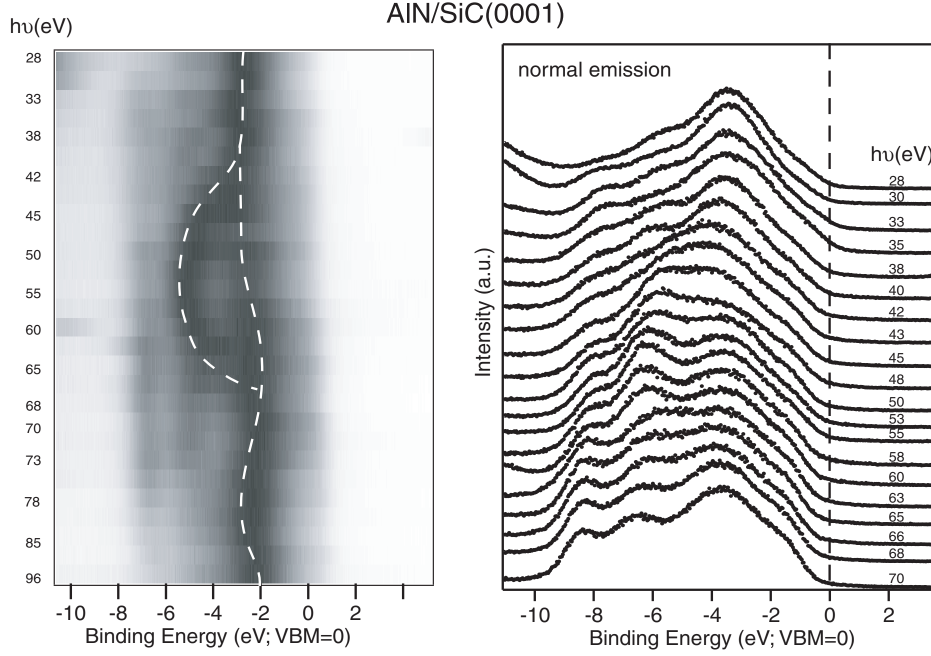

Figure 4.20: *Series of normal emission valence band spectra emitted from w–AlN(0001)–(1 × 1) surface. Photon energies were varied form 28 eV to 96 eV. Three bands are dispersing clearly. Lines are only as guides to the eye.*

The experimental band structure deduced from the set of normal emission ARPES spectra along with the LDA band structure calculation of Rubio et al.[Rubio et al., 1993] are illustrated in Fig. 4.21. The symmetry notations are after Ref. [Rubio et al., 1993]. As shown in this figure, the data points are rather scattered, especially true for the first two bands near the VBM. This is due to the fact that at this energy range, only a shoulder appears beside the most intense feature, and it is difficult to locate the peak position precisely under this condition. Furthermore, there is another band crossing these two bands in this area, which makes the situation more complex. Nevertheless, the general trends of the bands can still be followed.

The energies of the critical points of the calculated results and of experimental determinations are listed in Table 4.3. The critical point energies are the most crucial values to be compared. Unfortunately, the photoemission result does not cover the $A^{\nu}_{1,3}$ point, to which I therefore put a question mark in the table. But from the course of the data points along the Δ_3 band, the experimental $A^{\nu}_{1,3}$ point should not deviate much from the theoret-

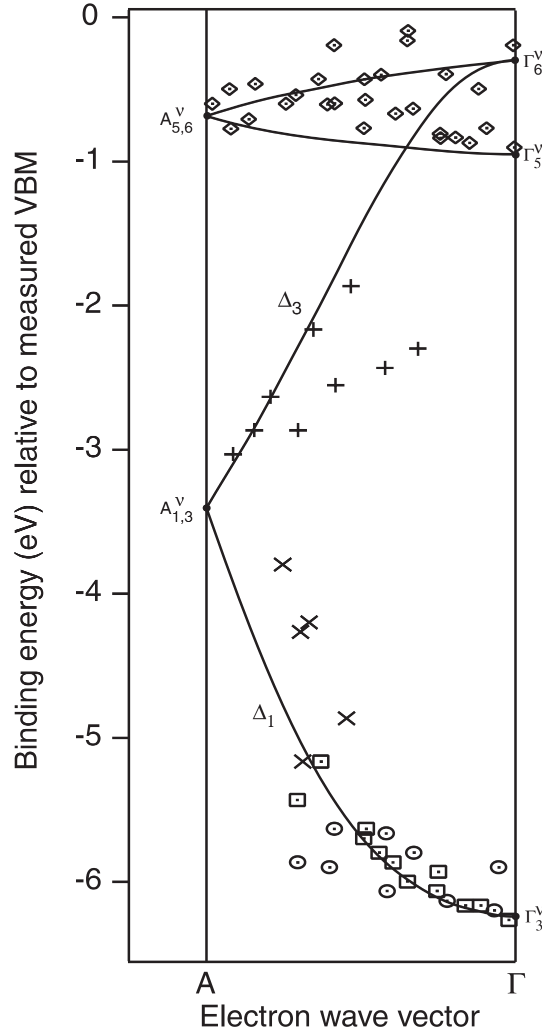

Figure 4.21: *Comparison of measured band structure for AlN thin films grown on 6H–SiC(0001) with the LDA band structure calculation (solid lines, from Ref. [Rubio et al., 1993]) of the bulk AlN bands along the* $\Gamma - \Delta - A$ *direction.*

ical value. Other than this critical point, the experimental result fits better with the LDA calculations. It is well known that LDA calculations tend to underestimate the band gap by 1.5–2 eV,[Rubio et al., 1993; van Schilfgaarde et al., 1997] while the GW approximation predicts vastly improved energy gap in semiconductors, and similar improvement is found in the nitrides.[Rubio et al., 1993] However, GW calculations are likely to overestimate band widths in general.[van Schilfgaarde et al., 1997] Our experimental observations is also supporting this point of view, see Table 4.2 and 4.3.

Table 4.3: *Critical points in the hexagonal AlN band structure from different calculations, compared with results from angle–resolved photoemission (this work), unit in eV.*

	Exp.	LDA^a	GW^a	LDA^b	$FP-LMTO^b$
Γ_3^ν	-6.10	-6.1	-6.9	-6.0	-5.9
Γ_5^ν	-0.83	-0.9	-1.1	-0.9	-0.8
Γ_6^ν	-0.19	-0.3	-0.2	-0.2	-0.2
$A_{5,6}^\nu$	-0.54	-0.6	-0.7	-0.5	-0.5
$A_{1,3}^\nu$	?	-3.4	-3.9	-3.3	-3.3

LDA: Local density approximation.
FP–LMTO: Full potential linear–muffin–tin–orbital calculation.
[a]Ref. [Rubio et al., 1993]
[b]Ref. [van Schilfgaarde et al., 1997]

4.4 Conclusions

We have applied the angle–resolved photoemission technique to study the electronic band structures of cubic InN, hexagonal GaN, and hexagonal AlN. We studied the cleaning procedures for cubic InN before the photoemission experiments were performed and found that annealing the crystal under ammonia atmosphere can clean and restore the crystalline order. The photoemission experiments probes the valence band structure along $\Gamma - X$ direction. For hexagonal GaN, we grown the thin GaN films by the MBE method with ammonia and nitrogen plasma as nitrogen sources, and compared the thin film quality and electronic structure. We have also observed a surface state on the w-GaN(0001)–(1×1) surface. AlN is another member of the group III–nitride family. We cleaned it by simply annealing under UHV conditions. Since GaN and AlN are both the wurtzite phase (0001) surface, normal emission ARPES probes the band structure along the same high symmetric line of $\Gamma - \Delta - A$ direction of the bulk Brillouin zone for both crystals. All of the experimental band structures from these crystals were compared with the theoretical calculations and found to be in general agreement.

Chapter 5

The SiC/GaN Heterointerface

A piece of semiconductor itself does not have much of a practical use. It has to be combined with other materials to form junctions to make it useful. One is to grow a metal on a semiconductor, to form a metal–semiconductor interface; we will turn to this in next chapter. The other way is binding two semiconductors to make a semiconductor–semiconductor junction.

This kind of junction has two different types. Binding the same semiconductors with different doping properties together makes a homojunction, and by combining different semiconductors a heterojunction is formed. For heterojunctions, those different semiconductors normally have a common crystal structure and the lattice mismatch is the smaller the better, in order to avoid a strain–induced electric field between the semiconductors and the formation of gap states.

Heterojunctions offer extra degrees of freedom in the design of semiconductor junction devices, which have widespread applications in modern solid state electronics, including heterojunction bipolar transistors, field–effect transistors and semiconductor lasers. In addition, by forming periodic layered heterojunctions with ultrathin layer thickness, roughly in the range of some tens of Å and up to as high as 60 periods for semiconductor laser, one can form so–called multiple–quantum–well structures, which allows us to control the carrier injection and carrier confinement for high speed and optoelectronic devices.[Weisbuch and Vinter, 1991]

As briefly discussed in chapter 1, current research about GaN and its alloys mainly focuses on heterojunction device applications, following improvements in material quality. Thus, an investigation on the band offset at heterojunctions of nitrides and other materials is important for device design,

modelling, and performance prediction.

6H–SiC is well lattice matched with GaN; as discussed in chapter 4. GaN/SiC heterojunctions have been used as the emitter–base junction in high temperature transistors. These transistors had an extraordinary high current gain at room temperature up to 10^7 and were able to operate at 530 ℃ with a current gain of 100[Torvik et al., 1999]. Furthermore, from a theoretical point of view, only polar semiconductor interfaces are likely to permit a band–offset modification.[Franciosi and de Walle, 1996] For example, the (110) interface is a nonpolar interface, each (110) plane consists of an equal number of cation and anion sites. Replacing a complete plane of host atoms with another type of atoms will therefore have no net effect. In order to form a dipole at the interface, one would have to substitute only the cation sites in one plane and only the anion sites in a different plane, or vice versa. However, such atomic swaps seem unlikely, there is experimental evidence that offset modification at nonpolar interfaces can occur.[Franciosi and de Walle, 1996] The hexagonal GaN on SiC(0001) system is a typical polar interface, this increase their importance for the theoretical calculation. Therefore, it is interesting to investigate the heterointerface properties and the valence band offset of this heterojunction.

5.1 Heterojunctions

When semiconductors of different band gaps (E_g) and electron affinities (χ) are brought together to form a junction, we expect discontinuities in the energy bands as the Fermi levels line up at equilibrium. Figure 5.1(a) shows the band diagram before two intrinsic semiconductors join together; the semiconductor A has a larger band gap. A band diagram for the interface region of a thin, abrupt heterojunction after these two semiconductors are brought together is given in Fig 5.1(b), along with an arbitrary shallow core level in semiconductor A with binding energy E_{CL}^A, shallow core level in semiconductor B with binding energy E_{CL}^B, their energy difference $\Delta E_B(A-B) = E_{CL}^A - E_{CL}^B$; all these binding energy are relative to the Fermi level. Note that the bands on either side of the interface are depicted as flat, since we are only interested in a region on the order of a few atomic distances around the interface, and these bands can be treated as flat in this situation. From the diagram we easily derive the following equation

$$\Delta E_v(A-B) = \Delta E_B(A-B) + (E_{CL}^B - E_v^B) - (E_{CL}^A - E_v^A) \quad (5.1)$$

where $\Delta E_v(A - B)$ is the heterojunction valence band offset, $(E_{CL} - E_v)$ are the energy differences between the core level binding energy and VBM, and $E_g^A \geq E_g^B$. If $E_{CL}^A < E_{CL}^B$, the ΔE_B will be negative. And no matter how these two semiconductors will align with each other, the discontinuities in the conduction band ΔE_c and the valence band ΔE_v will accommodate the difference in band gap ΔE_g between the two semiconductors; e. g. $\Delta E_g = E_g^A - E_g^B = \Delta E_c + \Delta E_v$. How photoemission can be utilized to measure these quantities and determine ΔE_v will be discussed later.

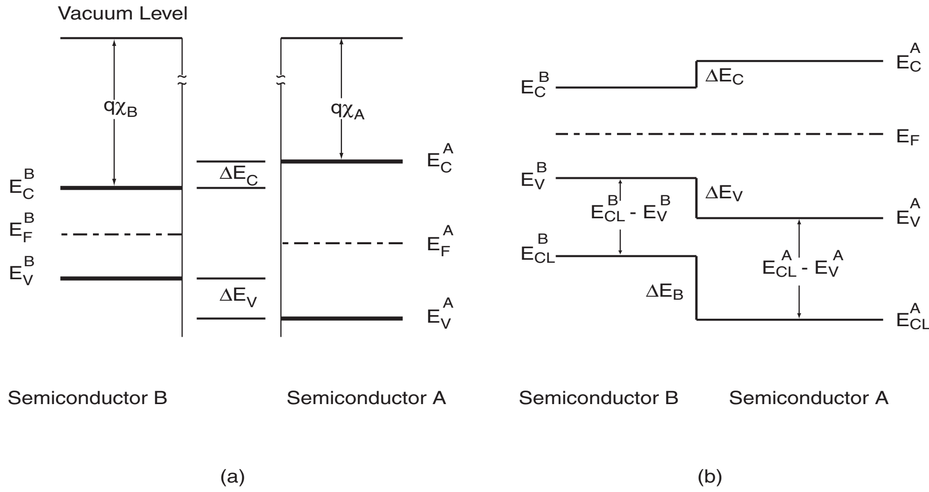

Figure 5.1: *(a) Ideal band diagram of two intrinsic semiconductors before joining, and (b) schematic energy band diagram of thin, abrupt heterojunction interface with arbitrary shallow core level.*

In thermal equilibrium, the Fermi levels of these two semiconductors will line up, and if we assume an abrupt interface, the various types of band alignment can be characterized by the way how the band edges of the smaller–gap semiconductor are located relative to the band gap of the second semiconductor . They can be categorized into three categories, e.g. straddling (or normal), staggered and broken gap [Horn, 1990], as indicated in Fig. 5.2. The discontinuities in the valence and conduction bands at the interface between the two materials determine its possible applications. The most common alignment is the "straddling" type (type I), in which the discontinuities at the valence band and conduction band point in opposite directions. For this kind of alignment, both electrons and holes are pushed by the barriers from

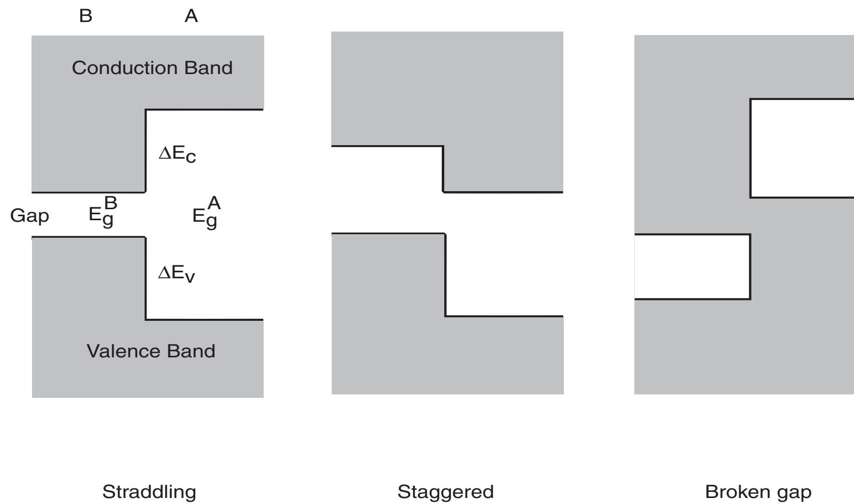

Figure 5.2: *Schematic drawing of the three different band alignments found in semiconductor heterojunctions.*

the wide–gap to the narrow–gap side of heterojunction. A fairly rare species is the "staggered" type (type II) line up. Opposite to straddling alignment; the discontinuities of these two bands are in the same direction. This arrangement has important advantage for applications where spatial separation of electrons and holes are required, such as solar cells or photodiodes. The "broken gap" type (type III) is a very special alignment, the InAs/GaSb is the only known heterojunction of this type.[Kroemer, 1983]

5.2 Investigation of Semiconductor Heterojunctions Using Photoemission

To determine the heterojunction band offset, several methods were developed in the past decades; for example, transport methods, optical methods, and photoemission spectroscopy.

Transport methods were essentially the only methods available to probe heterojunction band discontinuities, as well as Schottky barrier heights in metal–semiconductor contacts, before photoemission was applied to this field. [Henisch, 1984] Optical methods include absorption, luminescence, light scat-

tering and internal photoemission spectroscopy. Amongst all of these methods, photoemission spectroscopy has the unique advantage that it is the most surface sensitive technique. It can probe down to the monolayer scale to study the details of the interface formation. Therefore, most photoemission determinations of the band offset focus on semiconductor heterostructures comprised of relatively thin semiconductor overlayers grown *in–situ* or *ex–situ* on top of a suitable substrate. Typical overlayer thicknesses employed vary from 5 to 30 Å, depending on the photon energy and the corresponding photoelectron escape depth. Moreover, the band offset can also be measured as a function of overlayer thickness. This is important for a critical assessment of current theories concerning valence band lineup in heterojunctions.

Semiconductor heterojunctions are usually prepared by either molecular beam epitaxy (MBE), metal–organic chemical vapor deposition (MOCVD) or liquid phase epitaxy (LPE). But for *in–situ* studies in an ultra high vacuum environment, MBE is the best way. By controlling the molecular beam intensity, one can control the deposition rate precisely.

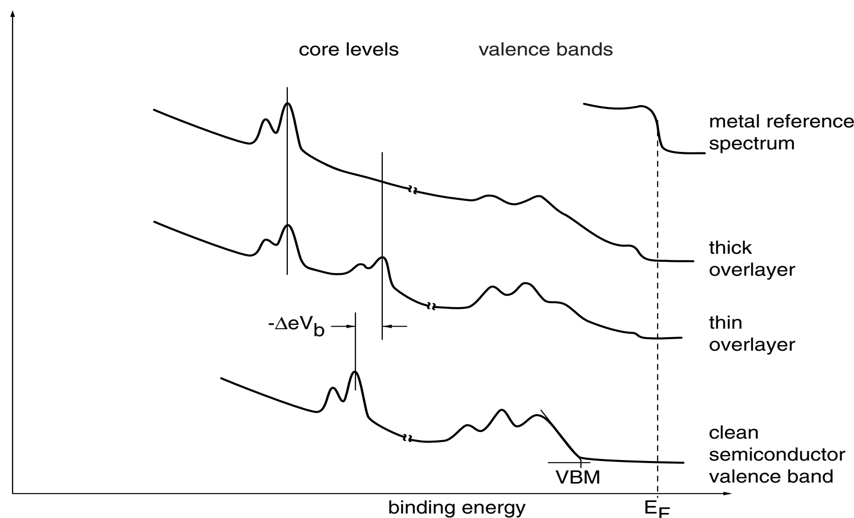

Figure 5.3: *Method of determining valence band offsets in photoemission from semiconductor heterjunctions. The shift in the valence band maximum is corrected for the band bending which occurs upon interface formation by measuring the shift of a particularly sharp and intense bulk core level from the substrate.*

In a photoemission experiment involving semiconductor surfaces, the valence band region is normally measured along with an accessible core level, as indicated in the lowest spectrum of Fig. 5.3. Since the reference level for the determination of electron kinetic energy in photoemission experiments is the Fermi level (E_F) of the electron energy analyzer, which has electrical contact with the samples, changes in the position of E_F in the semiconductor substrate due to band bending will cause a shift of whole photoelectron spectrum relative to this reference level. Band bending can be caused by a variety of processes. One of them is deposition of foreign materials on the surface of the semiconductor, causing a depletion or accumulation layer in the surface.[Mönch, 1993]

Therefore, the shift of valence band maximum (VBM) due to the deposition of foreign material on the substrate; as shown in Fig. 5.3, is not necessarily only due to the formation of valence band offset, it is a mixture of the band bending and valence band offset. The change in band bending (eΔV_s) can be measured by the shift of the core level emission line. However, this method has its disadvantage. Since core level lines frequently change their shape due to the occurrence of chemically reacted species, disappearance of surface core level shift etc. Only the shift of the bulk core level contribution to the peak actually reflects the band bending.[Horn, 1990] Normally people apply numerical line shape analysis ("curve fitting") to distinguish the different chemical components in the core level line. We can utilize this method to identify the bulk core level line from other components.

To perform a line shape analysis, we use a non–linear least square fitting procedure programmed by Theis.[Theis, 1989] The photoemission lines are modelled by Lorentzians, which are broadened by numerical convolution with a Gaussian in order to take into account instrumental and other broadening mechanisms. Spin–orbit partners are related by the branching ratio for the intensities and the spin–orbit splitting for the energy separation of the peaks. The background function used in this procedure consists of a third–order polynomial expression plus a broadened step function according to Shirley.[Shirley, 1972] These parameters are varied in order to minimize the difference between model and data. The optimization process uses the Levenberg–Marquardt algorithm.[Bevington, 1969] The free parameters are not constrained to a particular range of values during least squares (χ^2) optimization. Confidence intervals for each parameter are calculated by obtaining the change in the values of one parameter for one standard deviation in the normalized χ^2, with all other parameters relaxed.[Bevington, 1969] Such confidence parameters permit a judgement about the reliability of the

fit and model function.

I would like to make some comments about the background separation here. In the routine developed by Theis, the background is considered as part of the line shape analysis, in contrast to other authors, Himpsel et al.,[Himpsel et al., 1990] for example, subtract a measured secondary electron background from their spectra, then decompose the spin–orbit splitting before the actual line shape analysis is performed. Hricovini et al.[Hricovini et al., 1990] employ a similar procedure. They first subtract a second degree polynomial from the spectra to account for the background and then decompose the spectra into "same–shaped" spin–orbit split contributions. After these steps, the actual line shape analysis is conducted. The authors argue that this procedure reduces the number of free parameters in the line shape analysis. This is desirable because a meaningful model is harder to find with a large amount of free parameters. It must be clarified at this point that the background subtraction and spin–orbit de-convolution is already part of the analysis. Erroneous subtraction and de-convolutions will lead to artifacts in the line shape analysis conducted in succession. In Theis's program, such a separation of background treatment and the spin–orbit splitting from the line shape analysis, was not conducted in order to avoid artifacts. The background treatment, as well as the spin–orbit splitting are regarded as integral parts of the fitting. We consider this a distinct advantage of the procedure used here.

Through the curve fitting we can determine the energy of the bulk core level line. Another value that also has to be determined is the position of the VBM, since it is more difficult to locate. The VBM spectra from bulk SiC(0001) surface, thin GaN(0001) on SiC and thick GaN(0001) overlayer were recorded and are shown in Fig. 5.4, all of those spectra were recorded in normal emission condition with 130 eV photon energy. Some authors had used curve fitting to deconvolute the movement of the VBM, hoping to determine the band offset more precisely.[Yu et al., 1993] This method works in a system that no or very few interface reaction occurs and does not form new mixed phases in the interface. Therefore, the valence band emission from the interface is simply a superposition of substrate–related and overlayer–related valence band spectra. For the present system, however, this criterion is not fulfilled, since we had exposed clean SiC surface under nitrogen plasma or ammonia atmosphere to nitride the SiC surface prior the growth of GaN.[Ploog et al., 1998]

Therefore, the VBM positions of the SiC/GaN interface were determined

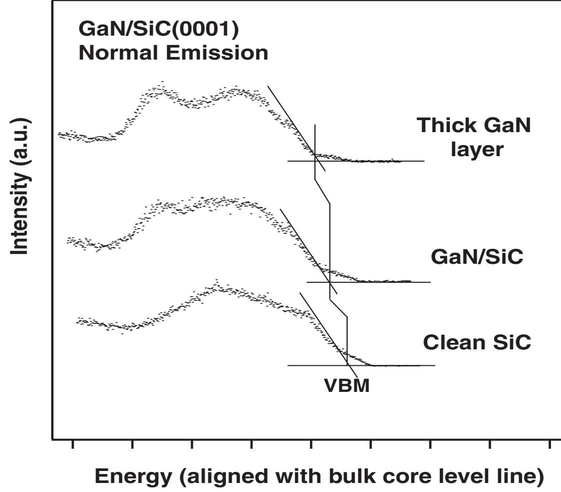

Figure 5.4: *Valence level spectra of GaN on SiC(0001) recorded in normal emission condition at 130 eV photon energy. The shape changing of the spectra indicate the gradual emergence of the GaN valence band. Note the valence band maximum position moved as the GaN overlayer forms.*

by a linear extrapolation of the leading edge of the valence band spectra. However, we can see from those spectra that some emission exists between VBM and E_F, which is called gap emission,[Ley et al., 1979] because they exist inside the energy gap. Gap states are usually introduced through compositional disorder or translational disorder,[Cohen et al., 1969] namely, through the existence of impurities or defects. Gap emission is common in GaN valence band spectra, see the valence spectra in reference[Dhesi et al., 1997] and [Ding et al., 1996]. The gap emission shoulder makes it more difficult to locate the leading edge and increase the uncertainty while determine the VBM position. After repeated tests on a large number of measurements indicate that ±0.05 eV is the typical accuracy in determining VBM position with this approach.

5.3 Core Levels

The valence band maximum is used as reference, and we located the binding energies of Si *2p* and Ga *3d* peaks from bulk SiC(0001) and GaN(0001)

surfaces by data deconvolution described briefly before.The Si *2p* peak from the unreconstructed clean SiC(0001) surface is shown in Fig. 5.5. The fitting parameters for the Si *2p* peak are as follow: spin–orbit branching ratio is 0.53 ± 0.03, which is in good agreement with the low temperature (77 K) and high instrumental energy resolution measurement[Wertheim et al., 1991]. The spin–orbit splitting is 627 ± 10 meV, which is somehow larger than the 602 ± 6 meV obtained from silicon (100) surface by Wertheim et al.[Wertheim et al., 1991]. The spectrum and the fitting are shown in Fig. 5.5, along with the residuals of the deconvolution. The lack of surface core level shift and other silicon bond forming suggests that the surface is clean but very well ordered. The lack of surface order can also be confirmed by the large spot of (1×1) LEED pattern.

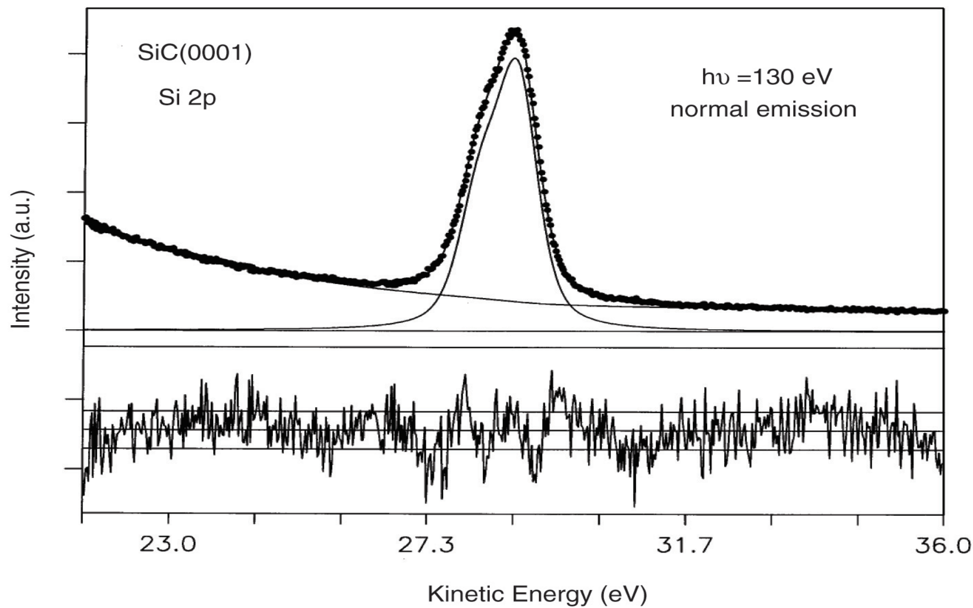

Figure 5.5: *Core level spectrum of the Si 2p peak from clean SiC(0001) along with line shape analysis. The spectrum was recorded in normal emission condition with 130 eV photon energy. Dots are the data points, solid lines are the fitting result and background. Below the spectrum is the residuum of the fit. See text for the detail description of the analysis.*

For a medium GaN thickness, the spectra are more difficult to interpret, since the Si *2p* peak is weaker and reacted components showed as well. In order to distinguish the different chemically reacted species in this peak, we made some constrains and assumptions for the curve fitting process. Since all peaks are Si *2p*, we used the same spin–orbit–splitting and branching ratio

as the bulk Si, i. e. 627 meV and 0.53, respectively, and fix these two values for all components. Next we assumed that there are four chemical reacted species in this peak, they are Si–C, Si–N, Si–Ga bonds and free Si atom, each bond shifts the Si *2p* line a different energy shift. This is a rough guess, and may not be correct, since one does not really know the detailed chemical processes happened during different growing period. From the literature, we can find that the Si–Ga bond will shift a Si *2p* line to lower binding energy by 0.6 eV,[Lu et al., 1989] the Si–N bond will shift it to higher binding energy by 0.3 to 2.4 eV[Rignanese and Pasquarello, 2001]; this depends on how many nitrogen atoms attach with silicon atom. A Si–C bond will shift the line about 0.2 to 0.3 eV to higher binding energy.[Terry et al., 1999] All of these energy shifts are referred to the bulk Si $2p$ line. We started the fitting with these parameters but didn't fix the energy differences. The Gaussian and Lorentzian widths were also set variable while we were doing curve fitting. Fig 5.6 shows the fitting result from the parameters described above.

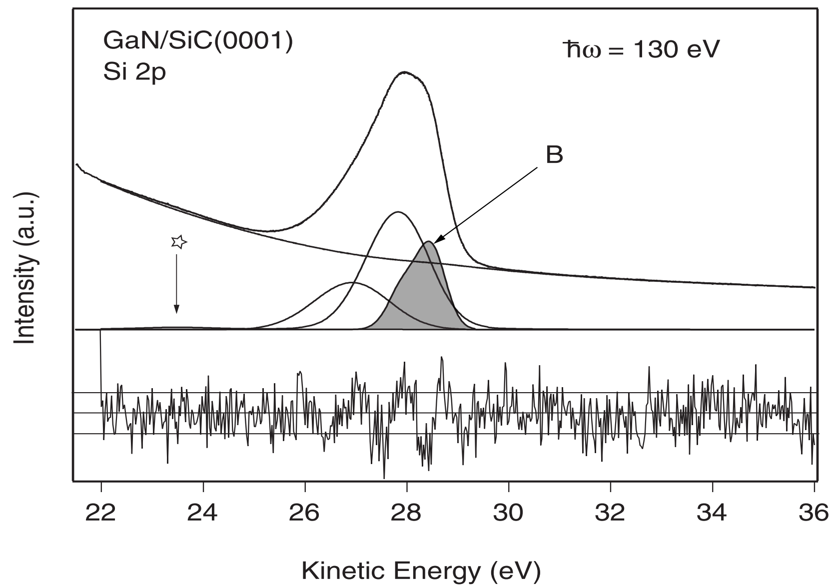

Figure 5.6: *The line shape analysis of Si 2p core level spectrum from SiC(0001) surface covered with thin GaN overlayer. The shaded component is the bulk Si peak from SiC substrate. See text for the details. The astroid indicates the Ga 3p signal from the thin GaN overlayer.*

As the figure indicates, there are three components in the Si $2p$ core level line. The "**B**" component, as pointed in the figure, is the Si–C bond from the underlying SiC substrate, since its energy position is exactly the same as the

bulk Si 2p signal from the clean SiC surface as the peak in Fig. 5.5. The energy shifts of the other two components relative to this peak are 0.48 eV and 1.38 eV (from right to left), respectively. According to table 5.1, these are the silicon nitride species, and they are Si–Si_2N_2 bond (middle component) and the Si–N_4 bond (left component). From the numerical deconvolution, there is no indication of the formation of a Si–Ga bond. This result is consistent with Boscherini et al.,[Boscherini et al., 1999] who used polarization–dependent x–ray absorption spectroscopy to study the GaN/SiC interface, and found no evidence for a mixed Ga/Si interface plane.[Boscherini et al., 1999] Also, no free silicon atoms were released in the interface, or at least their concentrations were below the detection limit of photoemission spectroscopy. This indicates that at the GaN–SiC interface region, only silicon–nitrogen bonds are formed. This is the direct result of the SiC surface nitridation prior to the GaN growth. This surface nitridation process will increase the SiC(0001) surface energy and improve the wetting of Ga on the SiC surface,[Ploog et al., 1998] which will lead to 2D GaN growth, as described in chapter 4.

Configuration	Δ(eV)	Ref.
Si–Si_4	0	
Si–Ga	-0.6	[Lu et al., 1989]
Si–C	+0.2 – +0.3	[Terry et al., 1999]
Si–Si_3N	+0.5 – +0.7	[Rignanese and Pasquarello, 2001]
Si–Si_2N_2	+1.5	[Rignanese and Pasquarello, 2001]
Si–N_4	+2.4	[Rignanese and Pasquarello, 2001]

Table 5.1: *List of different Si* 2p *core level chemical shift. Si–Si bonding is served as reference energy, plus sign means shift to higher binding energy.*

We have to emphasize here that the fitting result is not a single event. We have deconvoluted many Si 2p spectra with different GaN thickness and different nitrogen sources, all of them have these three components and the same energy separations, only the relative intensities are different. This is also an important criterion of the reliability for the curve fitting.

However, for the Ga 3d core level line, the results are different. The Ga 3d peak is always broad, and featureless. Many different ways were tried, but it is very difficult to reach a reasonable line shape result. Even with different thicknesses and different nitrogen sources, the line shape is almost the same. This broad, featureless Ga 3d peak was also observed by other gallium nitride researchers.[Dhesi et al., 1997; Bermudez et al., 1993]

We locate the Ga $3d$ position by fitting one component in this peak, as suggested by Bermudez.[Bermudez, 1998] The spin–orbit splitting and branching ratio were fixed at 0.46 eV and 0.61, respectively.[Miller and Chiang, 1984] The procedures were similar to those for the Si $2p$ peak.

With the knowledge of both the bulk core level line positions from substrate and overlayer, we are ready to determine the band bending ΔeV_b as indicated in Fig. 5.3, and find the valence band offset through

$$\Delta E_v = E^{VBM}(substrate) - E^{VBM}(overlayer) - \Delta eV_b \tag{5.2}$$

From the magnitude of the fundamental gap, which is tabulated, the conduction band offset can also be deduced. The band alignment of the GaN/SiC(0001) interface for different nitrogen sources are shown in Fig 5.7. With an energy gap of 3.4 eV for GaN[Ambacher, 1998] and 3.0 eV for 6H–SiC[Porter and Davis, 1995], and a valence band discontinuity of 1.10 eV for plasma growth GaN, 1.02 eV for ammonia growth GaN, the conduction band offsets are then 0.7 eV and 0.62 eV for a plasma–grown and ammonia–grown sample, respectively. The band diagram shows that the GaN/SiC heterojunction is of the staggered type (type II) alignment.

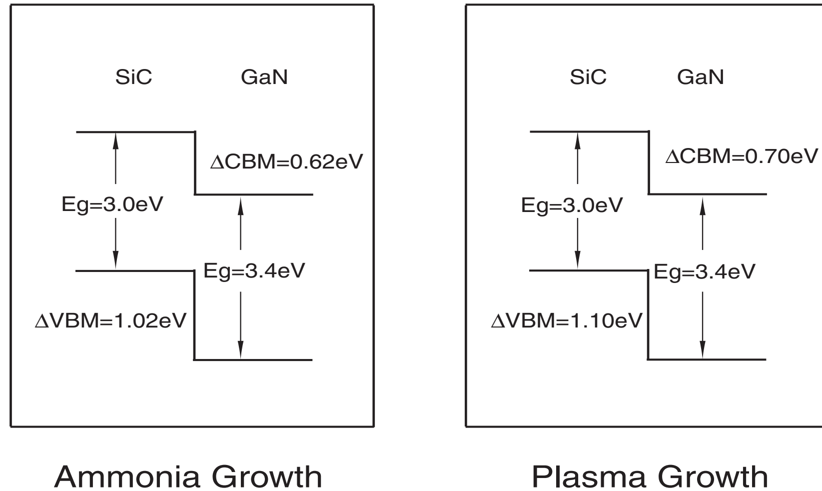

Figure 5.7: *Schematic diagrams of the band alignment at the GaN/SiC(0001) interfaces, which were grown with different methods.*

There have not been many theoretical calculations applied to the wurtzite GaN/SiC heterointerface yet. However, the valence band offset values of our result agrees rather well with Harrison and Tersoff's simple model[Harrison and Tersoff, 1986].With the Linear Combination of Atomic Orbitals (LCAO) method and by including nearest–neighbor interactions, the VBM (ϵ_v) relative to vacuum level can be calculated by[Harrison, 1989]

$$\epsilon_v = \frac{\epsilon_p^c + \epsilon_p^a}{2} - [(\frac{\epsilon_p^c - \epsilon_p^a}{2})^2 + (\frac{1.28\hbar^2}{md^2})^2]^{\frac{1}{2}} \tag{5.3}$$

Here ϵ_p^a and ϵ_p^c are the p–state eigenvalue of the anion and cation atoms, d is the bond length, and the last term derives from a universal form for the interatomic coupling. The values are linearly related to the experimental photothreshold as shown in Fig. 5.8[Harrison, 1999] over a large range of semiconductors. The empirical relation of the linearity is

$$\Phi = |E_v| - 4.2\ eV \tag{5.4}$$

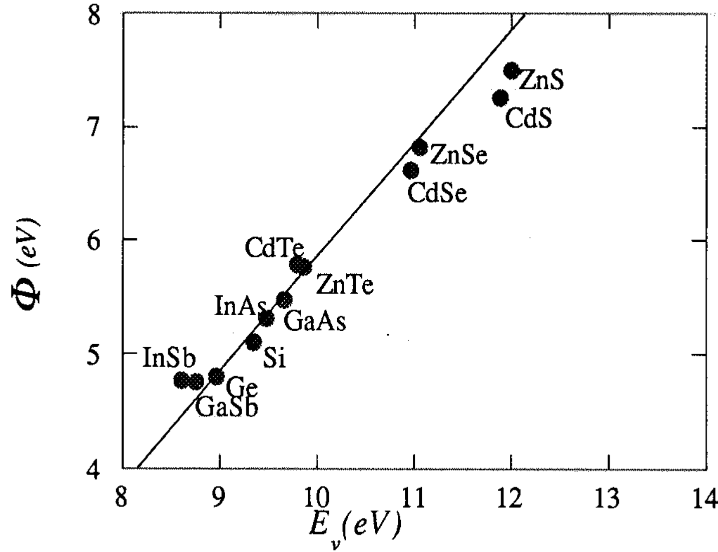

Figure 5.8: *The experimental photothreshold Φ, plotted against the energy of the valence band maximum E_v calculated by LCAO method. The line corresponds to the empirical relation.*

It is therefore natural to assume that the valence band discontinuity is the difference of the VBM of the corresponding semiconductors, as proposed

by Harrison[Harrison, 1977], and the alignment may be called "natural lineups". This method predicted some of the semiconductor heterojunctions offset well, but it showed poor agreement in other cases, since it did not include the interface dipole in the calculation.[Harrison, 1999] Tersoff has argued that at semiconductor heterojunctions, interface dipoles arise which can be quite large. These interface dipoles would shift the energy levels on the two sides and modify the natural band lineups.[Tersoff, 1984]

In 1986, Harrison and Tersoff produced a tight–binding theory of heterojunctions and interface dipoles[Harrison and Tersoff, 1986] that is related to the concept of the charge neutrality level (CNL)[Franciosi and de Walle, 1996], a concept postulated by Tersoff in 1984[Tersoff, 1984]. The idea is that the existence of interface dipoles will shift the bands of two semiconductors such that the CNLs line up across the interface, in analogy to the Fermi–level pinning in Schottky barriers.[Harrison and Tersoff, 1986]

The proximity of another material at the interface induces a distribution of states in the gap of semiconductor. In the case of a metal, these states would be related to tails of metal wave functions, and the states are commonly referred as metal–induced gap states (MIGS).The induced states can carry a certain amount of charge, depending on what fraction of them are filled. Any electronic state in the gap of a semiconductor, including the CNL, is necessarily a mixture of valence and conduction band states. The closer the state is to the valence band edge, the more valence character it has but it always includes a certain admixture of conduction band wave functions. The reverse is true for the gap states near the conduction band. The CNL occurs where the gap states have equal valence and conduction character. The occupation of a state in the gap leads to a local excess of electronic charge is proportion to its degree of conduction character. If the gap state is empty, there is a local positive charge in proportion to the valence character of the states. If the state lies near the bottom of the gap, filling it corresponds only to a slight negative charge, since little conduction character is involved. Leaving that state empty, however, results in a deficit of about one electronic charge (approximately one hole in the valence band). It is this behaviour of the CNL that is responsible for controlling the band alignment of an ideal semiconductor heterostructure. From the model of Harrison and Tersoff, therefore, the CNL is the energy level for lining up the semiconductor heterojunctions. For an ideal semiconductor heterojunction the alignment of the CNL $E_{CNL}(A)$ and $E_{CNL}(B)$ in the two semiconductors directly yields the valence band offset as

$$\Delta E_v = (E_{CNL}(A) - E_v(A)) - (E_{CNL}(B) - E_v(B)) \tag{5.5}$$

From the table 19-1 of reference [Harrison, 1999], the energy differences of the VBM relative to the CNL of SiC and GaN are 1.32 eV and 2.55 eV, respectively. The theoretical valence band offset of GaN/SiC would therefore be 1.23 eV, type II alignment. Compared with our experimental VBOs of 1.10 eV for plasma growth and 1.02 eV for ammonia growth, the agreement is rather good.

In conclusion, we have grown GaN on SiC(0001) surface by the MBE method with two different nitrogen sources, as described in a previous chapter. With the aid of numerical line shape analysis, we can identify the bulk core–level signal from other chemical components and evaluate the band alignment of this heterostructure. From the *in-situ* photoemission measurements, the band of GaN grown on SiC is of staggered type (type II) alignment, which has the potential applications for the devices that need to separate the electrons and holes in the interface region, such as solar cell or photon detector. The valence band offset of semiconductor heterojunction is an important parameter to determine the availability of theoretical calculations. The experimental valence band offset of the GaN/SiC heterointerface is 1.10 eV for plasma grown GaN and 1.02 eV for ammonia grown GaN on SiC(0001) surface. These values are rather close to the theoretical value predicted by the CNL alignment model.

Chapter 6

Metal–Nitride Interfaces

Not only semiconductor–semiconductor junctions are important, but metal–semiconductor (MS) contacts also play an important role in the field of semiconductor physics. Every semiconductor electronic device needs metal contacts to form electrodes and diodes. As is well known, device performance largely depend on the quality of the MS contacts. Therefore the study of the formation of metallic contacts and Schottky barrier heights in metal–nitride systems is of great relevance. As an example, the performance of GaN–based laser diodes is still limited by the difficulty in making low–resistance Ohmic contacts. In this regards, the presence of interface states seem to play an important role in Schottky barrier formation.[Picozzi et al., 2000]

Aluminum nitride (AlN) is the most frequent used material as a buffer layer for GaN growth.[Liu and Edgar, 2002] AlN and GaN have the same structure (isomorphic) and their lattice constant and thermal expansion coefficients are very similar,[Strite and Morkoç, 1992] thus, abrupt compositional junctions that are relatively free of strain can be achieved. However, the electronic properties of AlN have not received the same attention as GaN, even though it has its own merits as a wide band gap semiconductor and may exhibit a low or negative electron affinity.[Benjamin et al., 1994, 1996; Bermudez et al., 1996] It is therefore worthwhile to study the metal–GaN as well as metal–AlN interfaces.

Noble metals are monovalent metals with well known electronic properties and have widespread applications in the semiconductor industry. A study of the noble–metal/nitride contacts can also reveal the effect of d states on the Fermi–level position, which has been thought to be important in the case of GaAs interfaces.[von Schilfgaarde and Newman, 1990] In this work, we deposited silver films on GaN(0001) and AlN(0001) surfaces to form metal–

semiconductor junction and studied the barrier formation of these two interfaces.

6.1 Metal–Semiconductor Interfaces

When a metal–semiconductor interface is formed, a rectifying contact or ohmic contact will result, depending on the type of metal and semiconductor used. Both cases are equally important. Rectifiers are widely utilized in electronic devices, e.g. to convert alternating current into direct current. On the other hand, all semiconductor devices need contacts in which the electrons can easily flow in both directions, this will need ohmic contacts, which name is used because their current–voltage characteristic obeys Ohm's law.

In honour of Walter Schottky, who first attributed the rectifying behaviour of MS contacts to depletion layers at the interface, such metal–semiconductor interfaces are called Schottky barriers. Rectifying MS junctions are also named Schottky contacts or Schottky diodes.[Mönch, 1990]

The current transport in Schottky barriers is governed by the barrier height of the depletion layer. This barrier height is defined as the energy difference from the Fermi level to the valence band top or the conduction band bottom at the interface for semiconductors doped p– and n– type, respectively. (see Fig. 6.1). From the definition, we can see that the barrier heights are the energy barriers the charge carriers must overcome when they want to cross through the MS interfaces.

The magnitude of the Schottky barrier height largely determines the rectification properties of the metal–semiconductor contact. The first–order theory of the formation of a Schottky barrier was proposed by Schottky and Mott independently, and resulted in the famous Schottky–Mott rule:[Mönch, 1990]

$$\Phi^{\mathrm{n}}_{\mathrm{SB}} = \phi_{\mathrm{m}} - \chi_{\mathrm{s}} \qquad\qquad \Phi^{\mathrm{p}}_{\mathrm{SB}} = \mathrm{E_g} - (\phi_{\mathrm{m}} - \chi_{\mathrm{s}}) \tag{6.1}$$

ϕ_{m} is the metal work function, χ_{s} the electron affinity of the semiconductor and $\mathrm{E_g}$ the semiconductor gap.

From this rule, one expects to tune the barrier height by depositing metals with different work function. However, the Schottky–Mott relationship has received little support from experiment.Figure 6.2 shows measured Schottky

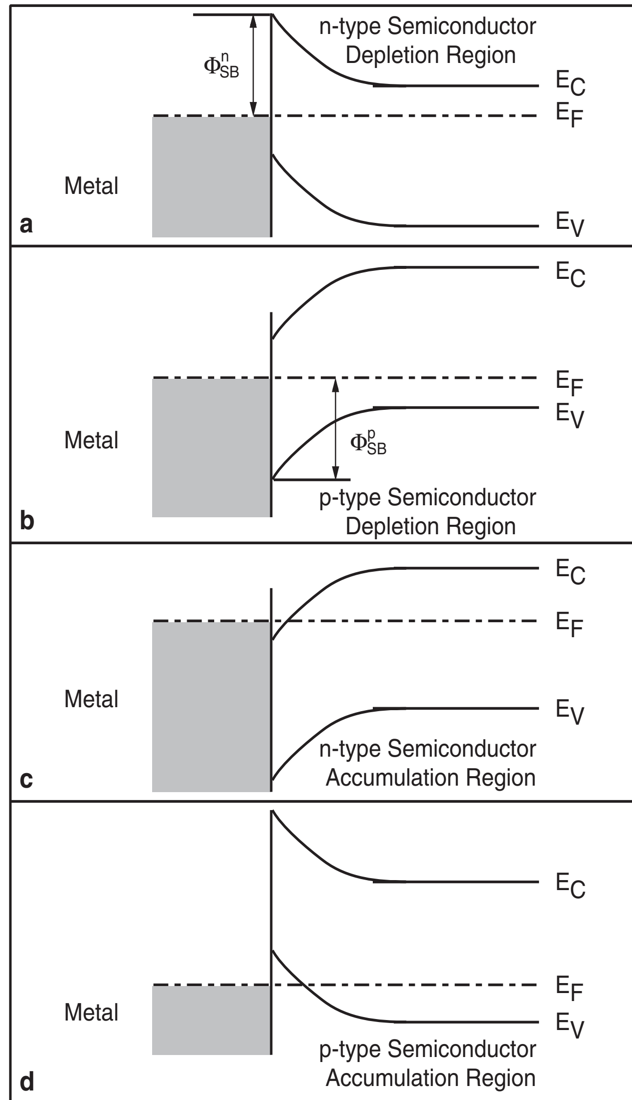

Figure 6.1: *Four different cases of the band bending after metal–semiconductor contacts were formed. (a) and (b) are the Schottky contacts for n–type and p–type semiconductors, respectively.The definitions of Schottky barrier heights (Φ^n_{SB}) and (Φ^p_{SB}) are also illustrated. (c) and (d) are ohmic contacts. For them, the charge carriers can transport through the interface without barriers to overcome.*

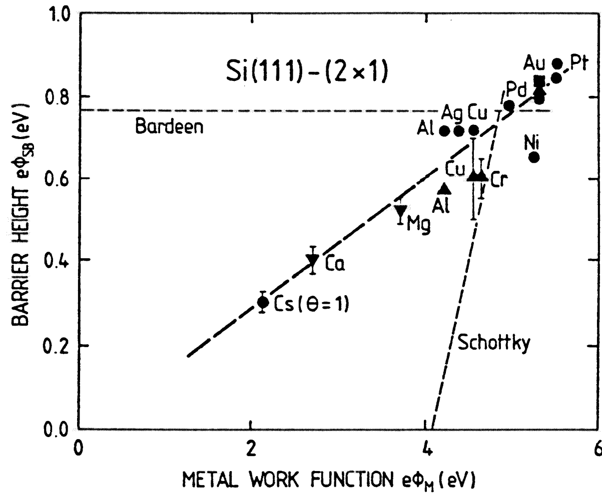

Figure 6.2: *Barrier heights of Si–Schottky contacts versus metal work function. The data were obtained by different researchers from measurements on the metal–covered Si(111)-(2×1) cleaved surface. For comparison the predictions of the Schottky–Mott model (no interface states) and the Bardeen model (high density of interface states) are given.[Lüth, 1997]*

barrier heights for metals with various work functions deposited on UHV–cleaved Si(111)-(2×1) surfaces. According to the Schottky–Mott model one would expect a much greater variation of the barrier height with work function than is experimentally observed.

Another model also shown in the figure is called Bardeen model, [Bardeen, 1947] to explain the deviation of experimental data from the Schottky–Mott model. He assumed that the intrinsic localized surface states of the clean semiconductor surface persist under the metal overlayer, and that they pin the Fermi level. The work function of the deposited metal would thus has no effect on the position of the Fermi level at the interface. (The dashed horizontal line in Fig. 6.2.) The assumptions of this model are flawed, since the surface states of the clean surface are strongly affected by metal deposition.

From the figure we can see that the real Schottky barrier heights are somewhere between these two extreme cases. This is the trend that we want to study in the metal–nitride interfaces.

Schottky barrier heights are usually determined from current–voltage, capacitance–voltage or photoresponse–wavelength characteristics. [Mönch, 1990] Such data, however, do not directly provide insight into the microscopic mechanisms determining barrier heights in MS interface or the chemical status while the barriers are forming. With surface–sensitive experimental tools, such as photoemission spectroscopy, the variation of the Fermi level within the band gap at the surface can be monitored as a function of the amount of metal deposited on an initially clean semiconductor surface.[Horn, 2000] In these studies, the surface band bending as a function of metal coverage is derived from shifts in a substrate core level line which may be detected even for thick overlayers (up to tens of Å). Such shifts are then interpreted as reflecting the position of the Fermi level in the band gap. This is similar to the heterojunction band offset determination method described in previous chapter, we therefore will not go into detail in this chapter.

6.2 Sample Preparation

The silver films were evaporated from a water–cooled Knudsen cell, which was described in chapter 2. The fluctuation of cell temperature was controlled within ±1°C during film depositions. Cell temperature and nominal deposition rate relation was measured prior to the experiments with a quartz microbalance, which was placed at the sample position to reduce the instrumental error.

The silver deposition rate was controlled as 1 Å per 30 seconds and depositions were performed stepwise. Each step we deposited a nominal thickness of 1 to 3 Å of Ag. After each deposition we took the spectra of substrate core level and the Fermi edge area, then deposited Ag again. These procedures were repeated until the core level peaks had totally disappeared.

6.3 Schottky Barrier Heights

Figure 6.3 shows the Ga $3d$ core level peak emitted from a clean GaN(0001) surface at room temperature and liquid nitrogen temperature with 49 eV photon energy. In order to minimize the spectrum shift from the photon source, we did not change any beamline parameter during the experiment. The peak shifted to higher binding energy upon decreasing temperature, which is due

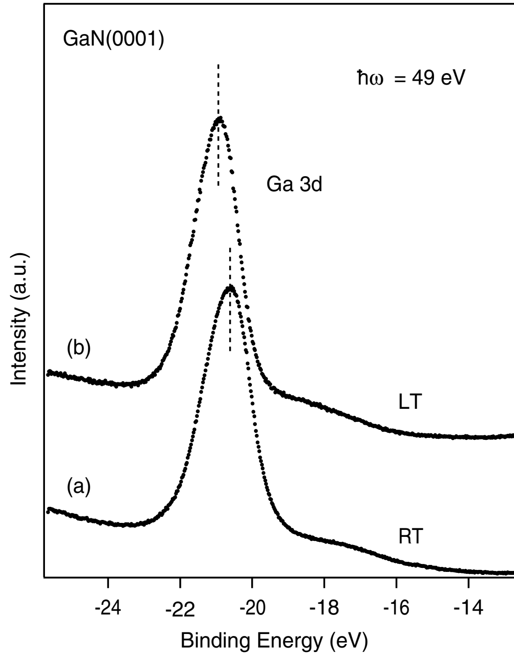

Figure 6.3: *Photoelectron spectra from clean GaN(0001) surface in the region of Ga 3d core level at different temperature. Spectrum (a) was at room temperature and spectrum (b) was at liquid nitrogen temperature.*

to the surface photovoltage effect that is more pronounced at low temperature.[Alonso et al., 1990]

This effect is visualized in Fig. 6.4. Under equilibrium condition, the Fermi level of the semiconductor lines up with that of the reference E_F, i.e. of the electron energy analyzer. When foreign atoms adsorb on the surface, such as the deposited metal, or surface defect or surface electronic states exist, the surface Fermi level will be "pinned" at an energy position other than the bulk position and causes band bending (V_{bb}),[Mönch, 1993] as shown in the left panel of Fig. 6.4. If the surface region is illuminated with photons of energy greater than that of the fundamental band gap, electron–hole pairs are generated (right panel), and because of the potential difference induced by the band bending, electrons are driven into the bulk, while the holes accumulate at the surface, compensating the space charge. This causes a rigid shift of all semiconductor levels. This situation can be described by a quasi–Fermi level, shown by the dashed curve.[Alonso et al., 1990] This effect is a self–limiting process since the surface band bending is needed to separate or trap the mobile carriers. This local charge compensation reduces the band bending and causes the low temperature spectra shift to higher binding energy.

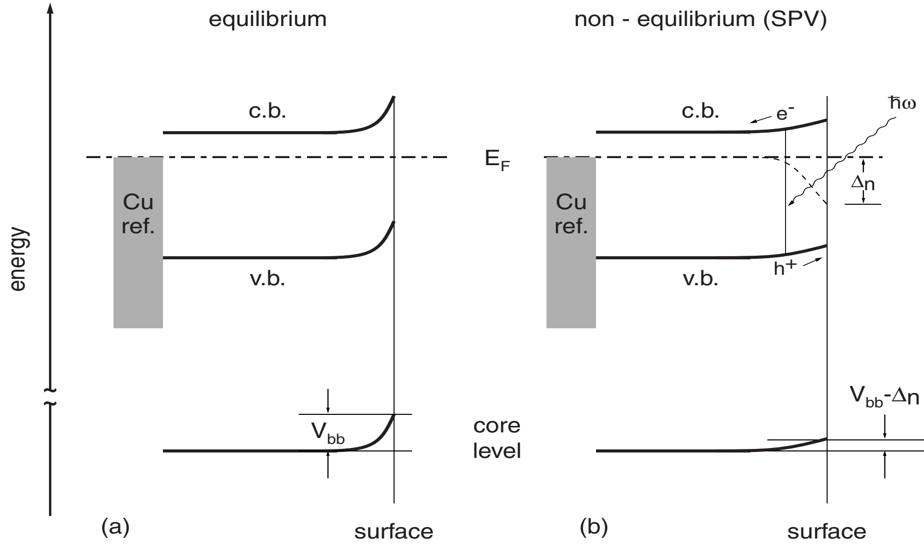

Figure 6.4: *(a)Schematic drawing of the equilibrium level alignment, upward band bending (V_{bb}) is caused by the deposition of foreign atoms, surface electronic states, or surface defects. (b)The influence of the surface photovoltage on the energies of the peaks. The dashed curve represent the quasi–Fermi level.*

As the deposited Ag layer becomes thicker, the Ga $3d$ peak and the metallic Fermi edge shift toward lower binding energy (see Fig. 6.5). This is due to the increase of overlayer thickness, which will lead to a reduction of photon flux and a concomitant decrease in SPV.[Alonso et al., 1990] Eventually the SPV will break down caused by the short–circuit at the edges of the film,[Horn, 2000] the Fermi edge then will coincide with the reference E_F and can be unambiguously determined.

The situation for Ag on AlN(0001) surface is shown in the spectra for the Al $2p$ core level and valence band plus Fermi edge area in Fig. 6.6. The lower spectra are from the clean AlN(0001) surface, features in the valence band region are clearly visible, which is similar to the valence spectra showed in Fig. 4.20. The upper spectra are from a thick (65Å) Ag overlayer, where the strong Ag d–band and metallic Fermi edge are observable. Some residual Al $2p$ signal still exists, this may be because the Ag deposit on AlN(0001) surface is not really epitaxially grown, photoelectrons from the substrate can still escape from the holes in the silver layer. The upper and lower spectra

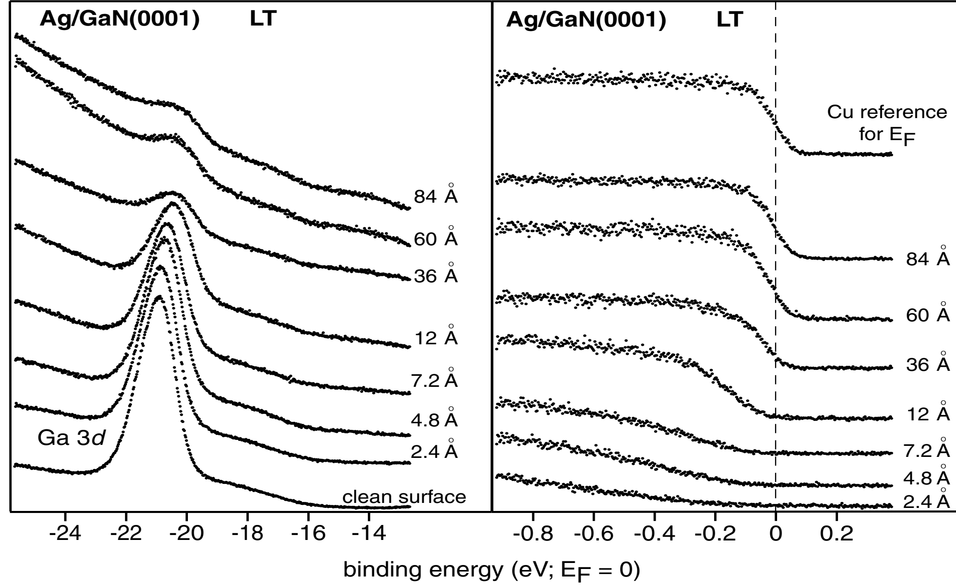

Figure 6.5: *Ga 3d core level recorded at low temperature with different An thickness (left), the spectra of the valence–band edge of GaN(0001) (right), showing the magnitude of the SPV–induced shift as a function of Ag overlayer thickness.*

were aligned as described in previous chapters in order to compensate for the band bending and SPV effect. The final energy difference between the clean surface VBM and the Ag Fermi edge is 3.33 eV, which is equivalent to a Schottky barrier height of 2.87 eV, with 6.2 eV of wurtzite–AlN fundamental band gap.[Strite and Morkoç, 1992]

The Schottky barrier heights after correction for SPV are

$$\Phi_{SB}^{GaN}(Ag) = 1.01 \text{ eV} \qquad \Phi_{SB}^{AlN}(Ag) = 2.87 \text{ eV} \tag{6.2}$$

for silver on GaN(0001) and AlN(0001) surfaces, respectively.

The barrier height of Ag on GaN(0001) is slightly higher than the value from reference[Kampen and Mönch, 1997], which was 0.82 eV, determined by current–voltage (I–V) measurement. The difference of about 0.19 eV is most likely caused by the use of different methods (i.e., I–V, C–V) to determine barrier heights,[Wolfframm et al., 2000] and different surface preparation techniques (e.g., surface etching, cleaving) prior to metal growth. It is also possible that differences in film properties due to the choice of substrate (sapphire for Kampen et al.[Kampen and Mönch, 1997] and 6H–SiC for our

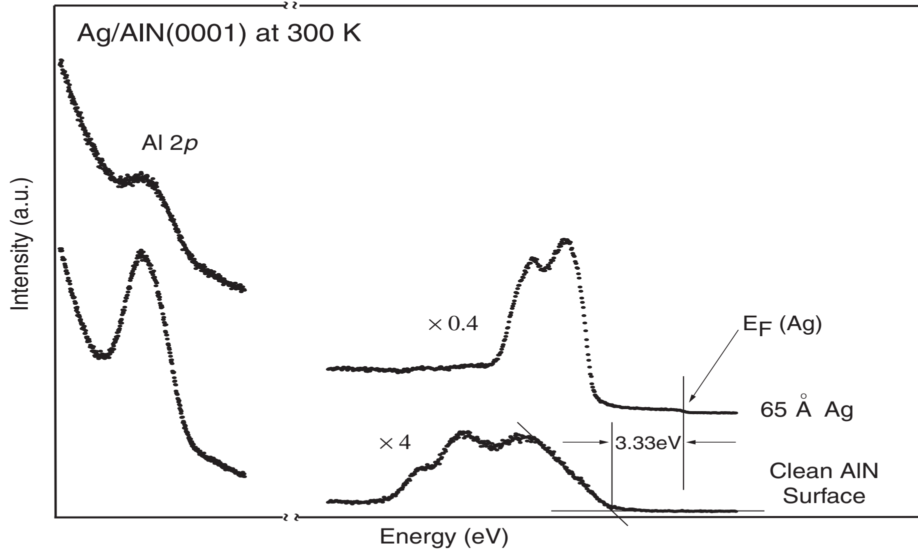

Figure 6.6: *Spectra of Al 2p core level, valence band, and Ag* d*–band from clean AlN surface and 65 Å of Ag overlayer. After the energy correction for SPV, energy difference between VBM from clean AlN and metallic Fermi edge is 3.33 eV. The corresponding Schottky barrier height is 2.87 eV.*

sample) are important, or that different surface polarities (i.e., the Ga versus N face) were studied.[Bermudez, 1999] The influence of lateral barrier height inhomogeneity can also not be ruled out.[Mönch, 1999]

A widely accepted model for the barrier heights was introduced by Heine [Heine, 1965] in 1965. He assumed that the barrier heights are determined by the continuum of the metal–induced gap states (MIGS). These intrinsic interface states derive from the virtual gap states (ViGS) of the complex semiconductor band structure. They represent the wave–function tails of the metal electrons into the semiconductor in the energy range between the VBM and the Fermi level where the metal conduction band overlaps the semiconductor band gap.[Mönch, 1996]

At the branch point (called the CNL in chapter 5), the character of the MIGS changes from predominantly donor– to predominantly acceptor–like, so that the net charge density in the MIGS is negative, vanishes, and becomes positive when the Fermi level is above, coincides with, and drops to below the CNL, respectively. The energy position of the Fermi level at the interface, which is equivalent to barrier height, depends on the occupation of

the continuum of MIGS.[Mönch, 1996]

Interface charge neutrality demands that the charge densities on the semiconductor and metal side are of equal magnitude but have opposite sign. The charge transfer across the interface may be described by the difference of the metal and semiconductor electronegativities, this model then predicts the barrier heights to vary as[Mönch, 1990]:

$$\Phi^{\mathrm{n}}_{\mathrm{SB}} = \phi_{\mathrm{cnl}} + \mathrm{S_x}(\mathrm{X_m} - \mathrm{X_s}) \tag{6.3}$$

where $\Phi^{\mathrm{n}}_{\mathrm{SB}}$ is the Schottky barrier height for n–type semiconductor, ϕ_{cnl} is the energy of the MIGS branch point relative to conduction band minimum,[Mönch, 1996] and $\mathrm{X_m}$ and $\mathrm{X_s}$ are the metal and semiconductor electronegativities, respectively. $\mathrm{S_x}$ is the slope parameter, which describes the dependence of the barrier height on metal electronegativity (and thus the work function). It is related to the density of MIGS, the thickness of the dipole layer at the interface and an appropriate interface dielectric constant.[Mönch, 1999] A semi–empirical rule that was justified theoretically[Mönch, 1996] relates the slope parameters with the optical dielectric constant ε_∞ of the semiconductor as:

$$\frac{\mathrm{A_x}}{\mathrm{S_x}} - 1 = 0.1(\varepsilon_\infty - 1)^2 \tag{6.4}$$

The parameter $\mathrm{A_x}$ depends on the electronegativity scale used and one obtains $\mathrm{A_x} = 0.86$ for Miedema's solid–state electronegativities.[Mönch, 1996] In the literature, researchers normally deposit different metals on the semiconductor then deduced the slope parameter by differentiating eq. 6.3; $\mathrm{S_x} = \frac{d\Phi_{\mathrm{SB}}}{d\mathrm{X_m}}$. Since we deposited one metal on two semiconductors, we reverse the procedure, calculate the theoretical slope parameter and the Schottky barrier height, then compare with our experimental barrier height. The optical dielectric constant ε_∞ is 5.45 for GaN,[Kampen and Mönch, 1997] which gives the theoretical slope parameter $\mathrm{S_x} = 0.29$.

In dealing with interfaces between solids, Miedema's scale of electronegativities is preferred[Mönch, 1993], and the values can be found in the same reference. The average electronegativity of a compound is given by the geometric mean of the atomic values of the constituents.[Mönch, 1990] For a binary compound one thus obtains

$$\mathrm{X_{AB}} = \sqrt{\mathrm{X_A} \times \mathrm{X_B}} \tag{6.5}$$

From table A.4 of reference[Mönch, 1993], one can find $\mathrm{X_{Ag}} = 4.45$, $\mathrm{X_{Ga}} = 4.10$, $\mathrm{X_{Al}} = 4.20$, and $\mathrm{X_N} = 7.00$, according to eq. 6.5 we can obtain

$X_{GaN} = \sqrt{4.10 \times 7.00} = 5.36$, $X_{AlN} = 5.42$.

We then take a branch point energy of the continuum of interface–induced gap states from Mönch[Mönch, 1997] obtained from empirical tight binding calculations, this yield $\phi^*_{cnl} = 2.35$eV above the valence band maximum, which is equal to 1.1 eV relative to conduction band minimum. With all the electronegativities, slope parameter, and branch point energy, the calculated Ag on GaN(0001) Schottky barrier height from eq. 6.3, which is based on the MIGS theory with ideal abrupt interface, is 0.84 eV. This value is fairly close to the barrier height we measured; 1.01 eV.

Table 6.1: *The optical dielectric constant (ε_∞) of AlN, the calculated slope parameters (S_x) use eq. 6.4, and the Schottky barrier height (Φ^{AlN}_{SB})calculated with eq. 6.3.*

ε_∞	S_x	Φ^{AlN}_{Bn} (eV)
4.51[a)]	0.39	2.85
3.86[b)]	0.47	2.77
4.27[c)]	0.42	2.82
4.84[d)]	0.35	2.89

[a)] Pseudopotential calculation. [Chen et al., 1995]
[b)] Linear–muffin–tin–orbital calculation. [Christensen and Gorczyca, 1994]
[c)] Orthogonal linear–combination–of–atomic–orbital calculation. [Xu and Ching, 1993]
[d)] Reflectivity measurements from AlN thin films on sapphire. [Collins et al., 1967]

Returning to the calculation for barrier heights described above, the optical dielectric constant ε_∞ for AlN from the literature is shown in table 6.1, and also listed in the table are the calculated slope parameter (S_x) from these constants and the resulting theoretical Schottky barrier heights. The branch point energy for AlN is 3.23 eV[Mönch, 1997] relative to the CBM. From table 6.1 we can see that the calculated barrier heights are in good agreement with our measurement, therefore, the slope parameter of AlN is about 0.37, calculated from our experimental barrier height.

When $S_X = 1$, we have the Schottky–Mott case, and the metal work func-

tion or electronegativity is the only parameter to control the barrier height. On the other hand, when $S_X = 0$, the barrier height becomes independent of metal work function, the Fermi level is pinned at the charge neutrality level of the interface states. In this slope parameter spectrum, both of the slope parameters for GaN and AlN are in the 0.3, 0.4 range, i.e. in the area where the metal work function does not have much influence on the Schottky barrier height, and the Fermi level will not deviate much from the branch point energy. This means a high density of metal–induced gap states exist in the metal–nitride interfaces that semi–pinned the Fermi level at the CNL.

The slope parameters of some other Ga compound semiconductors are listed as follow, GaP: 0.13[Linz et al., 1993], and GaAs: 0.1[Mönch, 1990]. These values are much smaller than that of GaN and AlN, which suggests that for GaP and GaAs, the MIGS will be so high that the Schottky barrier heights are not strongly influenced by the metal electronegativity, i. e. away from the Schottky–Mott model. In the early stages of Schottky barrier height investigations, Kurtin et al. have studied wide extended semiconductors and suggested that semiconductors with a larger band gap or ionicity will tend to behave more Schottky–Mott–like.[Kurtin et al., 1969] Comparing our experimental slope parameters of GaN and AlN with GaP and GaAs, the result is supporting Kurtin's postulate. However, when we turn to ZnS, which is also a wide band gap semiconductor with a fundamental band gap of 3.68 eV,[Wolfframm et al., 2000] the slope parameter is 0.76[Wolfframm et al., 2000], much higher than that of AlN. This is contradictory to the previous conclusion. This suggests that the band gap or ionicity of the semiconductors is not enough to describe the Schottky barrier behaviour precisely, the real trend may deviate from Kurtin's postulate.

Our Ag/GaN result is similar to an *ab initio* local density calculation on N–terminated [001] ordered Ag/GaN interface.[Picozzi et al., 2000] In those studies Picozzi et al.[Picozzi et al., 2000] calculated the c–GaN/noble–metal and c–GaN/Al interfaces. In the calculations, apart from the presence of MIGS, states from the strong interactions between noble–metal d states and nitrogen p states also exist. The resulting states are mainly localized in the interface region with a resonant behaviour inside the metal region and a negligible charge density in the GaN region. Such states are completely absent in GaN/Al–type structures due to the lack of d states in this system. This d–p state interaction is important for the interface formation but only localized in the metal side, the MIGS then still dominate the barrier behaviour. From their calculated barrier heights for Au and Ag overlayers, the slope parameter is 0.3, close to our experimental result.

However, for the GaN/Al interface, the barrier height is much higher than the noble–metal interfaces and deviates from the MIGS model. This is because the Al is a reactive metal on the GaN surface, a Ga–Al exchange reaction will occur at the immediate interface, driven by the AlN formation.[Picozzi et al., 2000, 1998a,b] This is probably the main reason for the deviation of GaN/Al interface from the MIGS model.

In conclusion, our photoemission studies from silver deposition on GaN(0001) and AlN(0001) surfaces are in good agreement with the ViGS model. A high density of metal induced gap states in nitride semiconductors apparently lead to a medium dependence of Schottky barrier heights on metal work function, but this relationship may only apply of the nonreactive noble–metals.

Chapter 7

Summary

This thesis describes investigations of the electronic properties of group III–nitride semiconductors. The electronic properties studied include the valence band structures along some symmetric directions in the bulk and surface Brillouin zone, GaN/SiC heterojunction band offset, and the silver–GaN, silver–AlN Schottky barrier heights. The electronic band structure is the central part of these studies, since it is the essential property that governs all the electronic behaviours of the solids. All of the studies were performed by means of angle–resolved photoemission spectroscopy with synchrotron radiation and low energy electron diffraction.

All of the nitride semiconductors exist in the metastable cubic phase, although it is difficult to grow, and most of the time a degree of mixture of hexagonal and cubic phases exist. Lima et al. was the first group to report the successful growth of cubic InN thin films on the InAs(001) surface by MBE method, and the results were confirmed by XRD and Raman spectra. The studies of the cubic InN electronic band structure were performed on these c–InN/InAs(001) thin films.

The growth of cubic InN on InAs(001) surface is similar to that of cubic GaN on GaAs(001) surface; both are large lattice misfit systems. The interface strain is released by the so–called "coincidence lattice",[Trampert and Ploog, 2000] and this provides an explanation for the epitaxial growth of such a large lattice mismatch system, at which epitaxy of covalently bonded material is usually no longer achieved, particularly so for the case of metastable phase.

After transportation through the air, one needs to find a method to clean the surface and restore the surface crystalline order. This was achieved by

annealing the InN thin films under ammonia atmosphere after mild ion bombardment. The ion sputtering removed the surface contaminations but also broke the nitrogen–indium bond and formed metallic indium clusters on the surface, these clusters were then converted to indium nitride again by annealing under ammonia pressure.

The normal emission ARPES was then measured on this restored cubic InN(001) surface, probing the valence bands with momentum along the $\Gamma - \Delta - X$ line in bulk Brillouin zone. The experimental band structure was compared with a pseudopotential band structure calculation which includes the In $4d$ and N $2s$ shallow core levels as part of the valence electrons. The comparison shows good agreement between theoretical and experimental band structure. However, for the In $4d$/N $2s$ levels, the calculation predicts that they should show some band–like dispersion due to their semi–valence property, which I did not resolve. From the core level spectra, it is not possible to locate the In $4d$ and N $2s$ lines precise enough to determine their dispersion behaviour. One will need an optimized stoichiometric surface to fulfill this purpose, which means a better sample preparation or surface cleaning process will be needed for further investigations on the shallow core level property.

Growth of high quality GaN thin films is difficult to achieve, in part because of the lack of a suitable substrate material. Yet some researchers have reported that depending on the Ga to N ratio during the growing period, the GaN(0001) surface reconstructed. Moreover, some evidences showed that the surface electronic properties are also largely depending on the surface preparation methods.

Thus I have tried to grow GaN thin films on the 6H–SiC(0001) surface by means of the MBE method, but have supplied ammonia or nitrogen plasma as different reactive nitrogen atom sources, and studied the difference between these two thin films. The growing processes are identical, the only difference is the gas sources. 6H–SiC is known to have a smaller lattice misfit than sapphire for GaN growth, and can produce better thin film quality. Also SiC is a semiconductor, which is more suitable for photoemission studies. The SiC wafer was cleaned by annealing the surface under Ga vapour prior to the thin film growth, the Ga vapour will react with surface oxygen and remove it in the form of Ga_2O.

Again, the normal emission ARPES was performed on GaN surfaces to investigate the valence band structures of these two different thin films. For

a hexagonal crystal with a (0001) surface, this will detect the band along the $\Gamma - \Delta - A$ line. It turns out that the bulk electronic band structures are identical to each other, and consistent with the local–density approximation band structure calculations, these calculations also include the Ga $3d$ level as part of the valence electrons. However, the surfaces are rather different. The GaN thin films grown by ammonia assisted MBE method have a distinct surface state in the valence band spectra, and the valence features are more pronounced, and a sharper LEED pattern exists. This indicates that with ammonia gas, one can grow better GaN thin films than nitrogen plasma. Part of the reason is that the hydrogen atoms released from the ammonia molecules are reactive and they can etch the surface roughness away to form a better SiC surface during the nitridation period. The surface band was studied with off–normal ARPES along the $\overline{\Gamma} - \overline{M}$ direction of the (1×1) surface Brillouin zone, which shows this state does not disperse much in this direction. It may originate from the surface dangling–bond state, as suggested by Chao et al.,[Chao et al., 1999] but one will need to compare with the calculations to ensure the result.

AlN also grown on 6H–SiC(0001) surface and in the hexagonal phase. Since the Al–N bond is the strongest amongst the nitride semiconductor family, the surface was cleaned simply by annealing the sample under UHV condition to $750 - 800°C$. This process cleaned the AlN surface, judged by the LEED and the valence band spectra. The valence band spectrum shows three clear features in the valence region and they disperse along with the changing of the incident photon energies, which is the proof of the band to band transitions.

The experimental valence band structure in the $\Gamma - A$ zone as well as the critical point energies were compared with theoretical band structure calculations . Amongst these calculations, the LDA method fits the experimental observation better. The comparison also shows that the band width calculated by the GW method is wider than the experimental result and the LDA calculation. This commonly observed for GW calculations.

The formation of the junctions of semiconductors with foreign materials is not only practically important, but also an interesting issue from a theoretical point of view. How the bands of a semiconductor align with other materials, either another semiconductor or a metal, has been under intensive study for decades.

Photoemission spectroscopy is a unique technique to study the interface

properties. Since it is a surface– and chemical–state–sensitive method, it can probe down to the monolayer scale to study the details of the interface formation. It is thus interesting to study the formation and electronic properties of GaN/SiC heterointerface and Ag/AlN, Ag/GaN Schottky barrier heights by photoemission spectroscopy.

From the Si 2*p* core level line shape analysis, only silicon–nitrogen bonds exist in the GaN–SiC interface region, no evidence of the existence of free silicon atoms or the formation of Si–Ga bonds was found. This is an indication of the successful SiC surface nitridation before the GaN thin film was deposited on the SiC surface. This surface nitridation process is aiming to increase the 6H–SiC(0001) surface energy and causes the 2D growth of GaN on SiC.

The resulting GaN/SiC heterojunction band alignment determined by photoemission spectroscopy is of the staggered type (type II) alignment. This type of alignment has potential applications for the devices that need to separate the electrons and holes in the interface region, such as solar cells or photon detectors. The valence band offset of this heterointerface is 1.10 eV for plasma grown GaN and 1.02 eV for ammonia grown GaN on SiC. These values are rather close to the theoretical value predicted by the charge neutrality level (CNL) alignment model.

The determination of the Schottky barrier heights of metal–semiconductor system by photoemission spectroscopy is similar to that of heterojunction valence band offset. However, for metals deposited on semiconductors, especially for wide band gap semiconductors or low temperature depositions, photoemission experiments may cause the surface photovoltage effect, which will interfere with the real Fermi level movement and induce mistake in extracting the Schottky barrier height from the photoemission spectra. One then has to take into account of the surface photovoltage effect before the Schottky barrier height determination.

After eliminating the effect of surface photovoltage effect, the Schottky barrier heights for silver on GaN(0001) surface and on AlN(0001) surface are 1.01 eV and 2.87 eV, respectively. These two values are in good agreement with the virtual gap states (ViGS) model.

From the Schottky barrier height and the optical dielectric constant, one can use eq. 6.4 to obtain the slope parameter, which is a parameter that can indicate whether the Schottky barrier height of a particular semiconductor

will largely depend on metal work function or not. For GaN and AlN, the slope parameters are in 0.3, 0.4 range. In this range, their Fermi levels will not deviate much from the CNL, the metal work function does not have much influence on their Schottky barrier heights. For the group III–nitrides, the barrier is mainly governed by their CNL, which means their Fermi levels are semi–pinned around CNL and the barrier heights are not much metal–dependent. However, this result is only available for the nonreactive metals. For reactive metals, such as Al on GaN, for example, due to the Ga–Al exchange reaction, the Schottky barrier height may deviate from the prediction of ViGS model.

Bibliography

M. Alonso, R. Cimino, and K. Horn. Surface photovoltage effects in photoemission from metal–GaP(110) interfaces: Importance for band bending evaluation. *Phys. Rev. Lett.*, 64:1947, 1990.

H. Amano, N. Sawaki, I. Akasaki, and Y. Toyoda. Metalorganic vapor phase epitaxial growth of a high quality GaN film using an AlN buffer layer. *J. Appl. Phys.*, 48:353, 1986.

O. Ambacher. Growth and applications of group III–nitrides. *J. Phys. D: Appl. Phys.*, 31:2653, 1998.

O. Ambacher, M. S. Brandt, R. Dimitrov, T. Metzger, M. Stutzmann, R. A. Fischer, A. Miehr, A. Bergmaier, and G. Dollinger. Thermal stability and desorption of group iii nitrides prepared by metal organic chemical vapor deposition. *J. Vac. Sci. Technol. B*, 14:3532, 1996.

N. W. Ashcroft and N. D. Mermin. *Solid State Physics.* Saunders College Publishing, Fort Worth, 1976.

J. Bardeen. Surface states and rectification at a metal semi–conductor contact. *Phys. Rev.*, 71:717, 1947.

J. J. Bellina Jr., J. Ferrante, and M. V. Zeller. Surface modification strategies for (100)3C–SiC. *J. Vac. Sci. Technol. A*, 4:1692, 1986.

M. C. Benjamin, M. D. Bremser, Jr. T. W. Weeks, S. W. King, R. F. Davis, and R. J. Nemanich. UV photoemission study of heteroepitaxial AlGaN films grown on 6H–SiC. *Appl. Surf. Sci.*, 104/105:455, 1996.

M. C. Benjamin, C. Wang, R. F. Davis, and R. J. Nemanich. Observation of a negative electron affinity for heteroepitaxial AlN on α(6H)–SiC(0001). *Appl. Phys. Lett.*, 64:3288, 1994.

C. N. Berglund and W. E. Spicer. Photoemission studies of copper and silver: Theory. *Phys. Rev.*, 136:A1030, 1964.

V. M. Bermudez. Study of the growth of thin Mg films on wurtzite GaN surfaces. *Surf. Sci.*, 417:30, 1998.

V. M. Bermudez. Simple interpretation of metal/wurtzite–GaN barrier heights. *J. Appl. Phys.*, 86:1170, 1999.

V. M. Bermudez, T. M. Jung, K. Doverspike, and A. E. Wickenden. The growth and properties of Al and AlN films on GaN(0001) $-$ (1×1). *J. Appl. Phys.*, 79:110, 1996.

V. M. Bermudez, R. Kaplan, M. A. Khan, and J. N. Kuznia. Growth of thin Ni films on GaN(0001)–(1×1). *Phys. Rev.*, B48:2436, 1993.

V. M. Bermudez, D. D. Koleske, and A. E. Wickenden. The dependence of the structure and electronic properties of wurtzite GaN surfaces on the method of preparation. *Appl. Sruf. Sci.*, 126:69, 1998.

V. M. Bermudez, C.-I. Wu, and A. Kahn. AlN films on GaN: sources of error in the photoemission measurement of electronic affinity. *J. Appl. Phys.*, 89:1991, 2001.

P. R. Bevington. *Data Reduction and Error Analysis for the Physical Sciences*. McGraw–Hill, 1969.

A. J. Van Bommel, J. E. Crombeen, and A. Van Tooren. LEED and Auger electron observations of the SiC(0001) surface. *Surf. Sci.*, 48:463, 1975.

F. Boscherini, R. Lantier, A. Rizzi, F. DÁcapito, and S. Mobilio. Evidence for relaxed and high–quality growth of GaN on SiC(0001). *Appl. Phys. Lett.*, 74:3308, 1999.

O. Brandt, H. Yang, A. Trampert, M. Wassermeier, and K. H. Ploog. Optimized growth conditions for the epitaxial nucleation of β–GaN on GaAs(001) by molecular beam epitaxy. *Appl. Phys. Lett.*, 71:473, 1997.

Y.-C. Chao, C. B. Stagarescu, J. E. Downes, P. Ryan, K. E. Smith, D. Hanser, M. D. Bremser, and R. F. Davis. Observation of highly dispersive surface states on GaN(0001)1×1. *Phys. Rev. B*, 59:R15586, 1999.

J. Chen, Z. H. Levine, and J. W. Wilkins. Calculated second–harmonic susceptibilities of BN, AlN, and GaN. *Appl. Phys. Lett.*, 66:1129, 1995.

T. -C. Chiang, J. A. Knapp, M. Aono, and D. E. Eastman. Angle–resolved photoemission, valence–band dispersion $E(\vec{k})$, and electron and hole lifetims for GaAs. *Phys. Rev. B*, 21:3513, 1980.

T.-C. Chiang and D. E. Eastman. Experimantal energy–band dispersions, critical points, and spin–orbit splittings for GaSb using angle–resolved photoemission. *Phys. Rev. B*, 22:2940, 1980.

W. Y. Ching and B. N. Harmon. Electronic structure of AlN. *Phys. Rev. B*, 34:5305, 1986.

A. Y. Cho and J. R. Arthur. Molecular beam epitaxy. *Prog. Solid–State Chem.*, 10:157, 1975.

N. E. Christensen and I. Gorczyca. Optical and structural properties of III–V nitrides under pressure. *Phys. Rev. B*, 50:4397, 1994.

F. Ciocci, G. Dattoli, A. Torre, and A. Renieri. *Insertion devices for synchrotron radiation and free electron laser.* World Scientific, Singapore, 2000.

Morrel H. Cohen, H. Fritzsche, and S. R. Ovshinsky. Simple band model for amorphous semiconducting alloys. *Phys. Rev. Lett.*, 22:1065, 1969.

A. T. Collins, E. C. lightowlers, and P. J. Dean. Lattice vibration spectra of aliminum nitride. *Phys. Rev.*, 158:833, 1967.

M. G. Craford. Leds challenge the incandescents. *IEEE Circuit Devices*, 8: 24, 1992.

C. J. Davisson and L. H. Germer. Diffraction of electrons by a crystal of nickel. *Phys. Rev.*, 30:705, 1927.

M. Dayan. The β–SiC(100) surface studied by low energy electron diffraction, Auger electron spectroscopy, and electron energy loss spectra. *J. Vac. Sci. Technol. A*, 4:38, 1986.

J. A. Dean. *Lang's handbook of chemistry, 14th edition.* McGraw-Hill, Inc., New York, 1992.

S. S. Dhesi, C. B. Stagarescu, K. E. Smith, D. Doppalapudi, R. Singh, and T. D. Moustakas. Surface and bulk electronic structure of thin–film wurtzite GaN. *Phys. Rev.*, B56:10 271, 1997.

S. A. Ding, S. R. Barman, K. Horn, and V. L. Alperovich. *Electronic Structure of Wurtzite GaN(0001).* Proceedings of the 23rd International Conference on the Physics of Semiconductors. World Scientific, Singapore, 1996.

S. A. Ding, S. R. Barman, K. Horn, H. Yang, B. Yang, O. Brandt, and K. H. Ploog. Valence band discontinuity at a cubic GaN/GaAs heterojunction measured by synchrotron–radiation photoemission spectroscopy. *Appl. Phys. Lett.*, 70:2407, 1997.

L. Duda, L. S. O. Johansson, B. Reihl, H. W. Yeom, S. Hara, and S. Yoshida. Electronic structure of the 3C–SiC(001)2×1 surface studied with angle–resolved photoelectron spectroscopy. *Surf. Sci.*, 439:199, 1999.

C. R. Eddy Jr., T. D. Moustakas, and J. Scanlon. Growth of gallium nitride thin films by electron cyclotron resonance microwave plasma–assisted molecular beam epitaxy. *J. Appl. Phys.*, 73:448, 1993.

J. H. Edgar. *Properties of Group III nitrides.* INSPECT, London, 1994.

A. Einstein. Über einen die erzeugung und verwandlung des lichtes betreffenden heuristischer gesichtspunkt (On the heuristic point of view concerning the production and conversion of light). *Annalen der Physik*, 17: 132, 1905.

G. Ertl and J. Küppers. *Low energy electrons and surface chemistry.* VCH, Weinheim, 1985.

E. V. Etzkorn and D. R. Clarke. Cracking of GaN films. *J. Appl. Phys.*, 89: 1025, 2001.

H. Y. Fan. Theory of photoelectric emission from metals. *Phys. Rev.*, 64:43, 1945.

V. Fiorentini, M. Methfessel, and M. Scheffler. Electronic and structural properties of GaN by the full-potential linear muffin-tin orbitals method: the role of the d electron. *Phys. Rev. B*, 47:13 353, 1993.

A. Franciosi and C. G. Van de Walle. Heterojunction band offset engineering. *Surf. Sci. Rep.*, 25:1, 1996.

M. Fuchs, C. Stampfl, and M. Scheffler. *to be published.*

Q. Guo, O. Kato, and A. Yoshida. Thermal stability of indium nitride single crystal films. *J. Appl. Phys.*, 73:7969, 1993.

Q. X. Guo, M. Nishio, H. Ogawa, A. Wakahara, and A. Yoshida. Electronic structure of indium nitride studied by photoelectron spectroscopy. *Phys. Rev. B*, 58:15 304, 1998.

P. Hacke, G. Feuillet, H. Okumura, and S. Yoshida. Monitoring surface stoichiometry with the (2×2) reconstruction during growth of hexagonal–phase GaN by molecular beam epitaxy. *Appl. Phys. Lett.*, 69:2507, 1996.

W. A. Harrison. Elementary theory of heterojunctions. *J. Vac. Sci. Technol.*, 14:1016, 1977.

W. A. Harrison. *Electronic structure and the properties of solids–The physics of the chemical bond*. Dover Publications, New York, 1989.

W. A. Harrison. *Elementary Electronic Structure*. World Scientific, Singapore, 1999.

W. A. Harrison and J. Tersoff. Tight–binding theory of heterojunction band lineups and interface dipole. *J. Vac. Sci. Technol.*, B4:1068, 1986.

V. Heine. Theory of surface states. *Phys. Rev.*, 138:A1689, 1965.

H. K. Henisch. *Semiconductor Contacts*. Oxford, New York, 1984.

H. Hertz. Über einen einfluss des ultravioletten lichtes auf die elektrishe entladung (On the influence of ultraviolet light on the electric discharge). *Annalen der Physik und Chemie*, 31:983, 1887.

F. J. Himpsel. Experimental determination of bulk energy band dispersions. *Appl. Opt.*, 19:3964, 1980.

F. J. Himpsel, B. S. Meyerson, F. R. Mcfeely, J. F. Morar, A. Taleb-Ibrahimi, and J. A. Yarmoff. *Core Level Spectroscopy at Silicon Surfaces and Interfaces*, volume CVIII of *Photoemission and Absorption Spectroscopy of Solids and Interfaces with Synchrotron Radiation*. North Holland, Amsterdam, 1990.

K. Horn. Semiconductor interface studies using core and valence level photoemission. *Appl. Phys.*, A51:289, 1990.

K. Horn. Photoemission studies of barrier heights in metal–semiconductor interfaces and heterojunctions. *Appl. Surf. Sci.*, 166:1, 2000.

K. Horn, B. Reihl, A. Zartner, D. A. Eastman, K. Hermann, and J. Noffke. Electronic energy bands of lead: Angle–resolve photoemission and band–structure calculations. *Phys. Rev. B*, 30:1711, 1984.

K. Horn and M. Scheffler. *Electronic Structure, Handbook of Surface Science*, volume 2. Elsevier, Amsterdam, 2000.

K. Hricovini, G. Le Lay, M. Abraham, and J. E. Bonnet. Phase transition on the Ge(111) and Si(111) surface from core–level studies. *Phys. Rev.*, B41:1258, 1990.

S. Hüfner. *Photoelectron Spectroscopy: Principles and Applications.* Springer–Verlag, Berlin, 1995.

R. W. Hunt, L. Vanzetti, T. Castro, K. M. Chen, L. Sorba, P. I. Cohen, W. Gladfelter, J. M. Van Hove, J. N. Kuznia, M. Asif Khan, and A. Franciosi. Electronic structure, surface composition and long–range order in GaN. *Physica B*, 185:415, 1993.

H. Ishikawa, S. Kobayashi, Y. Koide, S. Yamasaki, S. Nagai, J. Umezaki, M. Koike, and M. Murakami. Effects of surface treatments and metal work functions on electrical properties at p–GaN/metal interfaces. *J. Appl. Phys.*, 81:1315, 1997.

S. C. Jain, M. Willander, J. Narayan, and R. Van Overstraeten. Iii–nitrides: growth, characterization, and properties. *J. Appl. Phys.*, 87:965, 2000.

N. M. Johnson, A. V. Nurmikko, and S. P. DenBaars. Blue diode lasers. *Physics Today*, 53:31, Oct. 2000.

M. Kamp, M. Mayer, A. Pelzmann, and K. J. Ebeling. On surface cracking of ammonia for mbe growth of GaN. *Mater. Res. Soc. Symp. Proc.*, 449: 162, 1997.

T. U. Kampen and W. Mönch. Barrier heights of GaN Schottky contacts. *Appl. Surf. Sci.*, 117/118:388, 1997.

R. Kaplan. Surface studies of epitaxial β–SiC on Si(100). *J. Appl. Phys.*, 56: 1636, 1984.

R. Kaplan. Surface structure and composition of β and 6H–SiC. *Surf. Sci.*, 215:111, 1989.

R. Kaplan and T. M. Parrill. Reduction of SiC surface oxides by a Ga molecular beam: LEED and electron spectroscopy study. *Surf. Sci.*, 165: L45, 1986.

H. Amanoand M. Kito, K. Hiramatsu, and I. Akasaki. P–type conduction in Mg–doped GaN treated with low–energy electron beam irradiation (LEEBI). *Jpn. J. Appl. Phys.*, 28:L2112, 1989.

C. Kittel. *Introduction to Solid State Physics.* Jonn Wiley & Sons, Inc., Singapore, 1986.

G. R. Kline and K. M. Lakin. 1.0–GHz thin–film bulk acoustic wave resonators on GaAs. *Appl. Phys. Lett.*, 43:750, 1983.

E. Koch, D. E. Eastman, and Y. Farge. *Synchrotron radiation– a powerful tool in science*, volume 1a of *Handbook on synchrotron radiation.* North-Holland, Amsterdam, 1983.

H. Kroemer. *Proceedings of the NATO Advanced Study Insititute on Molecular Beam Epitaxy and Heterostructures, Erice.* Studies in Surface Science and Catalysis. Nijhoff, The Hague, 1983.

S. Kurtin, T. C. McGill, and C. A. Mead. Fundamental transition in the electronic nature of solids. *Phys. Rev. Lett.*, 22:1433, 1969.

H.-J. Kwon, Y.-H. Lee, O. Miki, H. Yamano, and A. Yoshida. Raman spectra of indium nitride thin films grown by microwave–excited metalorganic vapor phase epitaxy on (0001) sapphire substrates. *Appl. Phys. Lett.*, 69: 937, 1996.

H. Lahrèche, M. Leroux, M. Laügt, M. Vaille, B. Beaumont, and P. Gibart. Buffer free direct growth of GaN on 6H-SiC by metalorganic vapor phase epitaxy. *J. Appl. Phys.*, 87:577, 2000.

S. D. Lester, F. A. Ponce, M. G. Craford, and D. A. Steigerwald. High dislocation densities in high efficiency GaN–based light–emitting diodes. *Appl. Phys. Lett.*, 66:1249, 1995.

L. Ley, M. Cardona, and R. A. Pollak. *Photoemission in Semiconductors.* Photoemission in Solids II: Case Studies. Springer–Verlag, Berlin, 1979.

A. P. Lima, A. Tabata, J. R. Leite, S. Kaiser, D. Schikora, B. Schöttker, T. Frey, D. J. As, and K. Lischka. Growth of cubic InN on InAs(001) by plasma–assisted molecular beam epitaxy. *J. Crystal Growth*, 201/202:396, 1999.

R. Linz, H. J. Clemens, and W. Mönch. Cesium on GaP(110) surfaces: aconfirmationof the metal–induced gap state–plus–defects model. *J. Vac. Sci. Technol. B*, 11:1591, 1993.

L. Liu and J. H. Edgar. Substrates for gallium nitride epitaxy. *Materials Science and Engineering*, R 37:61, 2002.

Z. H. Lu, E. Sacher, A. Selmani, and A. Yelon. Supersaturated substitutional Ga^+ ion implanted in silicon studied by x–ray photoemission spectroscopy. *Appl. Phys. Lett.*, 54:2665, 1989.

H. Lüth. *Surfaces and Interfaces of Solid Materials*. Springer–Verlag, Berlin, 1997.

G. D. Mahan. Theory of photoemission in simple metals. *Phys. Rev. B*, 2: 4334, 1970.

G. Martin, S. Strite, A. Botchkarev, A. Agarwal, A. Rockett, H. Morkoç, W. R.L. Lambrecht, and B. Segall. Valence–band discontinuity between GaN and AlN measured by x–ray photoemission spectroscopy. *J. Appl. Phys.*, 65:610, 1994.

H. P. Maruska and J. J. Tietjen. The preparation and properties of vapour–deposited single–crystal–line GaN. *Appl. Phys. Lett.*, 15:327, 1969.

M. Mayer, A. Pelzmann, M. Kamp, J. K. Ebeling, H. Teisseyre, G. Nowak, M. Leszczyńsk, I. Grzegory, S. Porowski, and G. Karczewski. High quality homoepitaxy GaN grown by molecular beam epitaxy with nh_3 on surface cracking. *Jpn. J. Appl. Phys.*, 36:L1634, 1997.

T. Miller and T.-C. Chiang. Initial oxidation of GaAs(110): A core–level photoemission study. *Phys. Rev.*, B29:7034, 1984.

B. J. Min, C. T. Chan, and K. M. Ho. First–principles total–energy calculation of gallium nitride. *Phys. Rev. B*, 45:1159, 1992.

S. N. Mohammad, A. A. Salvador, and H. Morkoç. Emerging gallium nitride based devices. *Proceedings of the IEEE*, 83:1306, 1995.

R. J. Molnar, R. Singh, and T. D. Moustakas. Operation of a compact electron cyclotron resonance source for the growth of gallium nitride by molecular beam epitaxy (ECR–MBE). *J. Electron. Mater.*, 24:275, 1995.

W. Mönch. On the physics of metal–semiconductor interfaces. *Rep. Prog. Phys.*, 53:221, 1990.

W. Mönch. *Semiconductor Surfaces and Interfaces*. Springer–Verlag, Berlin, Heidelberg, 1993.

W. Mönch. Chemical trends of barrier heights in metal–semiconductor contacts: on the theory of the slope parameter. *Appl. Surf. Sci.*, 92:367, 1996.

W. Mönch. Elementary calculation of the branch–point energy in the continuum of interface–induced gap states. *Appl. Surf. Sci.*, 117/118:380, 1997.

W. Mönch. Barrier heights of real Schottky contacts explained by metal–induced gap states and lateral inhomogeneities. *J. Vac. Sci. Technol. B*, 17:1867, 1999.

B. Monemar and G. Pozina. Group III–nitride based hetero and quantum structures. *Porg. Quant. Elec.*, 24:239, 2000.

H. Morkoç. Potential applications of III–V nitride semiconductors. *Mat. Sci. Eng. B*, 43:137, 1997.

T. Mukai, D. Morita, and S. Nakamura. High–power UV InGaN/AlGaN double–heterostructure LEDs. *J. Crystal Growth*, 189/190:778, 1998.

S. Nakamura. Characteristics of InGaN–based multi–quantum–well–structure laser diodes. *Mater. Res. Soc. Proc.*, 449:1135, 1996.

S. Nakamura. The roles of strucutral imperfactions in InGaN–based blue light–emitting diodes and laser diodes. *Science*, 281:956, 1998.

S. Nakamura, T. Mukai, M. Senoh, and N. Iwasa. Thermal annealing effects on p–type Mg doped GaN films. *Jpn. J. Appl. Phys.*, 31:L139, 1992.

S. Nakamura, M. Senoh, S. Nagahame, N. Iwasa, T. Yamada, T. Matsushita, H. Kiyoku, and Y. Sugimoto. InGaN–based multi–quantum–well–structure laser diodes. *Jpn. J. Appl. Phys.*, 35:L74, 1996.

J. Neugebauer and C. G. Van de Walle. Atomic geometry and electronic structure of native defects in GaN. *Phys. Rev. B*, 50:8067, 1994.

J. E. Van Nostrand, J. Solomon, A. Saxler, Q.-H. Xie, D. C. Reynolds, and D. C. Look. Dissociation of Al_2O_3(0001) substrates and the roles of silicon and oxygen in n-type GaN thin solid films grown by gas-source molecular beam epitaxy. *J. Appl. Phys.*, 87:8766, 2000.

J. W. Ortony and C. T. Foxonz. Group III nitride semiconductors for short wavelength light–emitting devices. *Rep. Prog. Phys.*, 61:1, 1998.

M. J. Paisley and R. F. Davis. Molecular beam epitaxy of nitride thin films. *J. Crystal Growth*, 127:136, 1993.

Linus Pauling. *General Chemistry.* Dover Publications, New York, 1970.

S. Picozzi, A. Continenza, S. Massidda, and A. J. Freeman. Structural and electronic properties of ideal nitride/Al interfaces. *Phys. Rev. B*, 57:4849, 1998a.

S. Picozzi, A. Continenza, S. Massidda, A. J. Freeman, and N. Newman. Influence of the exchange reaction on the electronic structure of GaN/Al junctions. *Phys. Rev. B*, 58:7906, 1998b.

S. Picozzi, A. Continenza, G. Satta, S. Massidda, and A. J. Freeman. Mteal–induced gap states and Schottky barrier heights st nonreactive GaN/noble–metal interfaces. *Phys. Rev. B*, 61:16 736, 2000.

K. H. Ploog, O. Brandt, R. Muralidharan, A. Thamm, and P. Waltereit. Growth of high–quality (Al, Ga)N and (Ga, In)N heterostructures on SiC(0001) by both plasma–assisted and reactive molecular beam epitaxy. *J. Vac. Sci. Technol. B*, 18:2290, 2000.

K. H. Ploog, O. Brandt, H. Yang, B. Yang, and A. Trampert. Nucleation and growth of GaN layers on GaAs, Si and SiC substrates. *J. Vac. Sci. Technol.*, B16:2229, 1998.

F. A. Ponce and D. P. Bour. Nitride–based semiconductors for blue and green light–emitting devices. *Nature*, 386:351, 1997.

L. M. Porter and R. F. Davis. A critical review of ohmic and rectifying contacts for silicon carbide. *Materials Science and Engineering*, B34:83, 1995.

L. E. Ramos, L. K. Teles, J. L. P. Castineira, A. L. Rosa, and J. R. Leite. Structural, electronic, and effective-mass properties of silicon and zinc-blende group-III nitride semiconductor compounds. *Phys. Rev. B*, 63: 165210, 2001.

S. Y. Ren and J. D. Dow. Role of interfacial–charge in the growth of GaN on α–SiC. *J. Electron. Mater.*, 26:341, 1997.

G. M. Rignanese and A. Pasquarello. Nitrogen bonding configurations at nitrided Si(001) surfaces and Si(001)–SiO_2 interfaces: A first–principles study of core–level shifts. *Phys. Rev.*, B63:075307, 2001.

A. Rizzi, R. Lantier, F. Monti, H. Lüth, F. D. Sala, A. D. Carlo, and P. Lugli. AlN and GaN epitaxial heterojunctions on 6H-SiC(0001): valence band offsets and polarization fields. *J. Vac. Sci. Technol. B*, 17:1674, 1999.

A. Rubio, J. L. Corkill, M. L. Cohen, E. L. Shirley, and S. G. Louie. Quasiparticle band structure of AlN and GaN. *Phys. Rev. B*, 48:11810, 1993.

M. Seelmann-Eggebert, J. L. Weyher, H. Obloh, H. Zimmermann, A. Rar, and S. Porowski. Polarity of (00·1) GaN epilayers grown on a (00·1) sapphire. *Appl. Phys. Lett.*, 71:2635, 1997.

D. A. Shirley. High–resolution x–ray photoemission spectrum of the valence band of gold. *Phys. Rev.*, B5:4709, 1972.

G. A. Slack and T. F. McNelly. Growth of high purity AlN crystal. *J. Crystal Growth*, 34:263, 1976.

J. C. Slater. Electronic energy bands in metals. *Phys. Rev.*, 45:794, 1934.

A. R. Smith, R. M. Feenstra, D. W. Greve, J. Neugebauer, and J. E. Northrup. Reconstructions of the GaN($000\bar{1}$) surface. *Phys. Rev. Lett.*, 79:3934, 1997.

A. R. Smith, R. M. Feenstra, D. W. Greve, M. S. Shin, M. Skowronski, J. Neugebauer, and J. E. Northrup. Reconsrtuctions of GaN(0001) and GaN($000\bar{1}$) surfaces: Ga–rich metallic structures. *J. Vac. Sci. Technol. B*, 16:2242, 1998.

A. R. Smith, R. M. Feenstra, D. W. Greve, M.-S. Shin, M. Skowronski, J. Neugebauer, and J. E. Northrup. GaN(0001) surface structures studied using scanning tunneling microscopy and first–princilpes total energy calculations. *Surf. Sci.*, 423:70, 1999.

A. R. Smith, R. M. Feenstra, D. W. Greve, M.-S. Shin, M. Skowronski, J. Neugebauer, and J. E. Northrup. Determination of wurtzite GaN lattice polarity based on surface reconstruction. *Appl. Phys. Lett.*, 72:1998, 2114.

L. Sorba, V. Hinkel, H. V. Middelmann, and K. Horn. Bulk and surface electronic bands of InP(110) determined by angle–resolved photoemission. *Phys. Rev. B*, 36:8075, 1987.

C. Stampfl and C. G. Van de Walle. Density-functional calculations for III-V nitrides using the local-density approximation and the generalized gradient approximation. *Phys. Rev. B*, 59:5521, 1999.

U. Starke, Ch. Bram, P.-R. Steiner, W. Hartner, L. Hammer, K. Heinz, and K. Müller. The (0001)–surface of 6H–SiC: morphology, composition and structure. *Appl. Surf. Sci.*, 89:175, 1995.

J. Stöhr, P. S. Wehner, R. S. Williams, G. Apai, and D. A. shirley. Bulk versus surface effects in normal photoemission from Cu(110) in the range $32 \leq h\nu \leq 160\ eV$. *Phys. Rev. B*, 17:587, 1978.

S. Strite, D. Chandrasekhar, D. J. Smith, J. Sariel, H. Chen, N. Teraguchi, and H. Morkoç. Structural properties of InN films grown on GaAs substrates: observation of the zincblende polytype. *J. Crystal Growth*, 127: 204, 1993.

S. Strite and H. Morkoç. GaN, AlN, and InN: A review. *J. Vac. Sci. Technol. B*, 10:1237, 1992.

S. M. Sze. *Physics of Semiconductor Devices.* Wiley, New York, 1981.

A. Tabata, R. Enderlein, J. R. Leite, S. W. da Silva, J. C. Galzerani, D. Schikora, M. Kloidt, and K. Lischka. Comparative Raman studied of cubic and hexagonal GaN epitaxial layers. *J. Appl. Phys.*, 79:4137, 1996.

A. Tabata, A. P. Lima, L. K. Teles, L. M. R. Scolfaro, J. R. Leite, V. Lemos, B. Schöttker, T. Frey, D. Schikora, and K. Lischka. Structural properties and raman modes of zinc blende InN epitaxial layers. *Appl. Phys. Lett.*, 74:362, 1999.

J. Terry, M. R. Linford, C. Wigren, R. Cao, and P. Pianetta. Alkyl–terminated Si(111) surfaces: A high–resolution, core level photoelectron spectroscopy study. *J. Appl. Phys.*, 85:213, 1999.

J. Tersoff. Theory of semiconductor heterojunctions : The role of quantum dipoles. *Phys. Rev.*, B30:4874, 1984.

W. Theis. *Photoemission an Aluminium in der Nähe des Schmelzpunktes.* PhD thesis, Freie Universität Berlin, 1989.

P. Thiry, D. Chandesris, J. Lecante, C. Guillot, R. Pinchaux, and Y. Pétroff. E vs $\vec{k}$ and inverse lifetime of Cu(110). *Phys. Rev. Lett.*, 43:82, 1979.

J. T. Torvik, M. W. Leksono, J. I. Pankove, C. Heinlein, J. K. Grepstad, and C. Magee. Interfacial effect during GaN growth on 6H–SiC. *J. Elec. Mat.*, 28:234, 1999.

A. Trampert, O. Brandt, H. Yang, and K. H. Ploog. Direct observation of the initial nucleation and epitaxial growth of metastable cubic GaN on (001) GaAs. *Appl. Phys. Lett.*, 70:583, 1997.

A. Trampert and K. H. Ploog. Heteroepitaxy of large–misfit systems:role of coincidence lattice. *Cryst. Res. Technol.*, 35:793, 2000.

T. Valla, P. D. Johnson, S. S. Dhesi, K. E. Smith, D. Doppalapudi, T. D. Moustakas, and E. L. Shirley. Unoccupied band structure of wurtzite GaN(0001). *Phys. Rev. B*, 59:5003, 1999.

V. van Elsbergen, T. U. Kampen, and W. Mönch. Surface analysis of 6H–SiC. *Surf. Sci.*, 365:443, 1996.

M. van Schilfgaarde, A. Sher, and A.-B. Chen. Theory of AlN, GaN, InN and their alloys. *J. Crystal Growth*, 178:8, 1997.

M. von Schilfgaarde and N. Newman. Electronic structure of ideal metal/GaAs contacts. *Phys. Rev. Lett.*, 65:2728, 1990.

B. A. Weinstein, P. Perlin, N. E. Christensen, I. Gorczyca, V. Iota, T. Suski, P. Wisniewski, M. Osinski, and P. G. Eliseev. Cubic InN inclusiobs: proposed explanation for the small pressure–shift anomaly of the luminescence in InGaN–Based quantum wells. *Solid State Commum.*, 106:567, 1998.

C. Weisbuch and B. Vinter. *Quantum semiconductor structures, fundamentals and applications*. Academic Press, Boston, 1991.

G. K. Wertheim, D. M. Riffe, J. E. Rowe, and P. H. Citrin. Crystal–field splitting and charge flow in the buckled–dimer reconstruction of Si(100)2$\times$1. *Phys. Rev. Lett*, 67:120, 1991.

H. Winick. *Synchrotron radition sources–A Primer*. World Scientific, Singapore, 1994.

D. Wolfframm, D. A. Evans, G. Neuhold, and K. Horn. Gold and silver Schottky barriers on ZnS(110). *J. Appl. Phys.*, 87:3905, 2000.

D. P. Woodruff and T. A. Delchar. *Modern techniques of surface science–second edition*. Cambridge University, Cambridge, 1994.

A. F. Wright. Elastic properties of zinc–blende and wurtzite AlN, GaN, and InN. *J. Appl. Phys*, 82:2833, 1997.

C. I. Wu and A. Kahn. Electronic states at aluminum nitride (0001)–1$\times$1 surfaces. *Appl. Phys. Lett.*, 74:546, 1999.

Y. N. Xu and W. Y. Ching. Electronic, optical, and structural properties of some wurtzite crystals. *Phys. Rev. B*, 48:4335, 1993.

Q. Xue, Q. K. Xue, Y. Hasegawa, I. S. T. Tsong, and T. Sakurai. Two–step preparation of 6H–SiC(0001) surface for epitaxy growth of GaN thin film. *Appl. Phys. Lett.*, 74:2468, 1999.

H. Yang, O. Brandt, M. Wassermeier, J. Behrend, H. P. Schönherr, and K. H. Ploog. Evaluation of the surface stoichiometry during molecular beam epitaxy of cubic GaN on (001) GaAs. *Appl. Phys. Lett.*, 68:244, 1996.

H. W. Yeom, T. Abukawa, Y. Takakuwa, Y. Mori, T. Shimatani, A. Kakizaki, and S. Kono. Electronic structures of the Si(001)2×3–In surface. *Phys. Rev. B*, 55:15669, 1997.

W. M. Yim and R. J. Paff. Thermal expansion of AlN, sapphire and silicon. *J. Appl. Phys.*, 45:1456, 1974.

S. Yoshida, S. Misawa, and S. Gonda. Improvements on the electrical and luminescent properties of reactive molecular beam epitaxially grown GaN films by using AlN–coated sapphire substrates. *J. Appl. Phys.*, 42:427, 1983.

X. Yu, A. Raisanen, G. Haugstad, N. Troullier, G. Biasiol, and A. Fransiosi. Nonmagnetic–semimagnetic semiconductor heterostructures: Ge–$Cd_{1-x}Mn_xTe$(110). *Phys. Rev.*, B48:4545, 1993.

Acknowledgements

I want to thank my supervisor, Prof. Karsten Horn, for his support throughout the whole course of my study, without his support, I will not have the opportunity to come to Germany that largely expand my vision. I also want to thank him for his kindness and willing to give me his invaluable advice and share his life experience.

I am grateful to Prof. Mario Dähne for all his help in the Technischen Universität Berlin and his co-assessing this thesis.

Dr. Ruth Klauser is always willing to give me her suggestions and all her supports, which are not only limited in the academic area, thank you very much.

Henrik Haak is the most skillful technical designer I ever met, without his design and built of the MBE cell, sample exchange system and chambers, none of the experiments could be accomplished.

Dr. Sudipt R. Barman, we had my very first beamtime in BESSY I; TGM4, his teaching about the UHV system and ARPES, gave me a solid foundation for my later work.

Dr. Lucía Aballe, we had countless beamtime together in BESSY, she was always energetic and brought the sunshine to the experimental station.

Dr. D.-H. Wie, Dr. I.-H. Hong, Mr. S.-C. Wang, Mr. G.-C. Yin and Mr. M.-L. Huang, thank you all for your fully supports and always keeping the working atmosphere friendly at NSRRC.

In the end, I want to thank my family, for their love and their encouragement, especially to my beloved wife Shu-feng, she's always accompanying me, listen to me and give me her hands whenever I need them.

Thank you all, without the help and all the supports from you, this thesis is surely not possible to be finished.

Zusammenfassung

Die Halbleiter der Gruppe III-Nitride und ihre Verbindungen haben in den letzten Jahren wegen ihrer weitreichenden Anwendungen als Feldemitter für kurze Wellenlängen und optoelektronische Bauteile groβes Interesse hervorgerufen. Diese Entwicklung ist vor allem der Realisierung des p-dotierten Nitridhalbleiters und des erfolgreichen Wachstums dünner Schichten hoher Qualität zu verdanken.

Ungeachtet der steigenden Zahl an kommerziellen Produkten auf Nitridbasis, sind viele fundamentelle Fragen zu den Eigenschaften dieser Halbleiter noch ungeklärt. In der vorliegenden Doktorarbeit wurden die elektronischen Eigenschaften der Gruppe III-Nitridhalbleiter mittels winkelaufgelöster Photoelektronenspektrokopie (ARPES) mit Synchrotronstrahlung und der Beugung langsamer Elektronen (LEED) untersucht.

Das Reinigungsverfahren von kubischem InN wurde untersucht und eine geordnete kristalline Oberfläche erzielt. Dünne Schichten von hexagonalem GaN wurden mittels Molekularepitaxie unter Verwendung von Ammoniakgas oder Stickstoffplasma als Quelle für atomaren Stickstoff auf 6H-SiC(0001) gewachsen. Ergebnisse der Messungen mit LEED umd Photoelektronenspektroskopie zeigten, daβ die mit Ammoniakgas gewachsenen Schichten von besserer Qualität waren als solche bei denen molekularer Stickstoff verwendet wurde.

Die besetzten Valenzbänder von kubischem InN, wurtzischem GaN und AlN wurden mit ARPES gemessen und die dispersiven Strukturen im Valenzbandbereich wurden bei Annahme eines freien Elektronenendzustandes in Volumenbandstrukturen umgerechnet. Ein Oberflächenzustand wurde für die mit Ammoniak gewachsene GaN(0001)-(1×1) Oberfläche beobachtet und entlang der $\overline{\Gamma} - \overline{M}$ Brillouinzone ausgemessen.

Die GaN/SiC Grenzflächen wurden mit Photoelektronenspektroskopie untersucht. Die Linienbreiten der Rumpfniveaus zeigen, daβ in der Grenzfläche nur Stickstoff eine chemische Verbindung mit Silizium eingeht, verursacht durch die Nitridierung der SiC(0001) Oberfläche vor dem Wachstum der GaN Schicht. Dies ist nötig, um die Oberflächenenergie zu erhöhen und die Benetzungseigenschaften von Ga auf der SiC Oberfläche zu verbessern. Der GaN/SiC Heteroübergang ist vom Versetzungstyp (Typ II) und der gemessene Valenzbandoffset ist 1.02 eV für die mit Ammoniak gewachsene und 1.10 eV für die mit Stickstoffplasma gewachsene GaN Schicht.

Die Schottky-Barrieren von Ag auf GaN und AlN Oberflächen wurden mit Photoelektronenspektroskopie ermittelt. Der Oberflächen-Photovoltage-Effekt wurde beobachtet, nachdem der Halbleiter auf flüssige Stickstofftemperatur heruntergekühlt wurde. Dieser Effekt muβ bei der Bestimmung der Schottkybarriere mittels Photoelektronenspektroskopie berücksichtigt werden. Die Schottkybarriere is 1.01 eV für Ag/GaN und 2.87 eV für Ag/AlN. Das Ergebnis zeigt, daβ die Barrieren für nicht reaktive Metalle auf GaN und AlN Oberflächen nicht mit der Schottky-Mott Regel beschrieben werden können.